

APPLIED  
COMPUTATIONAL  
ELECTROMAGNETICS  
SOCIETY  
JOURNAL

November 1997  
Vol. 12 No. 3

ISSN 1054-4887

**DISTRIBUTION STATEMENT A**

Approved for public release  
Distribution Unlimited

19971114 065

**GENERAL PURPOSE AND SCOPE.** The Applied Computational Electromagnetics Society Journal hereinafter known as the **ACES Journal** is devoted to the exchange of information in computational electromagnetics, to the advancement of the state-of-the-art, and to the promotion of related technical activities. A primary objective of the information exchange is the elimination of the need to "re-invent the wheel" to solve a previously-solved computational problem in electrical engineering, physics, or related fields of study. The technical activities promoted by this publication include code validation, performance analysis, and input/output standardization; code or technique optimization and error minimization; innovations in solution technique or in data input/output; identification of new applications for electromagnetics modeling codes and techniques; integration of computational electromagnetics techniques with new computer architectures; and correlation of computational parameters with physical mechanisms.

**SUBMISSIONS CONTENT.** The **ACES Journal** welcomes original, previously unpublished papers, relating to **applied computational electromagnetics**.

Typical papers will represent the computational electromagnetics aspects of research in electrical engineering, physics, or related disciplines. However, papers which represent research in **applied computational electromagnetics** itself are equally acceptable.

For additional details, see "Information for Authors" on the back cover.

**SUBSCRIPTIONS.** All members of the Applied Computational Electromagnetics Society (**ACES**) who have paid their subscription fees are entitled to receive the **ACES Journal** with a minimum of three issues per calendar year. See page for ACES membership and Newsletter and Journal Subscription form.

**Visit us on line at:** [www.emclab.umn.edu/aces](http://www.emclab.umn.edu/aces)

**Back issues**, when available, are \$15.00 each. Subscriptions to **ACES**, orders for back issues of the **ACES Journal** and changes of addresses should be sent to:

Dr. Richard Adler  
ACES Executive Officer  
ECE Department, Code ECAB  
Naval Postgraduate School  
833 Dyer Road, Room 437  
Monterey, CA 93943-5121 USA

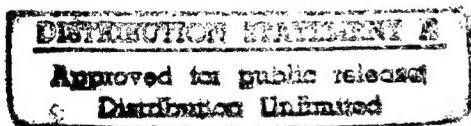
Allow four week's advance notice for change of address. Claims for missing issues will not be honored because of insufficient notice or address change or loss in mail unless the secretary is notified within 60 days for USA and Canadian subscribers or 90 days for subscribers in other countries, from the last day of the month of publication. For information regarding reprints of individual papers or other materials, see "Information for Authors".

**LIABILITY.** Neither ACES or the **ACES Journal** editors are responsible for any consequence of misinformation or claims, express or implied, in any published material in an **ACES Journal** issue. This also applies to advertising, for which only camera-ready copies are accepted. Authors are responsible for information contained in their papers. If any material submitted for publication includes material which has already been published elsewhere, it is the author's responsibility to obtain written permission to reproduce such material.

APPLIED  
COMPUTATIONAL  
ELECTROMAGNETICS  
SOCIETY  
Journal

November 1997  
Vol. 12 No. 3

ISSN 1054-4887



The ACES Journal is abstracted in INSPEC, in Engineering Index, and in DTIC.

The second, third, fourth, and fifth illustrations on the front cover have been obtained from Lawrence Livermore National laboratory.

The first illustration on the front cover has been obtained from FLUX2D software, CEDRAT S.S. France, MAGSOFT Corporation, New York.

DTIC QUALITY INSPECTED 2

# THE APPLIED COMPUTATIONAL ELECTROMAGNETICS SOCIETY

## JOURNAL EDITORS

### EDITOR-IN-CHIEF/ACES

**W. Perry Wheless, Jr.**  
University of Alabama, EE Dept.  
PO Box 870286  
Tuscaloosa, AL 35487-0286 USA

### ASSOC. EDITOR-IN-CHIEF/JOURNAL

**Adalbert Konrad**  
University of Toronto  
Toronto, ON, CANADA M5S 1A4

**Ruediger Anders**  
Applied EM Engineering  
Roswell, GA, USA

**Brian A. Austin**  
University of Liverpool  
Liverpool, UK

**Joao Bastos**  
University Fed De Santa Catarina  
Florianopolis, BRAZIL

**John Beggs**  
Mississippi State University  
Mississippi State, MS, USA

**Fulvio Bessi**  
Ingegneria dei Sistemi S.p.A.  
Pisa, ITALY

**Robert Bevensee**  
Box 812  
Alamo, CA, USA

**John R. Bowler**  
University of Surrey  
Surrey, UK

**John Brauer**  
Ansoft Corporation  
Milwaukee, WI, USA

**Robert T. Brown**  
Lockheed Aeronautical Sys. Co.  
Valencia, CA, USA

**Edgar Coffey**  
Advanced Electromagnetics  
Albuquerque, NM, USA

**Tony Fleming**  
Telecom Australia.  
Clayton, Victoria, AUSTRALIA

**Pat Foster**  
Microwave & Antenna Systems  
Gt. Malvern, Worc. UK

**Allen Glisson**  
University of Mississippi  
University, MS, USA

### EDITOR-IN-CHIEF/JOURNAL

**Duncan C. Baker**  
EE Dept. University of Pretoria  
0002 Pretoria, SOUTH AFRICA

### EDITOR-IN-CHIEF, EMERITUS

**Robert M. Bevensee**  
Box 812  
Alamo, CA, 94507-0516 USA

**Gregory R. Haack**  
DSTO  
Salisbury, SA, AUSTRALIA

**Christian Hafner**  
Swiss Federal Inst. of Technology  
Zurich, SWITZERLAND

**Kueichien C. Hill**  
Wright Laboratory  
Wright-Patterson AFB, OH, USA

**Todd H. Hubing**  
University of Missouri-Rolla  
Rolla, MO, USA

**Nathan Ida**  
The University of Akron  
Akron, OH, USA

**Ahmed Kishk**  
University of Mississippi  
University, MS, USA

**Peter Krylstedt**  
National Defence Research Est.  
Sundbyberg, SWEDEN

**Stanley Kubina**  
Concordia University  
Montreal, Quebec, CANADA

**Karl J. Langenberg**  
Universitat Kasse  
Kassel, GERMANY

**Ronald Marhefka**  
Ohio State University  
Columbus, OH, USA

**Gerald Meunier**  
NPG/ENSIEG  
St. Martin-d'Heres Cedex, FRANCE

**Edmund K. Miller**  
LASL  
Santa Fe, NM, USA

**Kenzo Miya**  
University of Tokyo  
Tokyo, JAPAN

### MANAGING EDITOR

**Richard W. Adler**  
833 Dyer Rd. Room 437  
Naval Postgraduate School Code EC/AB  
Monterey, CA 93943-5121 USA

### EDITOR-IN-CHIEF, EMERITUS

**David E. Stein**  
USAF Scientific Advisory Board  
Washington, DC 20330 USA

**Giorgio Molinari**  
University of Genova  
Genova, ITALY

**Frederic A. Molinet**  
Societe Mothesim  
Plessis-Robinson, FRANCE

**Gerrit Mur**  
Technische Universiteit Delft  
Delft, NETHERLANDS

**Giuseppe Pelosi**  
University of Florence  
Florence, ITALY

**Andrew F. Peterson**  
Georgia Institute of Technology  
Atlanta, GA, USA

**Kurt Richter**  
Technical University of Graz, IGTE  
Graz, AUSTRIA

**Harold A. Sabbagh**  
Sabbagh Associates  
Bloomington, IN, USA

**Chris Smith**  
Delfin Systems  
Santa Clara, CA, USA

**Norio Takahashi**  
Okayama University  
Tsushima, JAPAN

**Jean-Claude Verite**  
Electricite de France  
Clamart, Cedex, FRANCE

**Keith W. Whites**  
University of Kentucky  
Lexington, KY, USA

**John W. Williams**  
SAIC  
Germantown, MD, USA

# THE APPLIED COMPUTATIONAL ELECTROMAGNETICS SOCIETY

## JOURNAL

Vol. 12 No. 3

November 1997

### TABLE OF CONTENTS

"Domain Decomposition Strategies for Solving the Maxwell Equations on Distributed Parallel Architectures"	
T.A. Buter and D.C. Blake .....	4
"Moment Method Surface Patch and Wire Grid Accuracy in the Computation of Near Fields"	
R. Paknys and L.R. Raschkowan .....	16
"Using the FDTD Method to Model the Reflection Coefficient of a Vivaldi Tapered Slot Antenna Fed Through a Planar Balun"	
G. B. Gentili, R. Braccini, M. Leoncini and R. Evangelisti .....	26
"Finite-Difference Time-Domain Modeling of Light-Trapping in Solar Cells"	
T. Marshall and M. Piket-May .....	31
"Modelling Eddy Currents in Unbounded Structures Using the Impedance Method"	
D. James and D.V. Thiel .....	43
"Verification of Softwares for Electromagnetic Field Analysis Using Models Proposed by Investigation Committees in IEE of Japan"	
N. Takahashi .....	50
Announcements:	
Institutional Membership .....	63
Copyright Form .....	65
Application for ACES Membership and Newsletter and Journal Subscription .....	67
1998 14th Annual Review of Progress Pre-Registration Form .....	68
Advertising Rates .....	69
Copy Information - Deadline for Submission of Articles .....	69

© 1997, The Applied Computational Electromagnetics Society

# Domain Decomposition Strategies for Solving the Maxwell Equations on Distributed Parallel Architectures

Douglas C. Blake<sup>†</sup> and Thomas A. Buter<sup>§</sup>

Air Force Institute of Technology, Wright-Patterson Air Force Base, OH 45433

## Abstract

Domain decomposition strategies for solving hyperbolic systems of partial differential equations on distributed-memory parallel computing platforms are investigated. The logically-rectangular computational domain is divided either one, two, or three dimensionally into a series of computational blocks, and each block is assigned to a single processor. Theoretical predictions using standard parallel performance models indicate that higher-dimensional decompositions provide superior parallel program performance in terms of scalability. The theory is tested using a finite-volume time-domain (FVTD) Maxwell equations solver to compute the electromagnetic fields inside a rectangular waveguide using various grid sizes and processor numbers on three different parallel architectures—the Intel Paragon, the IBM SP2, and the Cray T3D. The specific performance of the FVTD algorithm on the three machines is investigated, the relation between processor connection topology and message passing performance of a typical grid-based hyperbolic equation solver are identified, and the results are used to augment the classical parallel performance model. Although clear performance trends emerge in terms of the dimensionality of the decomposition, results indicate that higher-dimensional decompositions do not always provide superior parallel performance.

## 1 Introduction

Numerical simulations of electromagnetic or fluid flow phenomena are most often constrained in their complexity by available computational processing capability. Although complex three-dimensional calculations were once the exclusive realm of the vector supercomputer, through recent dramatic advances in computer hardware technology—including the development of powerful Reduced Instruction Set Computing (RISC) microprocessors, high-density Dynamic Random Accesses Memory (DRAM), and very-high-speed switching networks—designers have been able to construct powerful machines comprised of hundreds to thousands of processors which are often capable of performance exceeding that of traditional vector supercomputers. Unfortunately, efficient utilization of these parallel machines requires much more effort on the part of the algorithm designer since compilers are not yet able to fully extract the

parallelism inherent in a computer code and properly map that parallelism to a distributed-memory environment.

One method of potentially achieving a high degree of concurrency in typical grid-based scientific computations such as those found in time-domain computational electromagnetics (CEM) or computational fluid dynamics (CFD) algorithms is to divide the computational domain into a series of subdomains or blocks and then assign the blocks in some manner to the available processors. This approach has been applied with an emphasis toward engineering practicality by several researchers in both the CFD and CEM communities<sup>1-6</sup>. Furthermore, the issue has been examined from a parallel efficiency standpoint by Wong, et al.<sup>7</sup>

Since the practice of domain decomposition has become increasingly prevalent, it is important to investigate methods for partitioning and assigning the computational domain to the available processors. Because the problem of determining an optimal mapping is known to be in problem space NP Complete<sup>8</sup>, no such attempt is made here. Instead three domain decomposition approaches—one, two, and three dimensional (as depicted in Figure 1)—are examined in terms of theoretical and measured parallel scalability. Furthermore, since modern parallel architectures differ widely in their processor capabilities, interprocessor connection topologies and communication bandwidths, it is reasonable to expect that a given domain mapping cannot yield identical parallel scalability across all platforms. For this reason, the domain decomposition analysis is performed on three separate parallel platforms which are discussed in the following section.

## 2 Target Architectures

The machines chosen for use in this study—the Intel Paragon, the IBM SP2 and the Cray T3D—arguably represent the most widely available currently produced distributed-memory computing platforms. Each of these machines is similar in that each utilizes RISC processors as its central processing units. However, the interprocessor connection topology of the machines differs substantially. The Paragon and T3D both employ very-high-performance static interconnection networks configured as a two-dimensional mesh and a three-dimensional torus, respectively. The SP2, on the other hand, utilizes an omega network of substantially lower bandwidth. In addition to the differences in connection topology, the T3D provides several programming options not available on the other machines due to its memory structure. Although the SP2 and Paragon are true distributed-memory platforms,

<sup>†</sup>PhD Candidate, Member ACES

<sup>§</sup>Assistant Professor of Aeronautical Engineering

This paper is declared a work of the U.S. Government and is not subject to copyright protection in the United States.



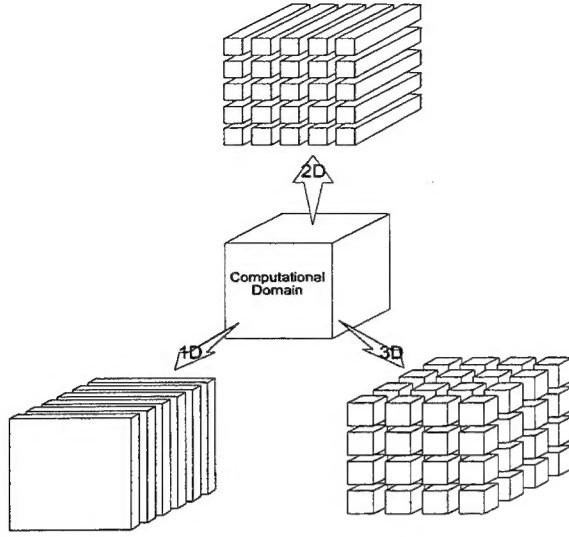


Figure 1: Domain Decomposition Techniques

the T3D is classified as a distributed-shared-memory machine since, although memory is physically distributed, a single global address space is available. This allows any processor to directly address memory contained on another processor. It is also possible to explicitly deliver data between processors through the use of a message-passing library such as that encapsulated in Parallel Virtual Machine (PVM)<sup>9</sup>. In this mode, the programming environment of the T3D is similar to that of the Paragon and SP2.

Although several message-passing libraries are available for each machine, the libraries used in this study were chosen based on vendor support, portability, and performance. At the inception of this study, PVM was actively supported by Cray Research for the T3D. Similarly, support and documentation for the Intel message passing library, NX<sup>10</sup>, was readily available. Finally, Message Passing Interface<sup>11</sup> (MPI) was selected for the SP2 due to its portability and performance. By abstracting the library-specific programming calls through the use of the macro feature in the C programming language, a single computer code was used to collect performance data on all three machines. A summary of the salient features of each of the machines appears in Table 1.

### 3 Problem Description

#### 3.1 Model Problem

The problem selected for examining the various domain decomposition approaches was the computation of the electromagnetic fields inside a rectangular waveguide as depicted in Figure 2. The computational domain for the problem was uniform and Cartesian, thereby facilitating a relatively straightforward partitioning of the domain. The physical dimensions  $a$ ,  $b$ , and  $L$  of the waveguide were scaled to  $\pi$ ,  $\pi$ , and 1 respectively, and the waveguide was

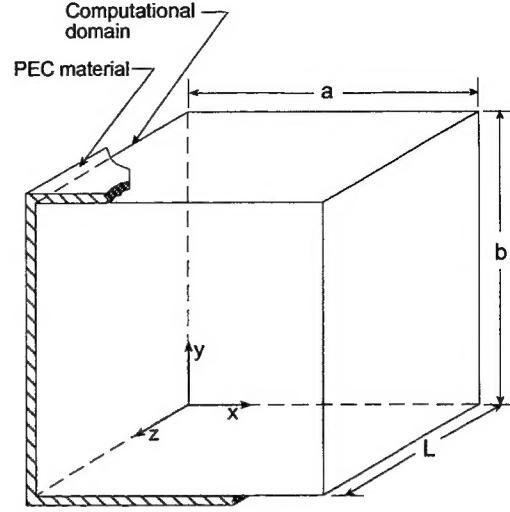


Figure 2: Rectangular Waveguide Geometry

excited in a TMZ11 mode. This problem has been extensively studied by Shang<sup>4,12</sup>, and the existence of an analytical solution<sup>13</sup> allows for a ready verification of parallel program correctness.

#### 3.2 Numerical Procedure

In order to compute the electromagnetic fields inside the rectangular waveguide, the differential vector forms of the two Maxwell curl equations are solved using a collocated, cell-centered, explicit FVTD scheme. For a general curvilinear  $(\xi, \eta, \zeta)$  coordinate system, the equations can be written as

$$\frac{\partial \tilde{Q}}{\partial t} + \frac{\partial \tilde{E}}{\partial \xi} + \frac{\partial \tilde{F}}{\partial \eta} + \frac{\partial \tilde{G}}{\partial \zeta} = \tilde{J} \quad (1)$$

where  $\tilde{Q}$  contains the six unknown scalar electromagnetic field components,  $\tilde{J}$  contains the scalar components of the surface current, and  $\tilde{E}$ ,  $\tilde{F}$ , and  $\tilde{G}$  are known as the *flux vectors*. Application of equation (1) to a general hexahedral finite volume cell yields

$$\frac{\partial(\tilde{Q}V)}{\partial t} + \sum_{k=1}^6 \tilde{R}_k \cdot \hat{n}_k A_k - \tilde{J}V = 0 \quad (2)$$

where  $\tilde{R} = \tilde{E}\hat{\xi} + \tilde{F}\hat{\eta} + \tilde{G}\hat{\zeta}$ ,  $\hat{n}_k$  and  $A_k$  are the unit surface normal and surface area of cell face  $k$ , respectively, and  $V$  is the cell volume.

In order to advance the solution in time, the FVTD scheme requires the evaluation of the flux vectors at the cell faces. To do so, the present study uses a flux-vector-splitting approach after Steger and Warming<sup>16</sup> which splits the flux at a cell face into positive and negative components according to the signs of the eigenvalues of the flux Jacobian matrix  $A$ ,

	Cray T3D (Eglin Air Force Base, FL)	IBM SP2 (Maui High Performance Computing Center)	Intel Paragon XP/S (Wright Patterson Air Force Base, OH)
central processing unit (CPU)	DEC Alpha 21064 @ 150 megahertz	IBM RS/6000 @ 66.7 megahertz	Intel i/860XP @ 50 megahertz
single processor megaflop rating (double precision)	150	266	75
number of compute processors	128	400	368
memory per CPU (megabytes)	64	64-1024	32-64
interprocessor connection topology	Three-dimensional torus (nodes configured 8 x 4 x 4)	Omega network	Two-dimensional mesh
communication bandwidth (megabytes/sec)	300	40	200
communication library used	Parallel Virtual Machine (PVM)	Message Passing Interface (MPI)	NX
maximum processors available to a single job (without special request)	128	128	128

Table 1: Target Machine Characteristics

where for the  $\eta$  direction

$$A = \frac{\partial \tilde{F}}{\partial Q} \quad (3)$$

and for the  $i+1/2$  face of cell  $i$  (see Figure 3),

$$\tilde{F}_{i+1/2} = \tilde{F}^+(\tilde{Q}_{i+1/2}^L) + \tilde{F}^-(\tilde{Q}_{i+1/2}^R) \quad (4)$$

Similar expressions hold for the fluxes at the five remaining cell faces. Note that the positive and negative fluxes in equation (4) are functions of the dependent variables at the left and right states (denoted by the superscripts  $L$  and  $R$  in the equation) of cell face  $i+1/2$ ; however, the dependent variables are not defined at the cell faces but rather at the cell centers. It thus becomes necessary to transfer information from cell centers to cell faces. This can be accomplished in one of two ways: the fluxes can be evaluated at cell centers and then extrapolated to cell faces, or the dependent variables can be extrapolated to the cell faces and the fluxes subsequently evaluated. The latter method is known as *Monotone Upstream-centered Schemes for Conservation Laws* (MUSCL) and is the methodology used in this work. Using the MUSCL approach after van Leer<sup>17</sup>, the extrapolation yields a scheme that is spatially third-order accurate.

With the flux evaluation complete, equation (2) is solved over each cell by applying a two-stage, second-order-accurate Runge Kutta procedure to the temporal derivative term. This yields a fully explicit numerical procedure that is ideally suited to a parallel implementa-

tion.

### 3.3 Parallel Implementation

The MUSCL scheme described in the previous section forms the crux of the data dependencies of the numerical scheme. Referring to Figure 3, in order to compute the total flux at cell face  $i+1/2$ ,  $\tilde{F}_{i+1/2}$ , the positive flux component requires dependent variable information from cells  $i-1$ ,  $i$ , and  $i+1$ . Similarly, the negative flux component requires information from cells  $i$ ,  $i+1$ , and  $i+2$ . These data dependencies are known as the *computational stencil* of the scheme and are depicted in the top portion of the figure. In a parallel environment, one or more of these cells may reside on different processors, and thus a means must exist to transfer necessary information between processors. The transfer of information is facilitated through the use of buffer storage locations. These locations serve to hold dependent-variable or other information that is computed on one processor but necessary for other computations on another. A sample of the buffer locations is shown as the shaded cells in the lower portion of Figure 3. Using this approach for the simple two-processor, one-dimensional example shown in the figure, the flux calculation for a cell which falls on a boundary created by the domain decomposition begins as processors 1 and 2 independently compute the positive and negative flux component, respectively, for cell face  $i+1/2$ . This calculation requires data stored in the buffer locations on each processor. Processor 1 passes the positive flux component to processor 2 which then computes the total



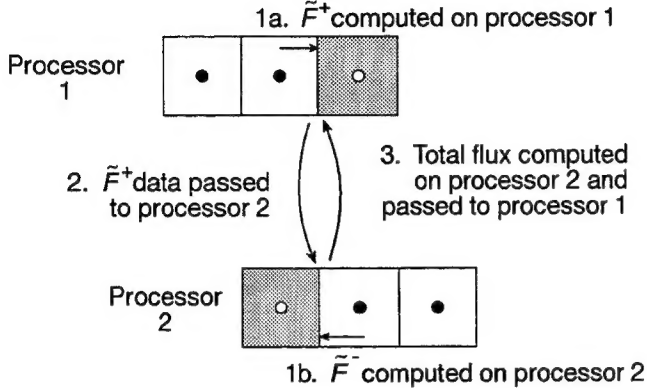
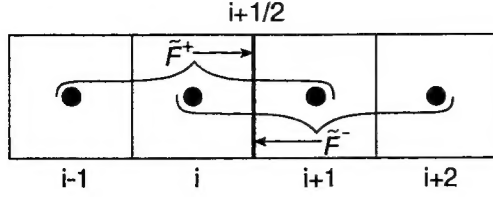


Figure 3: Flux Message Detail

flux for the cell face and returns this information to processor 1. Assuming the fluxes at the remaining cell faces have been calculated, the processors subsequently update cells  $i$  and  $i + 1$ , respectively, to the new time level. For a higher-dimensional problem, the message-passing scenario is repeated for each of the decomposition directions. No messages are required along a coordinate direction in which the computational domain is not decomposed. Once all cells have been updated to the new time level, dependent-variable information is exchanged so the buffer storage locations contain new time level data. Since the waveguide was considered filled with a homogeneous material (free space), the wave speed was uniform throughout the computational domain. This allows a single global time step determination at the beginning of program execution, and thus no global communications are required by the algorithm after the initial time step calculation.

It is possible to double the size of the buffers and thereby preclude the requirement for either processor to send any flux data to the other; however, this approach was examined and discarded since the storage penalty exacted was not offset by any significant performance gain.

#### 4 Parallel Analysis

##### 4.1 Theoretical Parallel Performance

Given the algorithm data dependencies described in the previous section, the theoretical parallel performance can be determined. Parallel run time,  $T_{par}$ , can be assumed to consist of contributions from calculations,  $T_{calc}$ , and from parallel overhead,  $T_{overhead}$ , i.e.

$$T_{par} = T_{calc} + T_{overhead} \quad (5)$$

The overhead consists of several factors including communication and any extra calculations necessary to implement the code on a parallel machine. For this analysis, the parallel overhead is assumed to be dominated by the communication time,  $T_{comm}$ . If the classical cut-through-routing communication cost model of Kumar, et al.<sup>19</sup> is used, then the communication time required for a single message to travel between processors  $a$  and  $b$ ,  $t_{comm}$ , is given by

$$t_{comm} = t_s + mt_w + lt_h \quad (6)$$

where  $t_s$  is the message start-up time,  $t_w$  is the per-word transfer time,  $t_h$  is the latency associated with a hop between two processors,  $m$  represents the number of words transferred, and  $l$  represents the number of hops the message must make in order to travel from processor  $a$  to processor  $b$ . In most modern parallel architectures, the per-hop time is extremely small and all processors can be considered computationally close. This allows the communication cost model to be simplified<sup>8</sup>, viz.

$$t_{comm} = t_s + mt_w \quad (7)$$

For this analysis, the computational domain is assumed to be three dimensional and to consist of  $n$  cells with  $n^{1/3} \equiv R$  cells distributed along each of the three coordinate directions. Furthermore, the domain is assumed to be evenly divided among the number of available processors,  $p$ . Thus, the number of grid cells residing on each processor,  $n_p$ , is given by

$$n_p = R^3 / p \quad (8)$$

With the exception of processors that contain the grid cells on the boundaries of the computational domain, each processor must send one message to each neighboring processor along each of the decomposition directions during the numerical flux computations. Furthermore, once the flux computations are complete, the updated dependent-variable information stored in the buffer arrays must be exchanged between neighboring processors. Since the time integration portion of the algorithm is a two-step procedure, this scenario is repeated twice in order to advance the solution in time. Consequently, the number of messages sent and received per time step is  $16i$ , and the length of each message,  $m$ , is

$$m = DR^2 p^{(1-i)/i} \quad (9)$$

where  $D$  represents the number of storage bytes required per grid cell for the dependent-variable data and  $i$  represents the dimensionality of the decomposition,  $0 \leq i \leq 3$ . Note that for  $i = 0$ , the computational domain is not decomposed, and thus  $i = 0 \Leftrightarrow p = 1$ . In all cases, the term  $p^{(1-i)/i}$  is restricted to integral values. Since the total communication

time is the product of the single message communication time and the total number of messages, then

$$T_{comm} = 16i(t_s + DR^2 p^{(1-i)/i} t_w) \quad (10)$$

which leads to the theoretical parallel run times for the various decompositions, namely

$$T_{par} = t_c(R^3/p) + 16i(t_s + DR^2 p^{(1-i)/i} t_w) \quad (11)$$

where  $t_c$  is the single-processor computation time per grid cell per time step.

With parallel run time determined, theoretical absolute speedup,  $S_a$ , and absolute efficiency,  $E_a$ —two of the most common metrics for parallel performance—can be determined using the standard definitions<sup>19</sup>

$$S_a = T_1/T_{par} \quad (12)$$

$$E_a = S_a/p \quad (13)$$

where  $T_1$  is the run time for the best known serial algorithm to solve the problem in question. It is often not practical to compare the chosen parallel algorithm against the best known serial algorithm, and consequently, relative speedup,  $S$ , and efficiency,  $E$ , are often used whereby the parallel algorithm run time is compared against the run time of the algorithm on a single processor. Substituting  $i = 0$ ,  $p = 1$  into equation (11) to determine  $T_1$ , the theoretical relative performance is thus given by

$$S = \frac{1}{\frac{1}{p} + \frac{16i}{R} [R^{-2}(t_s/t_c) + Dp^{(1-i)/i}(t_w/t_c)]} \quad (14)$$

$$E = \frac{1}{1 + \frac{16i}{R} [pR^{-2}(t_s/t_c) + Dp^{1/i}(t_w/t_c)]} \quad (15)$$

At this point, the applicability of the analysis to other implementations can be extended by treating the terms  $t_c$ ,  $t_s$ ,  $t_w$ , and  $16i$  (the number of message passes) as constants. An asymptotic analysis is then performed in which  $p$  and  $R$  are assumed large to yield<sup>19</sup>

$$E = \frac{1}{1 + \Theta(p^{1/i}/R)} \quad (16)$$

where  $\Theta$  indicates a tight upper bound.

It is important to note that the asymptotic analysis encapsulated in (16) is taken for  $p$  and  $R$  appropriately large when in fact, for a practical implementation, it may not be possible to let either variable grow suitably large due to memory or machine architecture restrictions. Consequently, a consideration of the constants appearing in (14) and (15) may be necessary when assessing true performance of the

algorithm on the machine of implementation.

Since parallel machines provide a means of solving relatively large problems over a fairly large number of processors, it is desirable to predict how an algorithm will perform as both the problem size and the number of processors is increased. *Isoefficiency* measures the scalability of an algorithm in such an instance and is determined by setting the computational work equal to the parallel overhead function<sup>19</sup>. In the present analysis, the isoefficiency is derived directly from equation (16) to yield

$$R = n^{1/3} = \Theta(p^{1/i}) \Rightarrow n = \Theta(p^{3/i}) \quad (17)$$

Thus, in order to maintain a constant parallel efficiency, a computational domain that is decomposed three dimensionally need only be increased in size by an amount linearly proportional to increasing processor number. One- and two-dimensional decompositions require larger increases in the size of the computational domain as increasing numbers of processors are applied to the problem if the efficiency is to be maintained at a constant value.

#### 4.2 Machine Performance Characterization

Determination of theoretical performance as embodied in equations (14) and (15) requires that the values of  $t_c$ ,  $t_s$ , and  $t_w$  be ascertained. In general,  $t_s$  and  $t_w$  are machine specific, while  $t_c$  depends both on the target architecture as well as the algorithm. In order to determine  $t_c$ , the FVTD algorithm was run for 100 time steps on a single processor on each of the three machines using a variety of grid sizes up to the maximum size containable in the machine's core memory. The times for these execution runs are contained in Figure 4. Although not presented here, a formal analysis of the FVTD algorithm run-time complexity reveals that the method is in time space  $\Theta(n)$  where  $n$  is the number of cells in the computational domain. This analysis is corroborated by the data exhibited in the figure which show the run times to be a linearly increasing function of  $n$ . Any slight deviations from linearity can be explained by noting that boundary condition cells require less computational work, and as the grid size decreases, the boundary condition points have an increased affect on the algorithm run time. Using a simple least-squares fit of the data,  $t_c$  was determined from the slope of each plot.

The message-passing performance of each of the three machines was determined by configuring eight processors as a logical ring and circulating messages of varying size 1000 times around the ring. Run time data for this experiment appears in Figure 5. By performing a linear curve fit of the data, the message start-up time and per-word transfer time can be computed directly from the y-intercept and line slope. Although the linear curve-fitting process generated excellent results (goodness of fit > 0.99 in all cases), the SP2 is characterized by marked and somewhat random variations in execution time. This variation is most likely due to message contention over the omega switching network. Table 2 con-

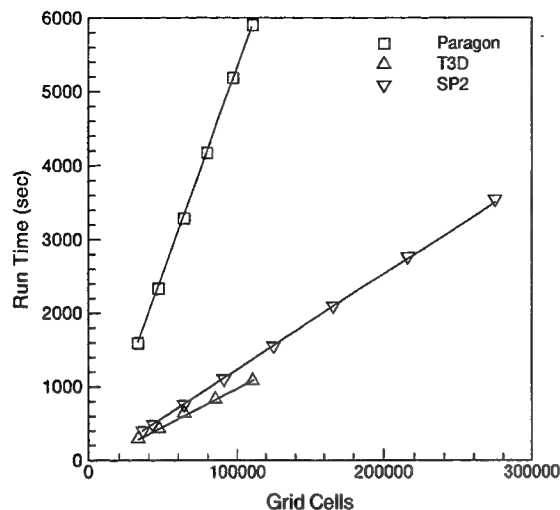


Figure 4: Single Node Algorithm Run Times

tains a summary of the findings of this portion of the study. The values agree in general with those of Foster<sup>8</sup>. Any discrepancies can be explained by differences in operating systems and message-passing libraries used.

## 5 Domain Decomposition Study

### 5.1 Test Procedure

As is evident in the theoretical derivations, parallel speedup and efficiency are dependent on a variety of parameters including the problem size and the number of processors on which the algorithm is executed. In order to test these parameters, the FVTD algorithm was run for 100 iterations on grid sizes ranging from  $R = 32$  to  $R = 128$  using up to 128 processors. One-hundred iterations was deemed an acceptable number so that run times would not be excessive yet any transient parallel-environment effects such as interprocess-message contentions would be suitably minimized. In every decomposition, the number of finite-volume cells residing on each processor was identical. This reduced, but did not completely eliminate, load imbalance since boundary condition cells require less computational effort than interior cells. The choice of domain decompositions and grid sizes was constrained primarily by the amount of memory available on each processor. This was especially true in the case of the Paragon which, with the exception of 16 "MP" nodes, possesses only 32 megabytes per processor. In addition to the memory constraint, additional restrictions were imposed by the processor-allocation scheme of the T3D. The current version of the operating system on this machine allows processors to be allocated only in powers of two. This required that the computational domain be partitioned in powers of two along each decomposition direction.

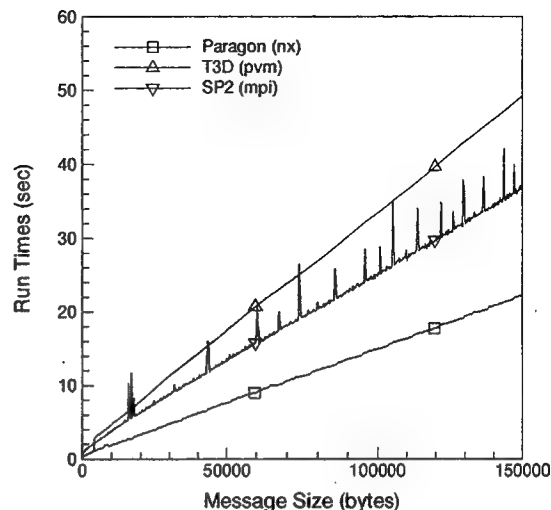


Figure 5: Ring Message Passing Times  
(1000 rings on 8 processors)

In addition to the dimensionality of the decomposition, the directional dependence of the decompositions was assessed by permuting the decompositions for each coordinate direction. The permutations correspond to a re-orientation of the planes or lines of grid points as depicted in Figure 1. Examination of the decomposition along each direction allows for an assessment of machine memory-accessing performance and uncovers potential bus contentions which are the inevitable result of mapping a higher-dimensional physical problem onto a lower-dimensional interconnection network. Table 3 contains a summary of the decompositions examined. Rather than list each grid size, processor count, and decomposition separately, they are combined into a single listing whenever possible with the understanding that all possible combinations on a given table row were examined.

The FVTD code used to conduct the study was written in C to take advantage of that language's dynamic memory allocation routines. Memory for each grid decomposition was allocated at run time. This facilitated the examination of

	$t_c$ ( $\mu$ sec)	$t_s$ ( $\mu$ sec)	$t_w$ ( $\mu$ sec)
T3D	102	25	.030
Paragon	546	36	.018
SP2	132	76	.040

Table 2: Machine and FVTD Algorithm Performance Parameters

Dimension of Partition	Grid Size (R)	Processors (P)	Decomposition*
1D	32, 64, 128	4, 8, 16, 32, 64, 128	$P \times 1 \times 1$ such that $P \leq R$
2D	32, 64, 96	4, 16, 64	$\sqrt{P} \times \sqrt{P} \times 1$
2D	32, 64, 96	8, 32, 128	$\sqrt{\frac{P}{2}} \times 2 \times \sqrt{\frac{P}{2}} \times 1$
3D	32, 64, 96	8, 64	$\sqrt[3]{P} \times \sqrt[3]{P} \times \sqrt[3]{P}$
3D	32, 64, 96	16, 128	$\sqrt[3]{\frac{P}{2}} \times 2 \times \sqrt[3]{\frac{P}{2}} \times 2 \left(\sqrt[3]{\frac{P}{2}}\right)$
3D	32, 64, 96	32	$2 \times 4 \times 4$

\*All permutations of the tabulated decompositions were performed. For example, in addition to the stated  $P \times 1 \times 1$  one-dimensional partitioning,  $1 \times P \times 1$  and  $1 \times 1 \times P$  partitions were also examined. The decomposition nomenclature refers to the number of blocks by which the computational domain was partitioned in each coordinate direction.

Table 3: Summary of Examined Decompositions

a large number of decompositions during a single program run with no memory wasted due to static array dimensioning. All message passing was performed using non-blocking communication primitives with special care taken to interleave communication and computation wherever possible.

As timing data was collected, several runs were reaccomplished to assess the repeatability of the timing data. In the case of the T3D and the Paragon, results were found to be repeatable to well within one percent. However, such was not the case for the SP2 where timing data varied much more dramatically (most likely due to the effects observed in Figure 5). In order to ensure accurate results, all runs on the SP2 were accomplished at least five times and the minimum time observed was used as the execution time. This procedure is similar to that recommended by Thinking Machines in the timing studies conducted by Blosch<sup>1</sup>.

## 5.2 Results

### 5.2.1 Electromagnetic Field Computations

Figure 6 contains a comparison of the magnitude of the computed and exact magnetic fields inside the waveguide. The computed solution was obtained from a 32-node Paragon run using approximately 110,000 grid points with the computa-

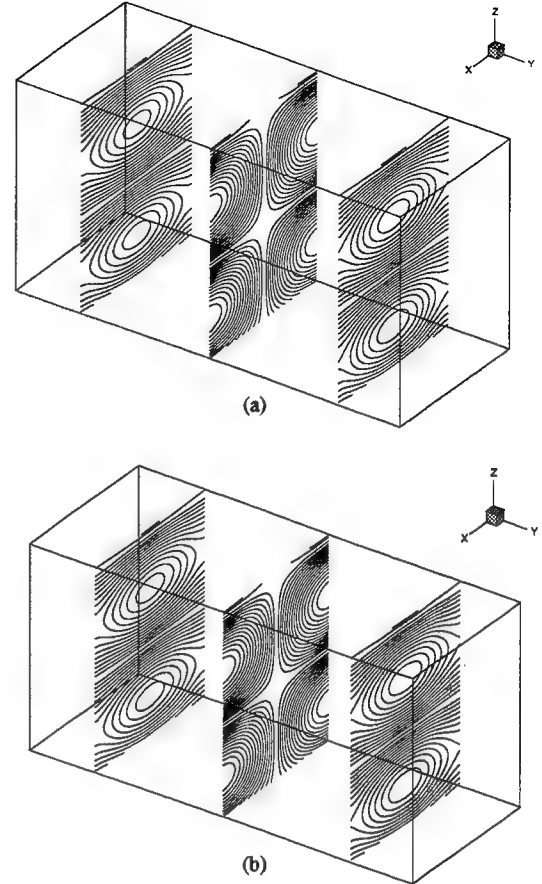


Figure 6: Total Magnetic Field Contours  
(a) exact, (b) computed

tional domain partitioned three-dimensionally in a  $4 \times 2 \times 4$  configuration. In the figure, the y and z axes have been scaled so that the cutting planes located at  $y = 0.6, 1.6$ , and  $2.5$  are unobstructed. The computed and exact solutions are in excellent agreement; in fact, the plots are indistinguishable. While not a formal proof of correctness, it does indicate that the parallel algorithm functioned as intended.

### 5.2.2 Parallel Scalability

The results of the domain-decomposition studies appear in Figures 7-12. Figures 7-9 contain parallel speedup results for the one-, two-, and three-dimensional decompositions, respectively, while Figures 10-12 contain efficiency results. A comparison of the relative performance of the FVTD algorithm for a given dimensionality of decomposition on each of the three machines can be conducted by examining sub-figures a, b, and c of a single figure. On the other hand, a comparison of the sub-figures in a given column facilitates an examination of the effects of the dimensionality of the decomposition for a given platform. It is apparent from the figures that in nearly every case, the two- and three-dimensional decompositions produced performance superior to that of the one-dimensional decompositions. Furthermore,

three-dimensional decompositions exhibited slightly better performance in several instances on the T3D while two-dimensional decompositions were slightly superior in general on the Paragon and noticeably superior on the SP2. This is especially evident in an examination of the efficiency curves of Figures 10-12. These trends in parallel performance correspond quite closely to the topologies of the three machines. The three-dimensional torus structure of the T3D allows each processor six neighboring processors while the two-dimensional mesh structure of the Paragon translates to at most four neighbors for a given computational node. In contrast, the omega network of the SP2 requires that any communication between two processors traverse at least one switch hop and two communication lines. It appears that superior parallel performance is achievable when there is a close agreement between the physical dimensionality of the domain decomposition and the physical topology of the architecture onto which it is mapped. It should be remembered that the speedup and efficiency curves of Figures 7-12 provide one measure of the scalability of the algorithm and do not reflect actual program execution times. For example, although the curves show the scalability of the algorithm on the SP2 to be decidedly less than that on the other two platforms, the superior performance of the RS/6000 when compared to the i/860XP yielded substantially faster run times. In other cross-platform comparisons, the T3D was able to significantly outperform the other two machines both in terms of parallel scalability and in terms of absolute execution speed. This is despite the comparatively poor performance of the message passing (as shown in Figure 5) which is most likely due to the use of PVM.

### 5.2.3 Comparison with Theoretical Model

A comparison of the theoretical and measured parallel speedups for a two-dimensional decomposition ( $R = 64$ ) appears in Figure 13. The theoretical curve was generated by substituting the measured values contained in Table 2 into equation (14). The measured speedup is somewhat over predicted, but this is not surprising since the theoretical model neglects such issues as load imbalance and message contention. It is therefore expected that this model provides a best-case performance prediction. The behavior of the model with respect to variations in the ratio  $t_w/t_c \equiv \chi$  is also shown in the figure. Using the value for  $t_w$  and  $t_c$  found in Table 2 yields the ratio  $\chi = 0.0003$ . A value of  $\chi = 0.0009$  is also shown for reference purposes. It is not unreasonable to expect fairly large variations in  $\chi$  for different decompositions due to differences in memory accessing patterns. In fact, these variations are demonstrated in section 5.2.4.

Although the theoretical model was able to predict the performance of certain decompositions on the T3D to an acceptable manner, such was not the case for the Paragon and the SP2. In these cases, the model drastically over predicted parallel performance. Since it is known that  $\chi$  plays a primary role in parallel performance, a more realistic test problem was conceived to measure  $t_w$ . Instead of utilizing a ring structure in which a single message is in transit at any

given instant, processors were configured as a logical three-dimensional mesh of dimension  $2 \times 2 \times 2$  and  $4 \times 4 \times 4$ . Nearest neighbors in the mesh simultaneously exchanged messages of varying lengths along each coordinate direction and the times for 1000 exchanges in each direction were recorded. The results of this experiment are contained in Figure 14. In the absence of message contention, the message-passing times are expected to be identical regardless of processor number or direction of message exchange since no two messages simultaneously transit the same logical connection between processors. In reality, however, the mapping of the logical three-dimensional structure to a lower-dimensionality architecture results in the mapping of more than one logical connection to the same physical connection. Although all three machines exhibit some degree of variation in message-passing times as the number of processors is increased, the effect is much less dramatic on the T3D. The deviation in the general trend is also small for the SP2, but the variations exhibited in Figure 5 become much more pronounced as the number of processors is increased. In addition to the variation with processor number, the Paragon also exhibits a directional bias in message transfer times which becomes more pronounced as the number of processors increases. In the figure, the  $i, j$ , and  $k$  notation simply identifies a direction along which the message exchanges occurred. The magnitude of the variations in message-passing times relates directly to the quality of the theoretical parallel performance model, and large variations in message-passing times are expected (and observed) to adversely impact the theoretical predictions.

### 5.2.4 Variations in Decomposition Times

The results contained in Figures 7-12 represent the best observed times for a given dimensionality of decomposition, processor number, and grid size. As noted in Table 3, all permutations of a given decomposition were performed for each case. Although each permutation yielded the same number of grid cells on a given processor and the same amount of message traffic, certain decompositions were observed to yield substantially better performance than others. The performance differences were quantified by constructing the ratio

$$\zeta = T_{max}/T_{min}$$

where  $T_{min}$  and  $T_{max}$  represent the minimum and maximum observed run times for each combination of processor number, grid size, and decomposition dimensionality, Figure 15 depicts this ratio for the two-dimensional decompositions on the SP2. Although the trends differed depending on the machine and decomposition approach, variations of similar magnitude were observed for the Paragon and T3D. The sometimes marked variations indicate that memory accessing issues are as important as the dimensionality of the decomposition in achieving good performance. This is to be expected since the RISC processors employed in all machines require a high degree of data locality in order to achieve near-advertised megaflop ratings. Should the domains be decomposed in a manner that precludes locality-

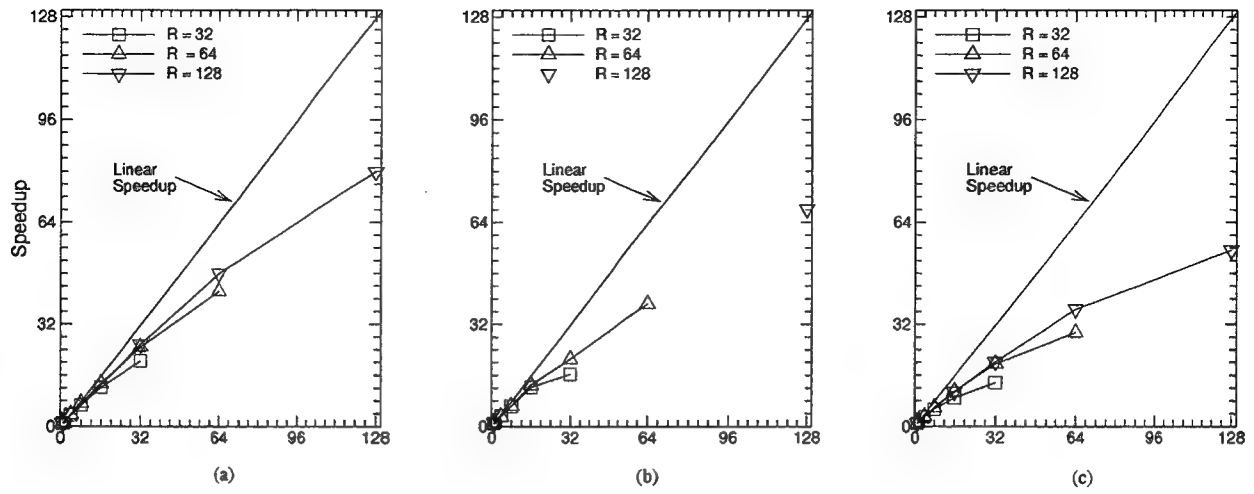


Figure 7: One-Dimensional Decomposition Speedups a) T3D, b) Paragon, c) SP2

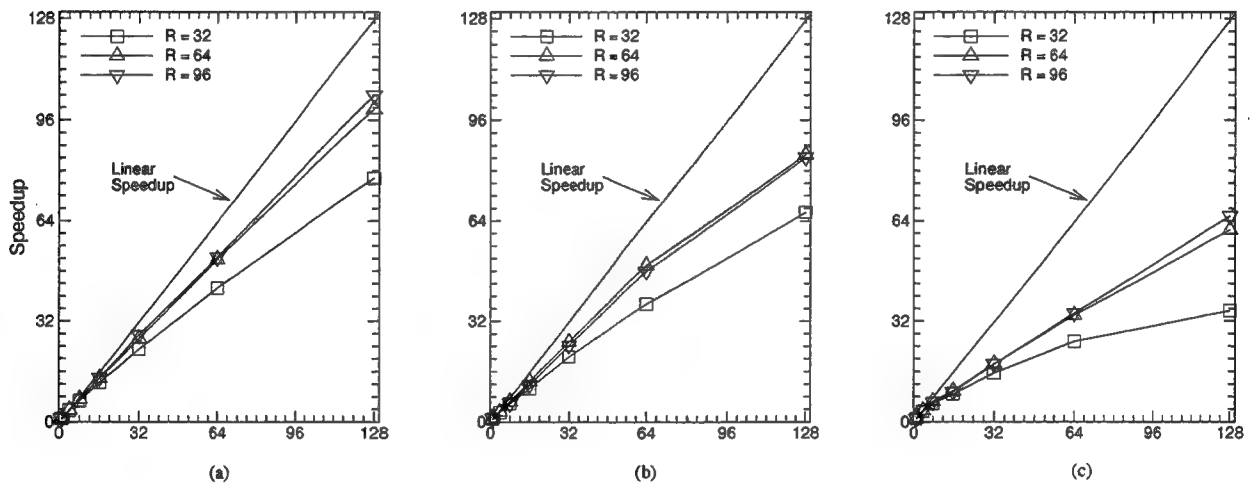


Figure 8: Two-Dimensional Decomposition Speedups a) T3D, b) Paragon, c) SP2

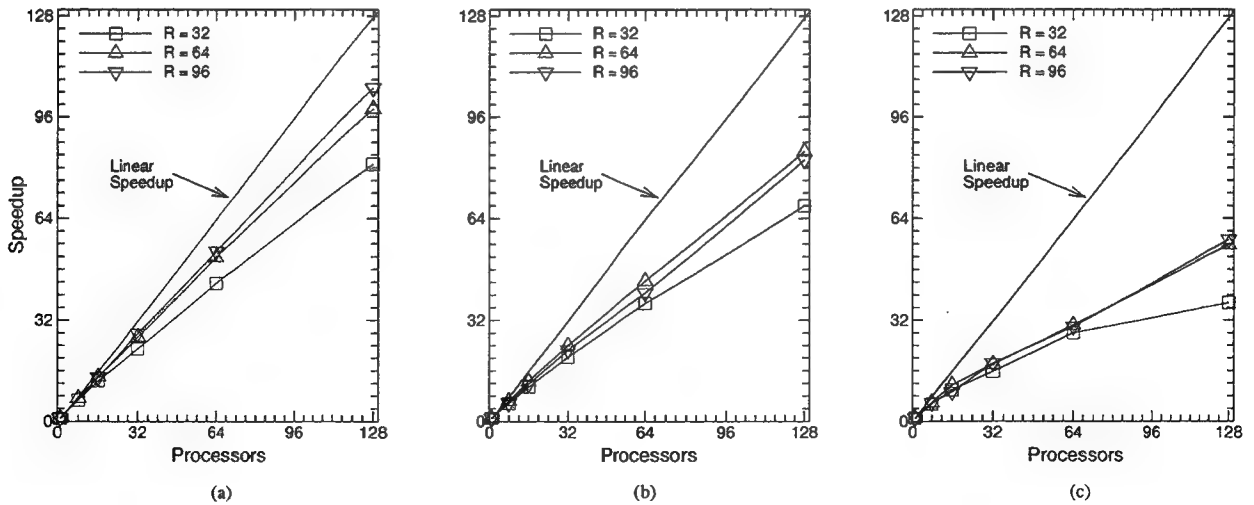


Figure 9: Three-Dimensional Decomposition Speedups a) T3D, b) Paragon, c) SP2



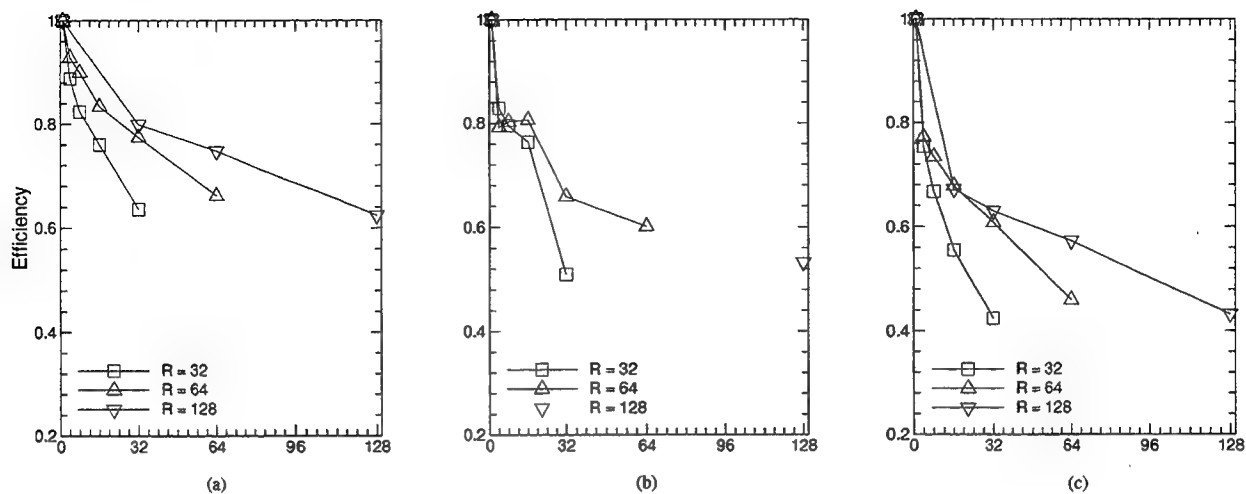


Figure 10: One-Dimensional Decomposition Efficiencies a) T3D, b) Paragon, c) SP2

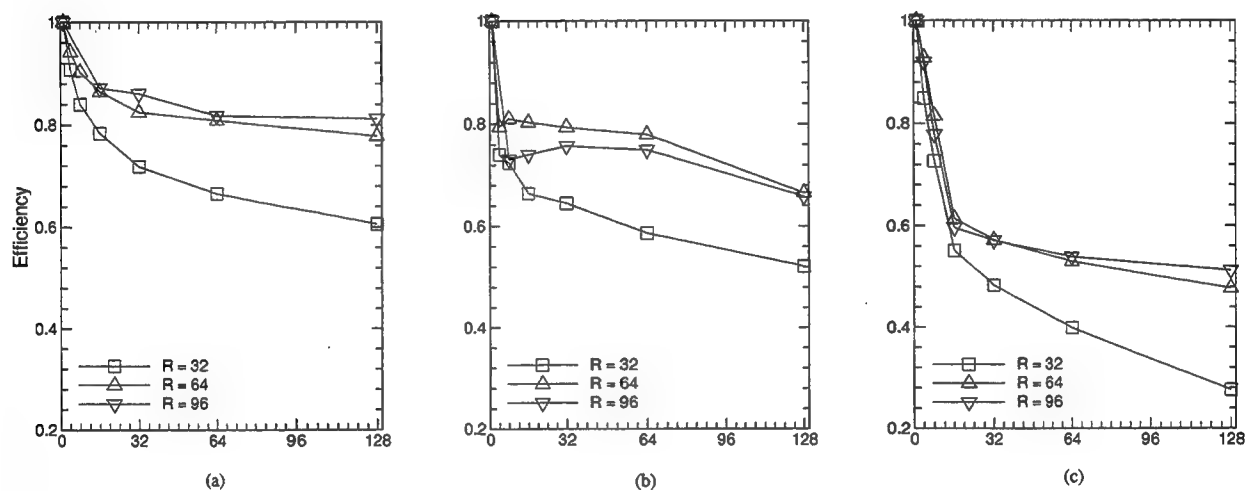


Figure 11: Two-Dimensional Decomposition Efficiencies a) T3D, b) Paragon, c) SP2

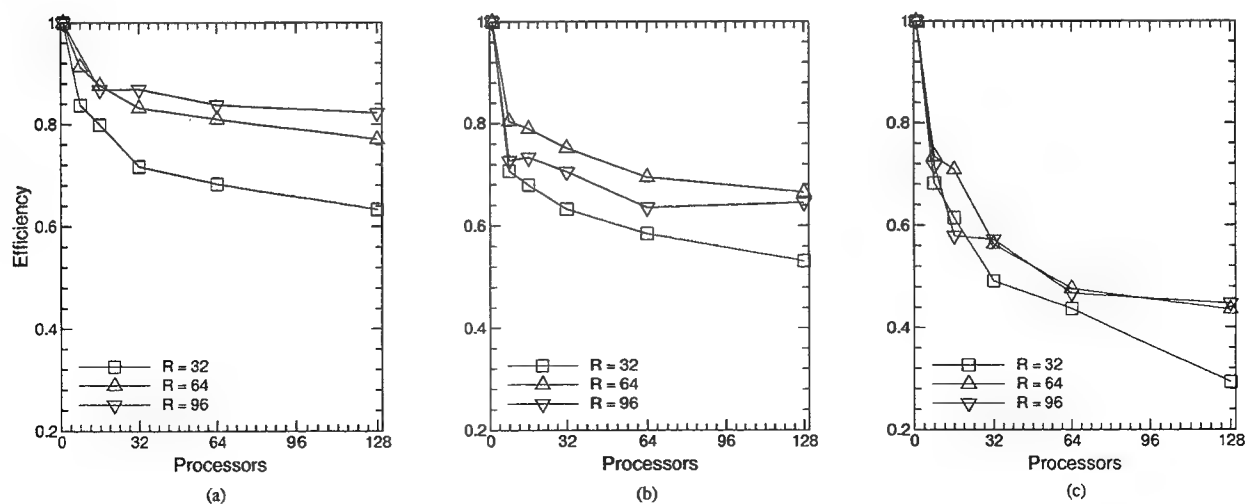


Figure 12: Three-Dimensional Decomposition Efficiencies a) T3D, b) Paragon, c) SP2

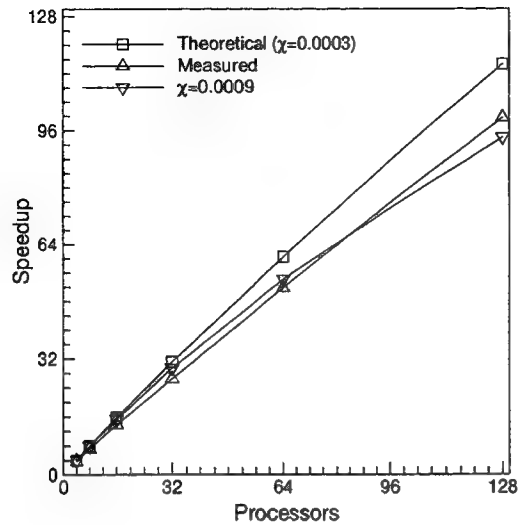


Figure 13: Theoretical and Measured Performance of the T3D  
( $R = 64$ , 2D decomposition)

of-reference, then performance suffers dramatically.

## 6 Conclusions

The relation between the dimensionality of the domain decomposition and parallel performance has been assessed on three modern distributed memory parallel computing platforms using a FVTD algorithm and a rectangular waveguide geometry. Higher dimensionality (two- and three-dimensional) decompositions were found to nearly always outperform one-dimensional decompositions. The performance of the decompositions was found to relate very closely to the topology of the machine on which the algorithm was implemented. In general, machines with higher processor connectivity favored higher-dimensional decompositions.

Despite the fact the classical parallel performance model used in this study accurately predicted performance trends, it occasionally dramatically over predicted the actual performance of the algorithm. This is due to the fact that the model does not account for issues such as message contention which occurs when more than one logical message path is mapped to the same physical connection. The adverse affect of message contention was observed to increase with increasing processor count on all architectures.

Although caution must be exercised when attempting to extend program performance characteristics to other algorithms, because many algorithms designed for solving hyperbolic systems of partial differential equations possess similar data dependencies, the results presented here can be generalized at least to some degree to a large number of explicit hyperbolic (and perhaps even some parabolic and elliptic) partial differential equations solution schemes.

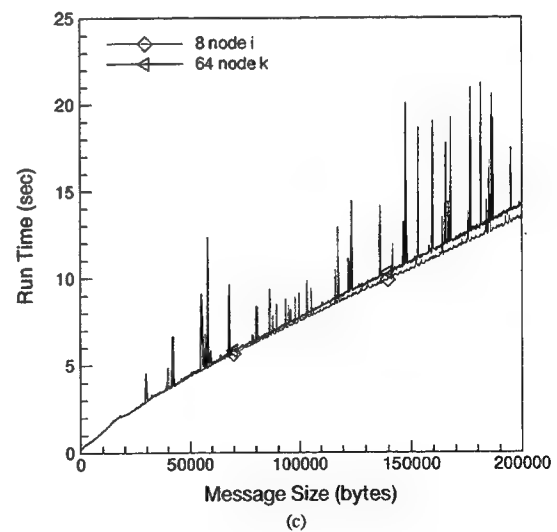
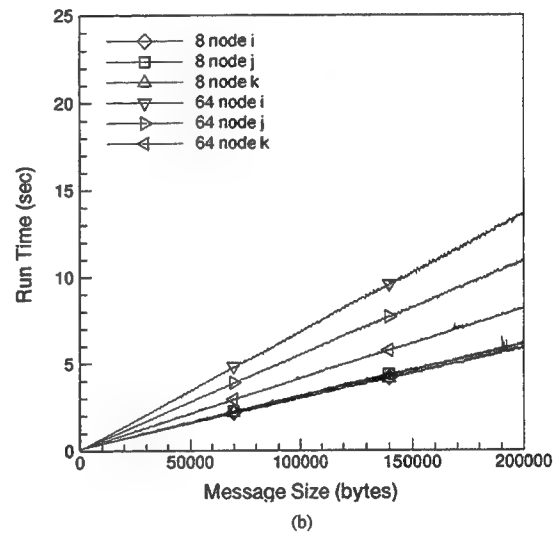
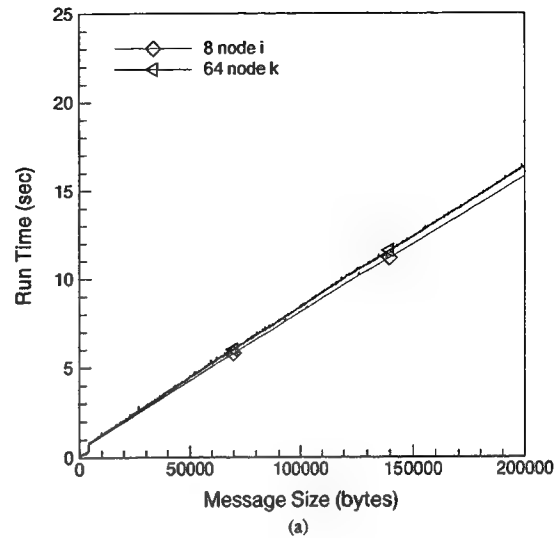


Figure 14: Nearest-Neighbor Message Passing Performance a) T3D, b) Paragon, c) SP2

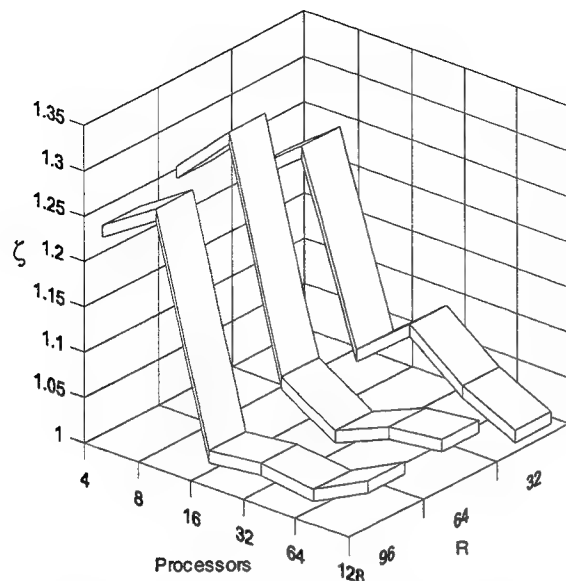


Figure 15: Example of Maximum to Minimum Execution Time Ratio (2D decompositions on SP2)

#### Acknowledgments

The authors wish to thank Dr. Joseph Shang of Wright Laboratories for sponsoring this work and providing the original sequential FVTD computer code.

#### References

- <sup>1</sup> Bloesch, E. L. and Shyy, W., "Parallel Efficiency of Sequential Pressure-Based Navier-Stokes Algorithms on the CM-2 and MP-1 SIMD Computers," AIAA Paper 94-0409, January 1994.
- <sup>2</sup> Hauser, J., and Williams, R., "Strategies for Parallelizing a Navier-Stokes Code on the Intel Touchstone Machines," *International Journal for Numerical Methods in Fluids*, Vol. 15, pp. 51-58, 1992.
- <sup>3</sup> Scherr, S. J., "Implementation of an Explicit Navier-Stokes Algorithm on a Distributed Memory Parallel Computer," AIAA Paper 93-0063, January 1993.
- <sup>4</sup> Shang, J. S., Hill, K. C., and Calahan, D., "Performance of a Characteristic-Based, 3-D, Time-Domain Maxwell Equations Solver on a Massively Parallel Computer," AIAA Paper 93-3179, July 1993.
- <sup>5</sup> Shankar, V., Hall, W. F., Mohammadian, A. and Rowell, C., "Computational Electromagnetics: Development of a Finite-Volume, Time-Domain Solver for Maxwell's Equations," Final Contract Report of contract N62269-90-C-0257, May 1993.
- <sup>6</sup> Stagg, A. K., Cline, D. D. and Carey, G. F., "Parallel, Scalable Parabolized Navier-Stokes Solver for Large-Scale Sim-

ulations," *AIAA Journal*, Vol. 33, No. 1, Jan. 1995.

<sup>7</sup> Wong, C. C., Blottner, F. G., Payne, J. L. and Soetrisno, M., "A Domain Decomposition Study of Massively Parallel Computing in Compressible Gas Dynamics," AIAA Paper 95-0572, January 1995.

<sup>8</sup> Foster, I., *Designing and Building Parallel Programs*, Addison-Wesley Publishing Company, 1995.

<sup>9</sup> PVM and HeNCE Programmer's Manual, SR-2501 5.0, Cray Research, Inc., 1994.

<sup>10</sup> Paragon C System Calls Reference Manual, Intel Corporation, Order Number 312487-003, June 1994.

<sup>11</sup> Snir, M., Otto, S., Huss-Lederman, S., Walker, D. W., and Dongarra, J., *MPI: The Complete Reference*, MIT Press, 1996.

<sup>12</sup> Shang, J. S., "A Fractional-Step Method for Solving 3-D Time-Domain Maxwell Equations," *Journal of Computational Physics* 118, pp. 109-119, 1995.

<sup>13</sup> Southworth, G. C., *Principles and Applications of Waveguide Transmission*, D. Van Nostrand Co., Princeton, New Jersey, 1956.

<sup>14</sup> Balanis, C. A., *Advanced Engineering Electromagnetics*, John Wiley & Sons, 1989.

<sup>15</sup> Mohammadian, A. H., Shankar, V. and Hall, W. F., "Application of Time-Domain Finite-Volume Method to Some Radiation Problems in Two and Three Dimensions," *IEEE Transactions on Magnetics*, vol. 27, No. 5, September 1991.

<sup>16</sup> Steger, J. L. and Warming, R. F., "Flux Vector Splitting of the Inviscid Gasdynamics Equations with Application to Finite Difference Methods," *Journal of Computational Physics*, Vol. 40, pp. 263-93, April 1981.

<sup>17</sup> van Leer, B., "Flux-Vector Splitting for the Euler Equations," Technical Report 82-30, ICASE, September 1983.

<sup>18</sup> Shang, J. S. and Gaitonde, D., "Characteristic-Based, Time-Dependent Maxwell Equations Solvers on a General Curvilinear Frame," AIAA Paper 93-3178, July 1993.

<sup>19</sup> Kumar, V., Grama, A., Gupta, A. and Karypis, G., *Introduction to Parallel Computing*, Benjamin/Cummings Publishing Company, 1994.

# Moment Method Surface Patch and Wire Grid Accuracy in the Computation of Near Fields

Robert Paknys and Leslie R. Raschkowan

Department of Electrical and Computer Engineering  
Concordia University, Montreal, PQ, Canada H3G-1M8  
E-mail: paknys@ece.concordia.ca

**Abstract**—The accuracy of surface patch and wire grid moment method models for the computation of near fields is investigated. A sphere and a flat plate with plane wave illumination are examined.

It is found that wire grids exhibit stronger near field anomalies than surface patches, which have the current more distributed over the surface. Nevertheless, good results can be obtained with a wire grid, provided that a small distance from the wire grid surface is maintained.

The surface patch results are obtained using the *Junction* code. Wire grid results are obtained with both the *MBC* and *NEC* codes. Validation for the sphere is by comparison with an exact solution, and validation for the plate is by comparison with a high frequency UTD solution obtained from the *NECBSC* code.

## 1 Introduction

The near field close to the surface of a complex shape is of great interest in antennas and electromagnetic compatibility. For example, the radiation characteristics of an aircraft antenna are distorted by the fuselage on which the antennas are mounted. Another example is in the assessment of electromagnetic hazards to personnel and equipment on the deck of a ship, in the presence of strong RF and microwave sources.

The method of moments is a suitable methodology for the calculation of fields scattered by bodies of resonant size and smaller. Numerous codes exist, and assessment of their accuracy for the computation of electromagnetic fields has been a topic of on-

going research for many years. Historically, wire grid models were the first methodology which permitted moment method modeling of scattering by complex shapes. Richmond's *Thin Wire* code [1] was a pioneering effort in this direction. His code was later extended significantly by Tilston and Balmain as the *Multiradius Bridge Current MBC* code [2]. The *Numerical Electromagnetic Code NEC* was developed by Burke et al. [3]. The development of surface patch codes such as *Patch* by Rao et al. [4], *Junction* by Hwu et al. [5], the *Electromagnetic Surface Patch Code ESP*, by Newman [6], and others, have further expanded the applicability of the moment method.

For smooth bodies without sharp edges, surface patches can accurately model the surface current. On the other hand, wire grids can also be useful, as an edge current can be more accurately handled by a wire than a patch. A patch cannot represent the current at the patch edge, so a separate "edge mode" is required. Inclusion of edge modes have been shown to enhance the accuracy [7], though their incorporation into a general purpose code is not straightforward. Another reason for using wires is that if open bodies are modeled with NEC, we must use a wire grid model, as its MFIE based patch model is only appropriate for closed bodies.

Although much work has been done on the validation of wire grids and patches for far field calculations, investigations into the near field are relatively scarce. Ludwig [8] examined a 2-D TM polarized wire grid model of a cylinder and found that

though the tangential field is not accurate between the wires, the far field is accurate, provided that the "same surface rule" is met, i.e. that the total surface area of the wires equals the surface area of the true surface being modeled. Later, Paknys [9] extended Ludwig's work and demonstrated that the same surface rule is also optimum for the near field of a 2-D TM cylinder. Other work has examined the use of surface patches in near field computations. Yang et al. [10] examined a 2-D cylinder and demonstrated the equivalence of pulse basis patch currents and filamentary wire currents, provided that the same surface rule is used. Kashyap and Louie [11] compared the surface currents of plates made of either wire grids or patches, and found that the edge wires have to be made thinner to obtain agreement with a patch model. Burton et al. [12] also used a patch model to study near fields. They constructed a sufficiently detailed model that enabled one to examine the leakage through gaps in a door on a closed box. Kemptner [13] computed the near fields of a metallic cube and an airplane, using a patch formulation. His results for a cube agreed well with the measured surface current and electric field.

This paper is an investigation into the accuracy of near zone tangential and normal electric fields for 3-D bodies, as computed from surface patch and wire grid models. A square plate and a sphere with plane wave illumination are used as test cases. The accuracy of the patch models are compared to a UTD solution for the plate, and an exact solution for the sphere. For the wire grid models, the same surface rule and the extent of near field anomalies are investigated.

Section 2 examines the near fields of the plate. Section 3 examines the near fields of the sphere. Section 4 compares two different moment method wire codes, MBC and NEC. Section 5 contains the conclusions.

## 2 Near Field of the Plate

The square plate is  $1 \times 1$  m in size and lies in the  $x-y$  plane with the origin at the center of the plate. A wire grid model that has a grid size  $g = 0.1$  m is shown in Fig. 1. The wire radius is  $a_w = 0.0145$  m, in accordance with the same surface rule. The surface

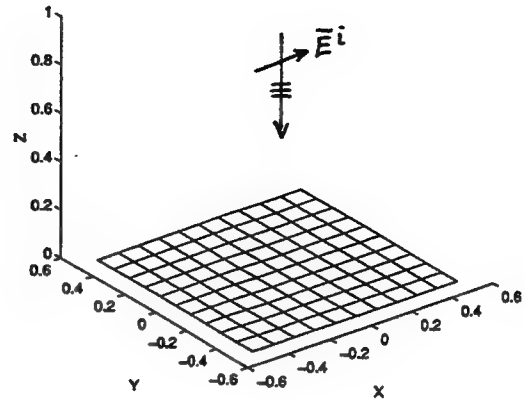


Figure 1: Wire grid model for the  $1 \times 1$  m plate. An  $\hat{x}$  polarized plane wave of 1 V/m is normally incident from above. The field point is in the  $y = 0$  plane.

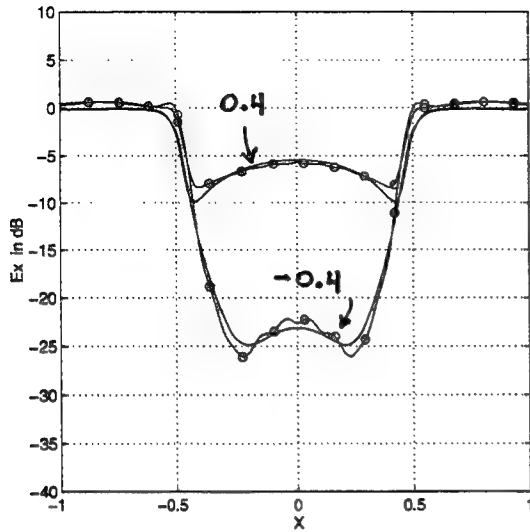
patch model is similar, except that each square area is divided into two triangular patches.

The incident field on the plate is a plane wave with an amplitude of 1 V/m, polarized in the  $\hat{x}$  direction and traveling in the  $-z$  direction, i.e.  $\vec{E}^{inc} = \hat{x}e^{jkz}$ . The field point is in the  $y = 0$  plane. The near field was calculated for several cases, and the total field  $\vec{E} = \vec{E}^{inc} + \vec{E}^{scatt}$  was plotted, using a reference level of 0 dB = 1 V/m. Unless otherwise specified, the frequency is 300 MHz so that  $g = 0.1\lambda$ .

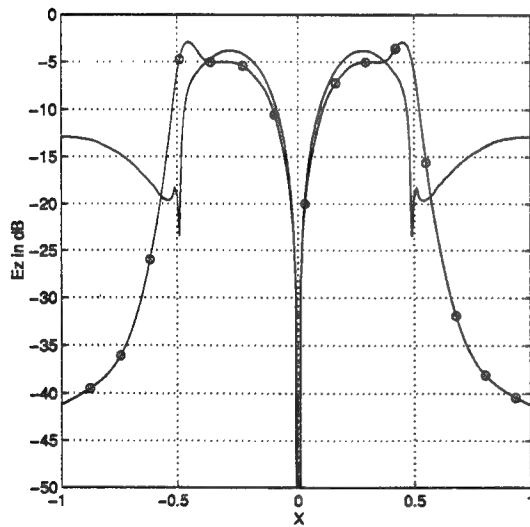
### A. Junction and UTD Models for the Plate

The scattering by a plate does not have an exact solution, so results from the UTD based BSC code [14] were compared with the Junction MM patch code, to establish confidence in the patch model. Fig. 2 shows the tangential field  $E_x$  and the normal field  $E_z$  at  $z/g = \pm 0.04$ .<sup>1</sup> The agreement is within 1.2 dB for  $E_x$  for all values of  $x$  along the plate. The agreement is also within 1.2 dB for  $E_z$  near the plate, but gets worse beyond the plate edges where  $|x| \geq 0.5$ . The reason for this is unknown, but it is speculated that further improvements could be obtained by the inclusion of multiple diffraction effects in the UTD

<sup>1</sup> $|E_z|$  is the same on both sides of the plate so  $z \leq 0$  is not shown.



(a)



(b)

Figure 2: Comparison of UTD (—) and Junction (ooo) for the plate, with patch size  $g = 0.1\lambda$ . (a)  $E_x$ ,  $z/g = \pm 0.4$  (b)  $E_z$ ,  $z/g = 0.4$ . The field point is in the  $y = 0$  plane.

model, and possibly reduced patch size in the patch model. We chose Junction for the subsequent plate model validations.

### B. Extent of the Near Field Anomalies

The near field of the wire grid plate was calculated with NEC and compared to Junction. A frequency of 300 MHz and  $g = 0.1\lambda$  was used. Fig. 3 shows the near field at a distance of  $z/g = \pm 0.4$  and  $z/g = \pm 0.8$ . At  $z/g = 0.4$ , the anomalies in  $E_x$  and  $E_z$  are of comparable magnitude. For  $E_x$ , the onset of anomalies occurs at about  $z/g = 0.4$  on the lit side, and  $z/g = -0.8$  on the shadow side. An increased grid size of  $g = 0.25$  m at 300 MHz was also tried, and anomalies of comparable magnitude were obtained at  $z/g = 0.1$  on the lit side and  $z/g = -0.2$  on the shadow side. This suggests that the onset of anomalies for flat plate structures occurs when  $z/g \approx 0.4$  on the lit side, and  $|z|/g \approx 0.8$  on the shadow side.

The results in Fig. 3 show that for a given observer height, the wire grid results are not as smooth as those obtained in Fig. 2 using Junction. It was found that anomalies of comparable magnitude could also be observed using Junction, but only for field points much closer to the surface.

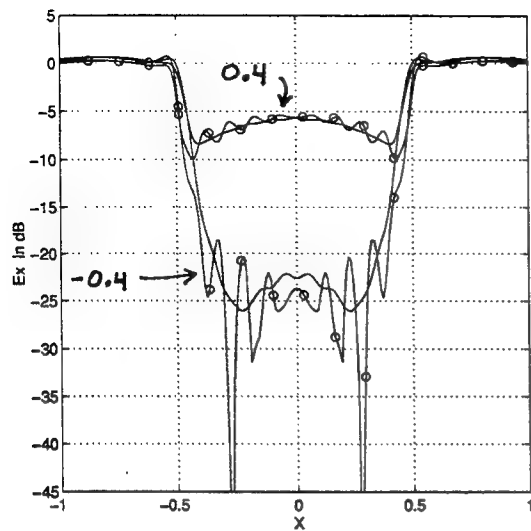
### C. Test of the Same Surface Rule

It is widely accepted that the same surface rule gives the best result for the field radiated by a wire grid model. To test this assertion, NEC was used to compute the near field for several wire radii, and compared to Junction. The frequency was 300 MHz with  $g = 0.1\lambda$ . The field points were chosen as close as possible to the plate, but not so close that the anomalies might obscure the results.

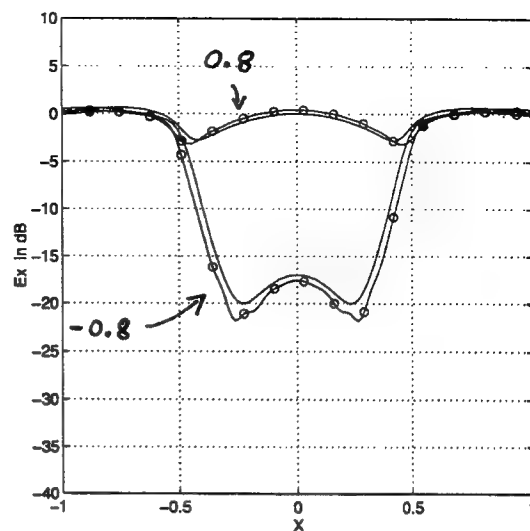
Figs. 4a, b show the tangential field  $E_x$  at  $z/g = \pm 0.8$  and Fig. 4c the normal field  $E_z$  at  $z/g = 0.8$ . It is interesting to note that the same surface rule gives the best result for  $E_x$  but not for  $E_z$ . Hence, it is not possible to choose a wire radius that is simultaneously optimum for both the tangential and normal field components. It is also noted that  $E_x$  is more sensitive to the wire radius than  $E_z$ .

Fig. 4 also shows that  $E_x$  on the shadow side is more sensitive to wire radius changes than on the

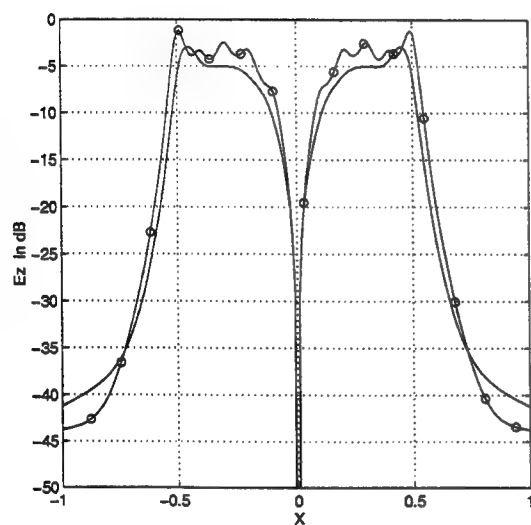




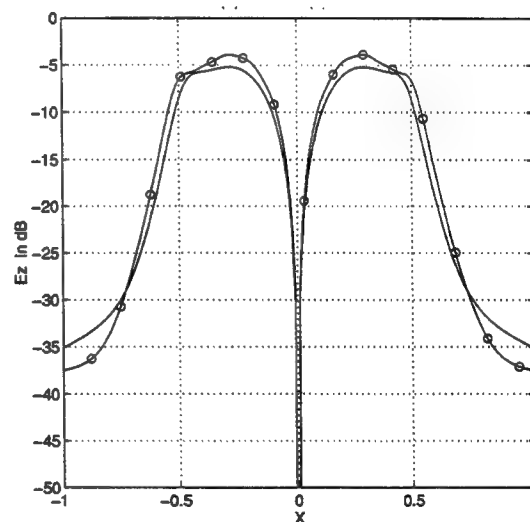
(a)



(b)

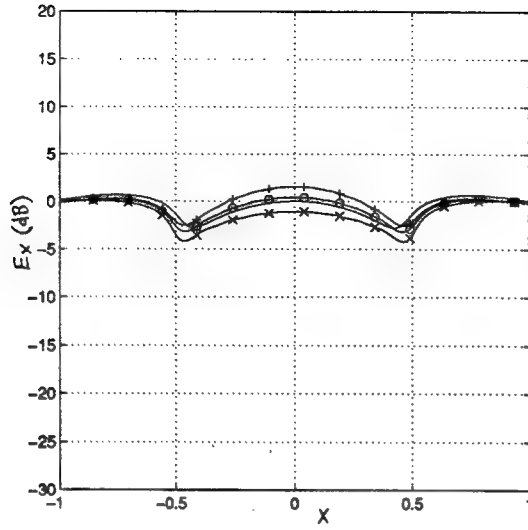


(c)

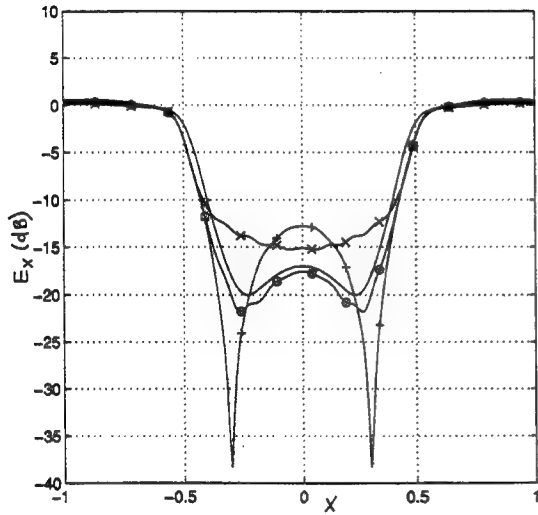


(d)

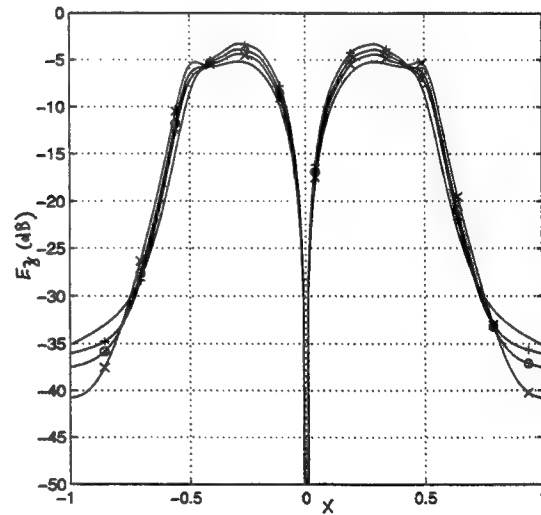
Figure 3: Near field of the plate with grid size  $g = 0.1\lambda$ . Comparison of NEC wire grid (ooo) and Junction surface patches (—). (a)  $E_x$ ,  $z/g = \pm 0.4$  (b)  $E_x$ ,  $z/g = \pm 0.8$  (c)  $E_z$ ,  $z/g = 0.4$  (d)  $E_z$ ,  $z/g = 0.8$ . The field point is in the  $y = 0$  plane.



(a)



(b)



(c)

Figure 4: Effect of wire radius on the near field of the plate, with grid size  $g = 0.1\lambda$ . The wire radius that satisfies the same surface rule is  $a_w = 0.0145$  m. Using NEC, with  $a_w$  (ooo),  $a_w/2$  (+++),  $2a_w$  (xxx). Comparison is with Junction (—). (a)  $E_x$ ,  $z/g = 0.8$  (b)  $E_x$ ,  $z/g = -0.8$  (c)  $E_z$ ,  $z/g = 0.8$ . The field point is in the  $y = 0$  plane.

lit side. This is probably because the accuracy of  $E^{scatt}$  on the shadow side is more critical, as  $E^{scatt}$  must cancel  $E^{inc}$  in order to accurately predict the low field level on the shadow side of the plate.  $E^{scatt}$  was examined separately, and was found to be much less sensitive to wire radius changes than the total field  $E^{inc} + E^{scatt}$ .

A higher frequency of 750 MHz was also tried. The corresponding grid size in this case is  $0.25\lambda$ . The results were still good, with typical errors of 2 dB or less. The sensitivity with respect to wire radius was increased for  $E_x$ , in the shadow. The sensitivity of  $E_z$  remained relatively weak.

#### D. Field Between the Wires

The previous results were taken along  $y = 0$ , which happens to be above a wire. To see what happens in other situations, a contour plot in the  $x-y$  plane was generated, from which some qualitative observations could be made. Also, to obtain a quantitative comparison, a cut along  $y = g/2$ , which is in between the wires, was used. The heights used were the same as before, i.e.  $z/g = \pm 0.4$  and  $z/g = \pm 0.8$ .

It was found that very little changed with respect to the peak to peak amplitude of the near field anomalies. The average field level changed only slightly. By comparing the  $y = 0$  and  $y = g/2$  cases it was found that with  $y = g/2$ ,  $E_x$  increased by 0.7 dB, and  $E_z$  decreased by 1.3 dB. This seems correct, as the wire tends to short out  $E_x$  and support the surface charge that is associated with  $E_z$ .

### 3 Near Field of the Sphere

The wire grid sphere is shown in Fig. 5. The surface patch model is similar, except that each quadrilateral area is divided into two triangular patches. The sphere is centered at the origin, and its radius is  $a = 15$  m. The wire spacing is  $\Delta\theta = \Delta\phi = \pi/8$ . At the equator the grid size is  $g = 5.853$  m and the wire radius is  $a_w = 0.9128$  m. Near the poles the grid size is smaller and the wire radii are adjusted in accordance with the same surface rule.

The incident field is a plane wave with an amplitude of 1 V/m, polarized in the  $\hat{y}$  direction and traveling in the  $+x$  direction. It is given by  $\vec{E}^{inc} = \hat{y}e^{-jkx}$ . In all cases the total field  $\vec{E} = \vec{E}^{inc} + \vec{E}^{scatt}$

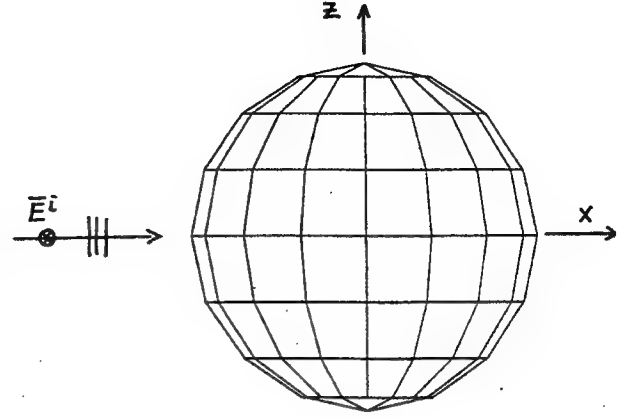


Figure 5: Wire grid model for the sphere. The radius is 15 m. A  $\hat{y}$  polarized plane wave of 1 V/m is incident, travelling along  $+x$ . The field point is at a height  $h$  above the surface, at the equator where  $\theta = 90^\circ$  and  $0 \leq \phi \leq 360^\circ$ .

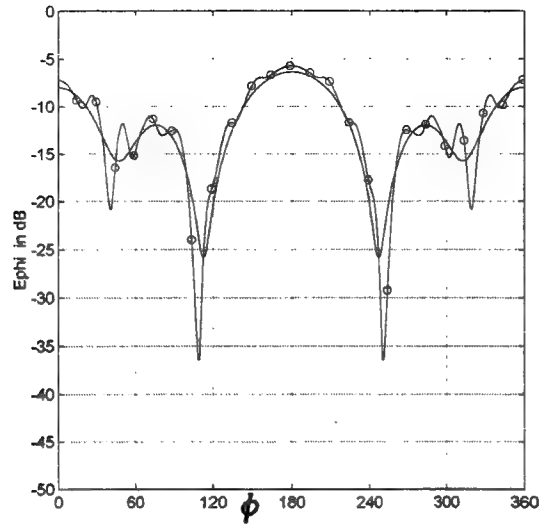
is plotted, using a reference of 0 dB = 1 V/m. The field point is at a height  $h$  above the surface, at the equator where  $\theta = 90^\circ$  and  $0 \leq \phi \leq 360^\circ$ . The frequency was chosen as 12.8 MHz so that  $ka = 1.6$  and  $g = 0.1\lambda$ .

#### A. Junction and Exact Solution for the Sphere

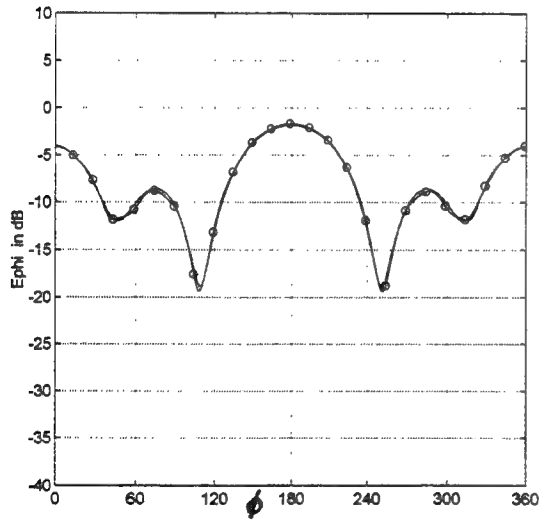
The Junction surface patch model of the sphere was evaluated by comparison with an exact solution obtained from an eigenfunction series [15]. The field was calculated at a height of  $h = 2.34$  m off the surface, so that  $h/g = 0.4$ . The agreement was so close as to be almost indistinguishable, suggesting that Junction is highly suitable for the computation of the near field of a smooth body. As a reference solution, the eigenfunction series was used in the subsequent validations.

#### B. Extent of the Near Field Anomalies

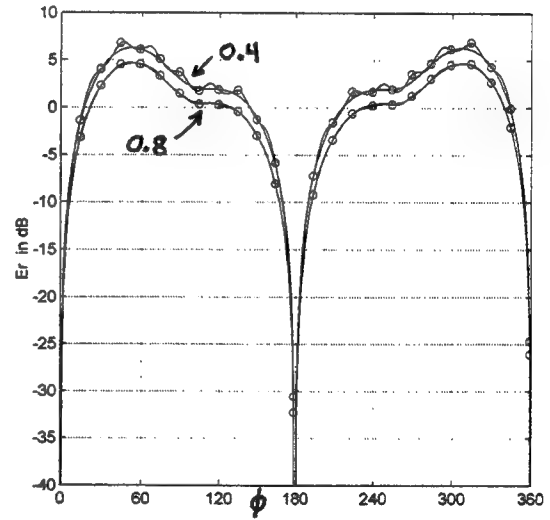
The field was calculated with NEC, at heights of  $h = 2.34$  m and 4.68 m off the surface, so that  $h/g = 0.4$  and 0.8, respectively. Fig. 6 shows that for  $h/g = 0.4$ , on the lit side, the anomalies in  $E_\phi$



(a)



(b)



(c)

Figure 6: Near field of the sphere, grid size  $g = 0.1\lambda$ . Comparison of NEC wire grid (ooo) and exact solution (—). (a)  $E_\phi$ ,  $h/g = 0.4$  (b)  $E_\phi$ ,  $h/g = 0.8$  (c)  $E_r$ ,  $h/g = 0.4$  and  $0.8$ .

and  $E_r$  are of comparable magnitude. For  $E_\phi$ , the onset of anomalies occurs at about  $h/g = 0.4$  on the lit side, and  $h/g = -0.8$  on the shadow side. Similar behavior was noted for the plate, so these aspects appear to be independent of the precise shape of the scattering body.

A higher frequency was also tried. Using  $ka = 4$  and  $g = 0.25\lambda$ , excellent agreement with the exact solution was observed, and we found that  $h/g \geq 0.8$  was still a good criterion for avoiding anomalies.

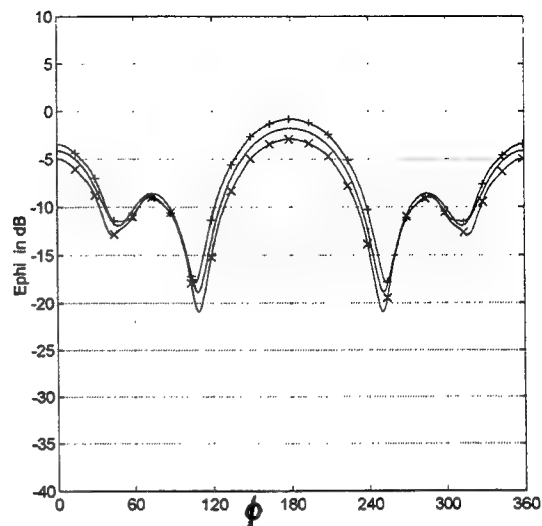
### C. Test of the Same Surface Rule

The field was calculated with NEC at a height of  $h = 4.68$  m off the surface, so that  $h/g = 0.8$ . In Fig. 7 we see that the same surface rule gives the best result for both  $E_\phi$  and  $E_r$ . The cases of too thick wires ( $2a_w$ ) and too thin wires ( $a_w/2$ ) straddle the exact result. (The case using the same surface rule was not plotted, as it is indistinguishable from the exact solution.) This is unlike the plate, where the same surface rule worked for the tangential field, but not for the normal field.

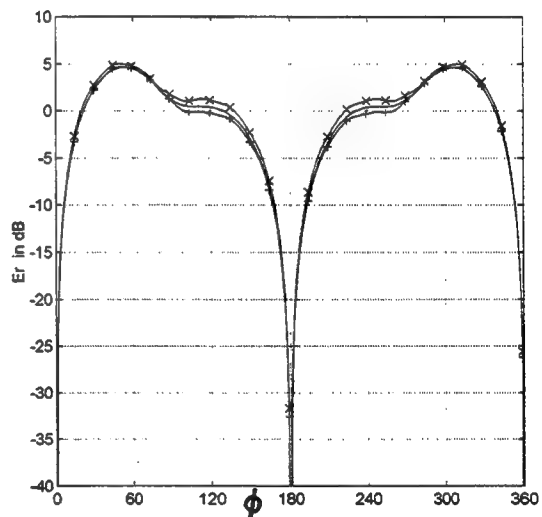
The tangential  $E$  for the sphere was much less sensitive to wire radius changes than the plate. This is not because of the shape, but because the field in the shadow of the plate is much lower. As already mentioned in Section 2 C, errors in the scattered field are more evident when the incident and scattered fields are supposed to be cancelling.

The internal field of a closed body is known to be a sensitive indicator of the quality of a moment method solution, as cancellation of the incident field must take place inside the scatterer. This was not explored here, as there is no corresponding test that can be used for the plate.

A higher frequency using  $ka = 4$  and  $g = 0.25\lambda$  was also tried. It was found that the sensitivity with respect to wire radius of  $E_\phi$  was increased on the shadow side, and hardly affected on the lit side. The sensitivity of  $E_r$  remained relatively weak. Even at this higher frequency, the results remained good, with errors on the order of 1 dB or less when the same surface rule was obeyed.



(a)



(b)

Figure 7: Effect of wire radius on the near field of the sphere, with grid size  $g = 0.1\lambda$  and  $h/g = 0.8$ . The wire radius that satisfies the same surface rule is  $a_w = 0.9128$  m. Using NEC with  $a_w/2$  (+++),  $2a_w$  (xxx). Comparison is with exact solution (—). (a)  $E_\phi$  (b)  $E_r$ .

## 4 Comparison of NEC and MBC

The NEC and MBC wire codes were used to compute the near field of the sphere at  $h/g = 0.4$ . Fig. 8 shows that the positions and amplitudes of the anomalies are very similar. This is noteworthy, as the two codes are quite different, i.e. NEC uses sine and cosine basis functions with point matching, whereas MBC uses piecewise sinusoids and Galerkin's method. Other tests using MBC revealed that the extent of near field anomalies and the dependence on wire radius were very similar to NEC. Hence, the comments made in previous sections with regard to the NEC wire grid models would seem to apply to MBC as well. The square plate was also tried, and similar near field behavior was found using both codes.

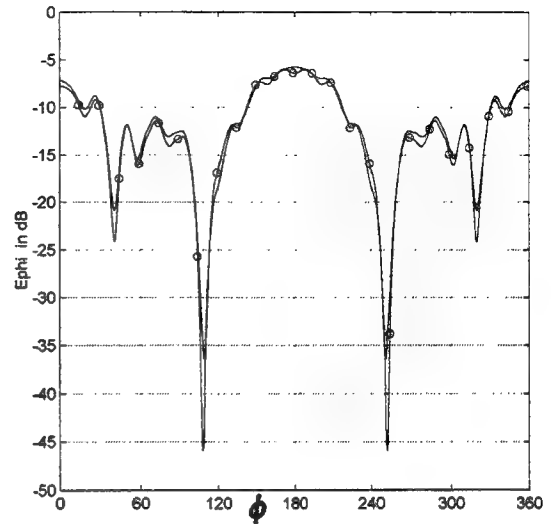
## 5 Conclusion

The near field of a surface patch model is smoother than for a wire grid with the same segmentation size. Nevertheless, a wire grid was found to give good results when the observer is a small distance  $h$  off the surface, provided that  $h/g \geq 0.4$  on the lit side, and  $h/g \geq 0.8$  on the shadow side. This was found to be true for both the plate and the sphere, and was tested for several grid sizes and frequencies.

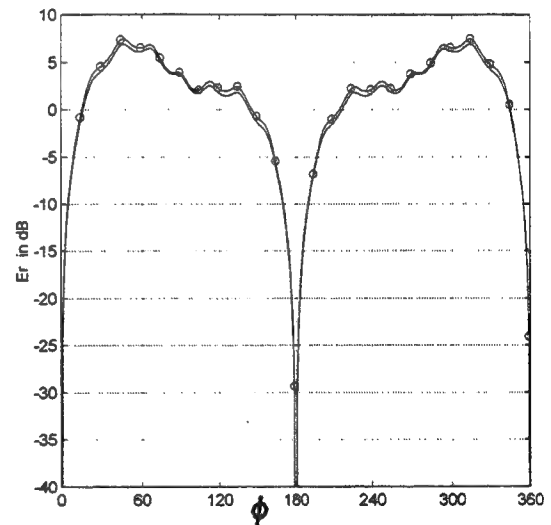
Use of the same surface rule gives the best result for the near fields most of the time but not all of the time. It worked for the tangential  $E$  for the plate and sphere, for the normal  $E$  on the sphere, but not for the normal  $E$  on the plate.

The tangential  $E$  was more sensitive than the normal  $E$  with respect to wire radius, and the greatest errors occurred in the tangential component when the same surface rule was violated. The greatest sensitivity occurred with the field point in the deep shadow, where the incident and scattered fields are supposed to cancel. On the lit side, the effect of changing the wire radius was much smaller.

The type of MM formulation used in the wire codes was not a major factor, as similar results were obtained from the NEC code and MBC code.



(a)



(b)

Figure 8: Comparison of NEC (—) and MBC (ooo) for the sphere, with grid size  $g = 0.1\lambda$  and  $h/g = 0.4$ . (a)  $E_\phi$  (b)  $E_r$ .



## Acknowledgment

This work was partially supported by the National Science and Engineering Research Council of Canada, grant OGP0046227.

Thanks to Mr. Jim Logan of NRAD(NOSC) for helping to make the *Junction* and *NECBSC* codes available to the Concordia University EMC Laboratory, and to Drs. Don Wilton and Ron Marhefka for supplying them to us through the established channels.

## References

- [1] J.H. Richmond, "Radiation and scattering by thin wire structures in a homogeneous conducting medium," *IEEE Trans. on Antennas and Propagat.*, p.365, Mar. 1974.
- [2] M.A. Tilston and K.G. Balmain, "A multiradius, reciprocal implementation of the thin wire moment method," *IEEE Trans. on Antennas and Propagat.*, pp.1636-1644, Oct. 1990. Code description and ordering information: *IEEE AP-S Magazine*, p.61, Oct. 1991.
- [3] G.J. Burke and A.J. Poggio, "Numerical Electromagnetic Code," Technical Document 116, Naval Electronic Systems Command, 18 Jul. 1977.
- [4] S.M. Rao, D.R. Wilton, and A.W. Glisson, "Electromagnetic scattering by surfaces of arbitrary shape," *IEEE Trans. on Antennas and Propagat.*, pp.409-418, May 1982.
- [5] S.U. Hwu and D.R. Wilton, "Electromagnetic scattering and radiation by arbitrary configurations of conducting bodies and wires," *Applied Electromagnetics Laboratory, University of Houston Dept. of Electrical Engineering Tech. Rept.* 87-17, May 23, 1988.
- [6] E.H. Newman, "A user's manual for electromagnetic surface patch code ESP," Department of Electrical Engineering, The Ohio State University ElectroScience Laboratory, Tech. Rep., prepared under Contract DAAG29-81-K-0020 for U.S. Army Research Office, 713402-1, Jul. 1981.
- [7] J.H. Richmond, "On the edge mode in the theory of TM scattering by a strip or grating," *IEEE Trans. on Antennas and Propagat.*, pp.883-887, Nov. 1980.
- [8] A.C. Ludwig, "Wire grid modeling of surfaces," *IEEE Trans. on Antennas and Propagat.*, pp.1045-1048, Sept. 1987.
- [9] R. Paknys, "The near field of a wire grid model," *IEEE Trans. on Antennas and Propagat.*, pp.994-999, Jul. 1991.
- [10] X.H. Yang, L. Shafai, and A. Sebak, "A comparison study on wire grid model and point matching technique with subdomain basis functions," *ANTEM Symposium on Antenna Technology and Applied Electromagnetics, Winnipeg Manitoba, Conference Proceedings* pp.656-661, Aug. 5-7, 1992.
- [11] S. Kashyap and A. Louie, "Surface modelling for EM interaction analysis," *ACES Journal*, Vol.6 No.2, pp.38-52, Winter 1991.
- [12] M. Burton, A. Louie, S. Kashyap and R. Banik, "Penetration of the field of an HF antenna into ammunition lockers on a ship," *IEEE International EMC Symposium Digest*, pp.46-47, Aug. 9-13, 1993.
- [13] E. Kemptner, "Determination of lines of constant phase in the near field of a metallic cube and an air-plane," *IEEE Trans. on Antennas and Propagat.*, pp.897-904, Jul. 1994.
- [14] R.J. Marhefka and W.D. Burnside, "Numerical electromagnetic code- Basic scattering code (version 2), part 1: User's manual," Department of Electrical Engineering, The Ohio State University ElectroScience Laboratory, Tech. Rep., prepared under Contract N00123-79-C-1469 for Naval Regional Contracting Office, 712242-14, Dec. 1982.
- [15] R.F. Harrington, *Time Harmonic Electromagnetic Fields*. New York: Mc Graw-Hill, 1961.

# USING THE FDTD METHOD TO MODEL THE REFLECTION COEFFICIENT OF A VIVALDI TAPERED SLOT ANTENNA FED THROUGH A PLANAR BALUN

G. Biffi Gentili, R. Braccini, M. Leoncini  
Dept. of El. Eng., Univ. of Florence, Florence (Italy)  
R. Evangelisti  
Elettronica, S.p.A., Rome (Italy)

**ABSTRACT** - In this paper, the Finite-Difference Time-Domain (FDTD) method was used to determine the reflection coefficient vs. frequency of a Vivaldi Tapered Dual-Slot Antenna fed through a planar balun. The reflection coefficient at the input port of the feed stripline was determined through the separate computation of the reflection coefficient of the antenna section and the scattering matrix of the balun, assuming that the electromagnetic coupling between these sections was negligible. Experimental results, which were obtained on a prototype of this structure, confirmed the validity of the proposed approach and demonstrate that the coupling between the two sections does not affect the accuracy of the model.

## 1. INTRODUCTION

Vivaldi tapered slot antennas (TSAs) consist of tapered slots etched in the metallization of a dielectric substrate with an exponential contour for the slot edges [1],[2]. These traveling wave antennas provide a symmetric endfire beam with appreciable gain and low sidelobes. Moreover, they offer a wideband performance and are characterized by a very low profile. Single sided or bilateral antennas can be realized with the feeding section integrated on the same dielectric substrate. However, owing to the broadband characteristics of Vivaldi TSA, a proper matching section must be used to couple the antenna with the feeding transmission line.

In this work, the FDTD method was used to determine the reflection coefficient at the input port in the feed stripline of a dual-slot Vivaldi TSA. A planar balun was used to couple the antenna section to the stripline [3],[4]. The FDTD analysis was carried out by splitting the problem in two separate ones: the determination of the reflection coefficient of the antenna section and of the scattering matrix of the balun. Then, assuming that the feeding and radiating sections of the antenna were not electromagnetically coupled, the reflection coefficient at the input section of the stripline was computed. Results were successfully compared

with a few experimental data obtained at Elettronica S.p.A. (Rome) where a prototype of this antenna was built up thus confirming the assumption validity.

Because the coupling between the two sections of the whole antenna can be ignored without adversely affecting accuracy, an FDTD-based equivalent network representation of the whole structure can be then derived which would allow a simple and efficient numerical analysis of the electromagnetic response of these devices. Moreover, this approach allows an accurate refinement of the grid for the two disconnected sections, greatly reducing the need for computational resources thus fully exploiting the capability of the FDTD method.

## 2. ANTENNA CONFIGURATION

A schematic view of the antenna section with the feeding transmission line and the planar balun is depicted in Fig. 1. The balun was designed according to the scheme proposed in [4]. Basically, it consists of a stripline-to-slot transition realized by using two stubs, i.e. one terminating the stripline and the other the slotline which directly feeds the antenna. The overall dimensions for the antenna and the feeding sections are reported in the same figure. This antenna is expected to properly operate in the 6 -18 GHz frequency range.

## 3. FDTD ANALYSIS

The FDTD method [5],[6] consists of the numerical solution of Maxwell's equations in time domain through a finite difference approximation of the partial derivatives which appear in curl operators. A numerical scheme analogous to that of Yee's formulation [7] was implemented, except for a variable grid step size that was introduced to properly describe field behavior in the various parts of the structure. In each simulation, a Gaussian-shaped signal was used as time-varying excitation source. Since simulations were run separately for the antenna and the feeding sections, a brief description of the approach used in each case here follows:

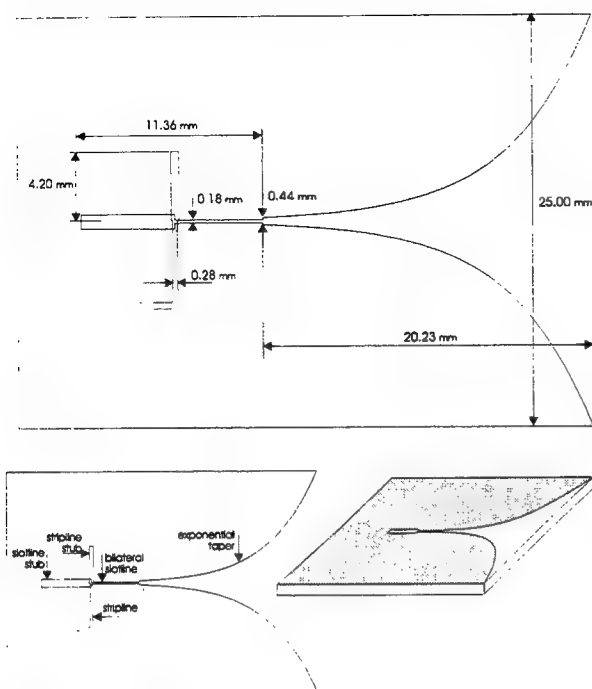


Fig. 1: the Vivaldi antenna and the feeding balun.

#### a) antenna section

The grid step size was linearly changed through the mesh domain to provide a better tracking of the exponential contour. This means that, in the  $x$  direction,  $\Delta x' = \alpha \Delta x$  where  $\Delta x'$ ,  $\Delta x$  are the step sizes of two contiguous cells and  $\alpha$  is a coefficient that would depend on the design parameter of the exponential profile.

A stair casing approximation was used to describe this contour according to the fact that a conformal approach is not expected to give a significant improvement in the results [8]. Due to the symmetries of this dual-slot configuration (see Fig. 2a), the FDTD mesh domain was reduced to a quarter of the total domain by enforcing an electric and a magnetic wall in the  $x=0$  and  $z=0$  planes, respectively. The minimum and maximum grid step sizes along the  $x$  direction were  $90 \mu\text{m}$  and  $130 \mu\text{m}$ , respectively. On the other hand, in the  $y$  and  $z$  directions, a constant grid step size of  $110 \mu\text{m}$  along  $y$  and  $102 \mu\text{m}$  along  $z$  was used. A grid with  $161 \times 296 \times 41$  nodes along  $x, y, z$ , respectively, was obtained. Since the maximum step size is about  $\lambda/50$  at 40 GHz, a reasonable accuracy in the results is expected at least up to that frequency.

A voltage source excited pulse propagation in the slotline. With reference to Fig. 2a, this source was located at AA' plane (i.e. the excitation plane) while

simulation results were stored in terms of voltage at BB' plane (i.e. the input plane). The distances BB' - AA' and BB' - HH' were properly chosen (20 and 30 cells, respectively) in order to remove the evanescent modes launched at the discontinuity planes. The reflection coefficient  $\Gamma_a$  at the input plane of the antenna was determined according to the following procedure:

a.1 - a first simulation was run with the slotline alone terminated on a matched load. This allowed to sample a clean incident signal (i.e. without antenna reflections) at BB' plane. Litva's second order boundary conditions [9] were used to simulate a matched load at the end of the slotline. Since these conditions require the knowledge of phase velocities at the lower and the upper frequency of the range of interest, other FDTD simulations were run before, in order to compute the propagation constant vs. frequency in the slotline;

a.2 - a second simulation was run for the entire antenna section and the total voltage response detected at the input BB' plane. Since this signal would correspond to the incident one previously computed plus the reflected signal from antenna terminals, the latter was then extracted by subtraction. Litva's conditions were used to simulate a matched load at the slotline end, while Higdon's second order boundary conditions [10] were enforced to absorb the waves radiated from the antenna;

a.3 - finally, the reflection coefficient vs. frequency was computed through the ratio of the FFT of the reflected and incident signals.

#### b) feeding section

Since the feeding section is a two-port symmetric network with losses, three of the four parameters of its scattering matrix must be determined. With reference to Fig. 2b, this was carried out as follows:

$S_{11}$  and  $S_{12}$  parameters: a pulse signal was launched in the stripline by exciting the field distribution shown in the same figure, at the excitation CC' plane. In order to properly compute the voltage of the TEM incident wave at the input DD' plane, a first simulation was run by terminating the stripline with a matched load. Due to the TEM propagation in the line (i.e. normal field incidence on the boundary), matching conditions were obtained by enforcing there Mur's first order absorbing boundary conditions [11]. Then, a second simulation was run for the entire feeding section and voltage signals stored at DD' and BB' planes. Since port 2 of the network corresponds to the slotline end, Litva's absorbing boundary conditions were enforced there to simulate a matched load (see a.1 above).  $S_{11}$  and  $S_{12}$  vs. frequency were computed through the ratio of the FFT of the reflected and transmitted signals with the incident one.

$S_{22}$  parameter: with the stripline terminated in a matched load a simulation was run by launching a pulse signal at EE' plane and by storing the total signal at BB' plane, respectively. The determination of  $S_{22}$  immediately follows since the incident signal at BB' plane was already known from the previous simulations (see a.1).

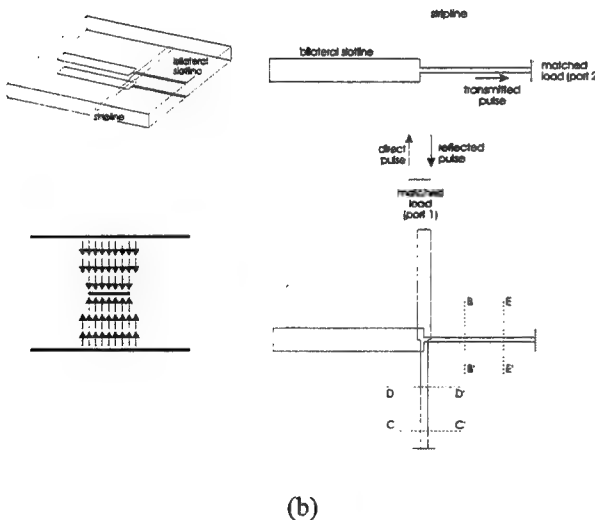
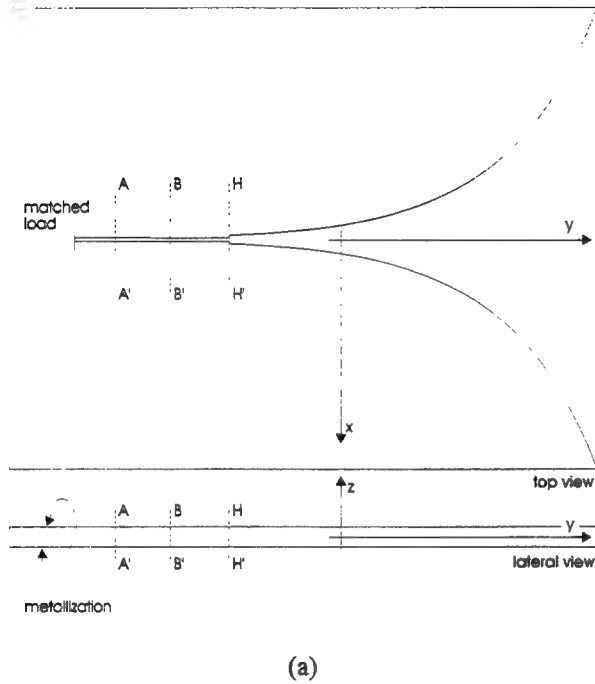


Fig. 2a,b: schematic view of (a) the Vivaldi antenna and (b) the planar balun. In both figures, the reference planes for FDTD analysis are indicated. In Fig. 2b, the exciting field distribution in the feed stripline is also depicted.

The same FDTD grid was used in each simulation. The minimum and maximum grid step sizes were 70  $\mu\text{m}$  and 115  $\mu\text{m}$  along the x direction and 90  $\mu\text{m}$  and 120  $\mu\text{m}$  along the y direction. Again, a constant grid step size of 102  $\mu\text{m}$  along the z direction was used. A grid with 110 x 110 x 41 nodes along x,y,z, respectively, was obtained.

The total reflection coefficient  $\Gamma_{\text{in}}$  at the stripline input DD' plane was determined by using the following equation:

$$\Gamma_{\text{in}} = S_{11} + \frac{S_{12} \cdot S_{21} \cdot \Gamma_a}{1 - \Gamma_a \cdot S_{22}}$$

on the assumption that the antenna and the feeding sections were not electromagnetically coupled.

In this FDTD-derived equivalent network model the radiating section acts as a lumped, frequency dependent impedance loading the feeding network output terminals.

#### 4. RESULTS

In Fig. 3, the reflection coefficient amplitude vs frequency at the input BB' plane of the antenna section is shown. Results indicate the broadband behavior of this kind of antenna up to 40 GHz, with the appearance of local maxima and minima due to the antenna finite dimensions and the dielectric truncation at its far end.

In Fig. 4, the amplitude of the scattering parameters vs frequency for the feeding section is reported. Results obtained for  $S_{11}$ ,  $S_{12}$  ( $S_{21}$ ) and  $S_{22}$  (i.e. Fig. 4a, 4b and 4c, respectively) allow to determine the bandwidth of this matching network which covers the 6-18 GHz operating frequencies. A strong mismatching does appear out of that frequency range.

Results obtained for the reflection coefficient at the input section of the stripline with the antenna loading are shown in Fig. 5. In the same figure, the experimental results measured by using a WILTRON 360 Network Analyzer are reported. Measurements were carried out using a standard SMA connector-to-stripline transition that it was experimentally found to have negligible effects on results accuracy.

The agreement between simulation results and measurements is quite satisfactory and validate the assumption of electromagnetic decoupling between the radiating structure and the feeding network.

#### 5. CONCLUSIONS

In this work the FDTD method was used to analyze the electromagnetic behavior (i.e. in terms of scattering parameters and reflection coefficients), of a

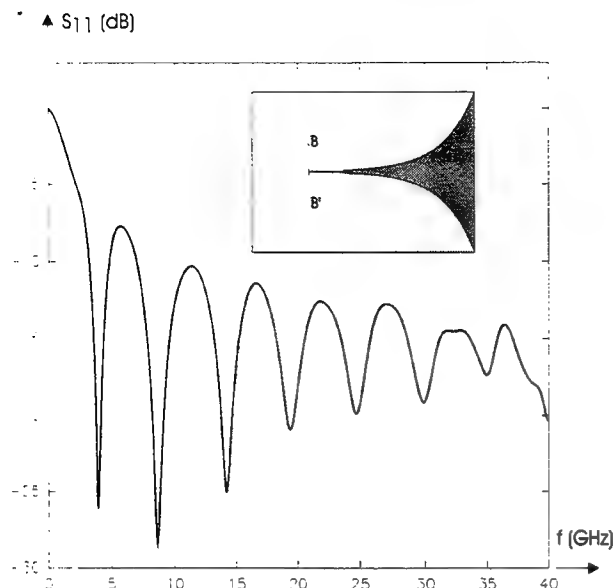


Fig. 3: amplitude vs. frequency of the reflection coefficient of the Vivaldi antenna at BB' plane in the slotline.

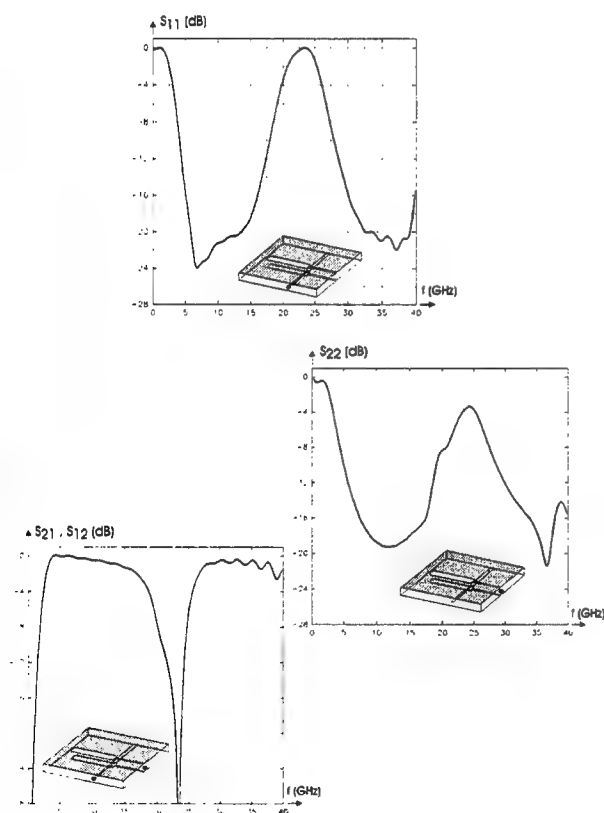


Fig. 4: amplitude vs. frequency of the  $S_{11}$ ,  $S_{12}$  ( $S_{21}$ ) and  $S_{22}$  scattering parameters of the planar balun.

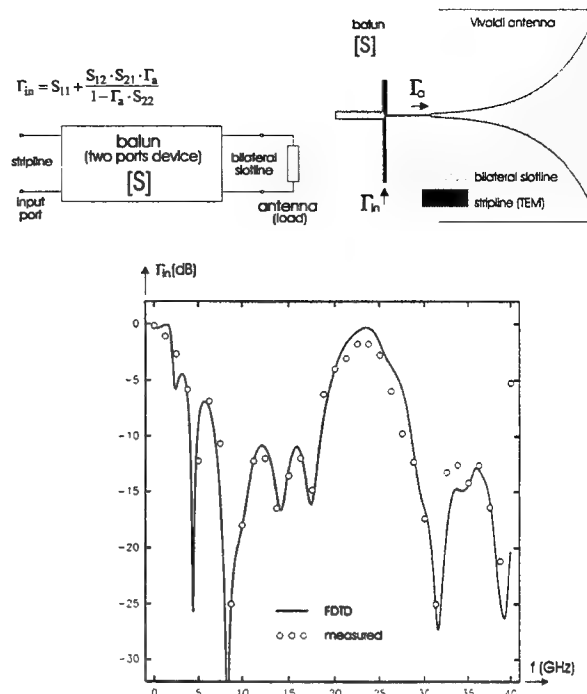


Fig. 5: reflection coefficient of the Vivaldi antenna with the planar balun at the input plane DD' in the stripline: continuous line - numerical results, circles - measured data

Vivaldi tapered dual-slot antenna fed through a planar balun.

Despite of the complexity of the entire structure, a suitable approximation was made which allowed to separately analyze the radiating section and the planar balun. Numerical results did show the intrinsic broadband characteristics of the Vivaldi antenna and allowed the determination of the bandwidth of the balun. Experimental data for the reflection coefficient at the input port of the feed stripline did agree with simulation results, thus indicating the powerfulness of FDTD in dealing with these complex radiating structures and the validity of the proposed approach.

Further investigations will concern the analysis of the scattering matrix of more complex planar baluns and the determination of the electromagnetic coupling between a few adjacent radiating elements, i.e. a subarray of two, three or four Vivaldi antennas.

## REFERENCES

- [1] P.J. Gibson, "The Vivaldi aerial," in *Proc. 9th European Microwave Conf.* (Brighton, U.K.), 101-105, 1979;
- [2] K.S. Yngvesson, T.L. Korzeniowski, Y-S Kim, E.L. Kollberg, J.F. Johansson, "The tapered slot antenna - A new integrated element for millimeter-wave applications, *IEEE Trans. Microwave Theory Tech.*, MTT-37, 365-374, 1989;

- [3] N. Marchand, "Transmission-Line conversion," *Electronics*, vol. 17, 142-145, 1944;
- [4] A. Axelrod, D. Lipman, "Novel planar balun feeds octave-bandwidth dipole," *Microwaves & RF*, 91-92, 1986;
- [5] A. Taflove, K. Umashankar, "The Finite-Difference Time-Domain (FD-TD) method for electromagnetic scattering and interaction problems," *J. Electromagn. Waves & Appl.*, vol. 1(4), 363-387, 1987;
- [6] A. Taflove, "Review of the formulation and applications of the finite-difference time-domain methods for numerical modeling of electromagnetic wave interactions with arbitrary structures," *Wave Motion*, Vol. 10, 547-582, 1988;
- [7] K. Yee, "Numerical solution of initial boundary value problems involving Maxwell's equations in isotropic media," *IEEE Trans. Ant. Propagation*, AP-14, 302-307, 1966;
- [8] E. Thiele, A. Taflove, "FD-TD analysis of Vivaldi flared horn antennas and arrays," *IEEE Trans. Ant. and Propag.*, APS-42, 633-641, 1994;
- [9] K.L. Wu, Z.Q. Bi, C. Wu, J. Litva, "A dispersive boundary condition for microstrip component analysis using the finite-difference time-domain (FDTD) method," *IEEE Trans. Microwave Theory Tech.*, MTT-40, 774-777, 1992;
- [10] R.L. Higdon, "Absorbing boundary conditions for difference approximations to the multi-dimensional wave equation," *Math. of Comp.*, vol. 47, 437-459, 1986;
- [11] G. Mur, "Absorbing boundary conditions for the Finite-Difference approximation of the Time-Domain electromagnetic-field equations," *IEEE Trans. Electromagnetic Compatibility*, EMC-23, 377-382, 1981.



# Finite-Difference Time-Domain Modeling of Light-Trapping in Solar Cells

Todd Marshall and Melinda Piket-May

University of Colorado at Boulder

Campus Box 425

Boulder, CO 80309-0425

Fax: 303-492-2758 Email: mjp@boulder.colorado.edu

**Abstract**—To maximize light-trapping, the absorption of light in the solar cell is maximized. The ways to increase light-trapping are to texture the surfaces of the solar cell and to use anti-reflection coatings. The power spectrum of sunlight also plays an important role in light-trapping. In general, a solar cell consists of multiple layers of dielectric materials. Each dielectric has a complicated surface texture geometry to increase light-trapping. This paper concentrates on solving Maxwell's equations for the general solar cell configuration under illumination from the sun. The absorption and maximum achievable current density are calculated and used to quantify light-trapping in a given solar cell design.

Thin solar cells promise to yield higher current collection than thick solar cells at a lower cost [1]. Low cost solar cells are usually characterized by short diffusion length semiconductors. Most minority carriers created within the distance equal to the diffusion length contribute to the electrical current of a solar cell. Hence, the solar cell must be thin when low quality materials are used. As solar cells decrease in size, the ray-trace model becomes inaccurate as previously demonstrated in [2]. A full-wave Finite-Difference Time-Domain (FDTD) light-trapping model is demonstrated to accurately study light-trapping of thin-film solar cells.

## I. INTRODUCTION

Solar cells are semiconductor devices designed to convert light into electrical power. In order to be cost effective they must be as efficient as possible. Solar cell efficiency is related to the percent of the incident sunlight converted into electrical power. One goal in the design of solar cell devices is to trap and absorb as much light as possible inside the semiconductor. In the language of the solar cell community, the goal is to maximize light-trapping.

One effective way to maximize light-trapping is to coat the semiconductor with a thin film which reduces reflection. This anti-reflective coating ensures a higher percentage of light enters the cell so more light is absorbed. A second effective approach to increase light-trapping is to texture the surface of the solar cell [1], [3], [4], [5], [6], [7], [8], [9]. The texture creates multiple reflections which will lead

to increased light-trapping. The specific design of the textures is critical to maximize light-trapping. All commercial solar cell designs include encapsulation to protect the solar cell from nature. The effect of encapsulation on light-trapping is not well understood. The integration of the anti-reflection coating, encapsulation, and texture into the solar cell design determines the overall light-trapping capacity of a solar cell [10].

Historically, the solar cell industry did not have a means to effectively and accurately predict the light-trapping of a given solar cell geometry. Each solar cell was manufactured and then its efficiency was measured. This is expensive and time consuming. This research fills the need of the solar cell community by quantifying and predicting the light-trapping of a given solar cell design with the aid of numerical models. The result of this research provides industry a means to quantify the light-trapping capability of many different three-dimensional solar cell designs. By modeling light-trapping, the expensive and time consuming step of fabrication is streamlined. Only the promising designs need to be fabricated and tested. This, in turn, frees valuable resources which can be utilized to design more efficient solar cells. The basics of numerical solar cell analysis and the results of the ray-trace analysis were detailed in a companion paper [11]. A reader not familiar with solar cell analysis is encouraged to read the cited paper first.

## II. BACKGROUND

A full-wave model of light-trapping based on the finite-difference time-domain method (FDTD) method is designed to include three-dimensional surface textures, encapsulation, anti-reflection coatings, the energy spectrum of sunlight and the polarization of light. Unlike the ray-trace model, the FDTD model explicitly includes the wave properties of light. The FDTD model accounts for diffraction

due to small surface textures. Small geometric features are common on thin solar cells designed to optimize light-trapping.

This research uses the basic FDTD algorithm first developed by Kane Yee in 1966 to numerically solve Maxwell's Equations and then extended by Taflové. It has been extensively documented so the basic methodology will not be repeated here [12], [13], [14]. The general solar cell geometry with surface texture, encapsulation, and anti-reflection coating is described based on the requirements of the FDTD algorithm. A periodic boundary is introduced to reduce the required computer resources. Sunlight is incorporated into the FDTD model as an electromagnetic source. Finally, the light-trapping model is completed with an explanation of the measurement of light-trapping. The paper concludes with a general discussion concerning the limitations and capabilities of FDTD modeling for solar cells.

#### A. Optical Properties of Matter

The governing equations of light-trapping are Maxwell's equations

$$\frac{\partial \vec{E}}{\partial t} = \frac{1}{\epsilon} \nabla \times \vec{H} - \frac{\sigma}{\epsilon} \vec{E} \quad (1)$$

$$\frac{\partial \vec{H}}{\partial t} = -\frac{1}{\mu} \nabla \times \vec{E} \quad (2)$$

where both the electric field and magnetic field ( $\vec{E}$  and  $\vec{H}$ ) describe the interaction between light and the solar cell. The solar cell is described by its permittivity,  $\epsilon$ , and permeability,  $\mu$ .

The parameters,  $\epsilon = \epsilon_r \epsilon_0$  and  $\sigma$ , describe the optical properties of the solar cell. These properties are quantified directly or through the optical parameters of refractive index,  $n$ , and the extinction coefficient,  $k$ . The quantities are related by

$$\epsilon_r = n^2 - k^2 \quad (3)$$

$$\sigma = 2nk\epsilon_0\omega \quad (4)$$

where  $c$  is the speed of light,  $\omega$  is the angular frequency of light and  $\epsilon_0$  is the permittivity of free space [15].

In actual practice, the light illuminating a solar cell experiences dispersion. Specifically, the index of refraction depends on the wavelength of the incident light. The extinction coefficient also depends on wavelength and determines the amount of light that is absorbed in the solar cell [16]. The index of refraction varies over a wide range from 3.4 to 5.6

which means dispersion effects are important. The extinction coefficient varies by orders of magnitude. The extinction coefficient becomes small as wavelength increases which means little light is absorbed at the higher wavelengths. The higher wavelengths corresponds to lower energy photons. Solar cell designs must accommodate dispersion to ensure accurate light-trapping predictions. Solar cell designs must also overcome the small extinction coefficient by maximizing light-trapping.

#### B. Solar Cell Geometry

Defining the solar cell, or any object, in the FDTD model requires that coefficients be calculated at each field location in the FDTD grid based on the material properties. The coefficients are calculated based on the material parameters of permittivity, permeability, and conductivity. Yee's algorithm imposes a Cartesian grid on the solar cell and surrounding space. Consequently, the location of a field relative to the Yee grid and the material determines the values of the coefficients.

Similar to the ray-trace model, the FDTD model defines the solar cell as a set of materials and interfaces. Each surface separates different materials within the solar cell. The surface normal is not explicitly required by the FDTD model. Unlike the ray-trace model, the solar cell is not restricted to using three-node planar elements. The interfaces are defined as surfaces represented by an arbitrary function of  $x$ - and  $y$ -coordinates,  $K(x, y)$  as shown in Figure 1. The surface is confined to the rectangle between  $Nx1 \leq i \leq Nx2$  and  $Ny1 \leq j \leq Ny2$ . For each field component, the corresponding material parameter is defined. This definition is generalized to multiple surfaces by defining  $N$  interfaces;  $K1, K2, K3 \dots KN$  as necessary.

The encapsulation layer and anti-reflection coatings are incorporated into the FDTD model by defining the necessary number of surfaces. One benefit of using surfaces to define the solar cell is the simplicity of defining a anti-reflection coating with as many layers as needed. In contrast, the ray-trace model only incorporated a two-layer anti-reflection coating while the FDTD model is unlimited. There is no difference between defining the solar cell and the anti-reflection coating, or even the encapsulation layers.

#### C. Periodic Boundary Condition

Scanning Electron Microscope pictures of chemically etched textured solar cells show a periodic structure [1]. This allows us to model the textured

solar cell as an infinite grid. The infinite grid allows us to use a periodic boundary condition which conserves valuable computer resources. In the ray-trace model, the periodic boundary is simple to implement by checking when a light ray hits a periodic boundary. On the contrary, the incorporation of the periodic boundary into the FDTD algorithm is complicated by the light interacting with the entire periodic boundary simultaneously. The light is not localized to a single thin ray at a single point on the periodic boundary. Instead, the light interacts along the entire periodic boundary. The FDTD algorithm models the entire light wave. As a result, the periodic boundary contends with the spatial distribution of power which is inherent to light traveling in various directions.

Since the FDTD algorithm calculates the values of field components, the periodic boundary is defined relative to field locations in the Yee grid. Figure 1 shows the periodic boundary and the Yee field locations at two different heights within the solar cell. The views show two slices of the solar cell which are perpendicular to the periodic boundary. The first view shows a planar slice at a height of  $k$  to coincide with the fields in the bottom half of Yee's unit cell. The  $x$ - and  $y$ -components of the electric field and the  $z$ -component of the magnetic field are contained in the transverse electric plane (TE-plane). Note, the TE-plane has no relation to TE modes in a waveguide. The TE-plane is defined because the electric field components lie in the plane and are transverse to the normal  $\hat{z}$  direction. The field components are drawn as small arrows for the  $x$ - and  $y$ -components of the electric field and as a small circle for the magnetic field. The periodic boundary surrounds the silicon and is confined on the electric fields which are bounded by the rectangle;  $Nx1 \leq i \leq Nx2 + 1$  and  $Ny1 \leq j \leq Ny2 + 1$ . The Transverse Magnetic plane (TM-plane) is shown in the second planar slice. The TM plane is a slice through the solar cell at a height of  $k + 1/2$  to coincide with the upper half of a Yee unit cell. The TM-plane contains the  $x$ - and  $y$ -components of the magnetic field and the  $z$ -component of the electric field. Again, the field components are drawn as small arrows for the  $x$ - and  $y$ -components of the magnetic field and as a small circle for the electric field. By alternatively stacking TM- and TE-planes one on top of the other, any FDTD model of the solar cell is defined. It is sufficient to incorporate the periodic boundary into both TM- and TE-planes separately and then apply the corresponding boundary condition to every

planar stack in the entire FDTD grid.

Each field component in the Yee grid only depends on its nearest neighbors. For example, when calculating  $E_x(i, j, k)$ , the nearest surrounding fields used by the update equation are  $H_z(i, j, k)$ ,  $H_z(i, j - 1, k)$ ,  $H_y(i, j, k)$ , and  $H_y(i, j, k - 1)$ . The nearest neighbors can be found graphically by drawing the smallest contour path perpendicular to the field to be updated [13]. This graphical interpretation of Yee's equations is true for all component fields in the Yee grid. By drawing contours, the fields whose contours do not overlap the periodic boundary are known to be unaffected by the periodic boundary. However, the fields whose contours overlap the periodic boundary are affected by the periodic boundary. The fields that are unaffected by the periodic boundary are colored light grey in Figure 1. While the field components colored dark black in Figure 1 are affected by the periodic boundary. The dark black fields correspond to Yee update equations that need to be modified to incorporate the periodic boundary. As an example, the  $E_x$  field along the boundary,  $j = Ny1$ , uses the surrounding fields;  $H_z(i, j, k)$ ,  $H_z(i, j - 1, k)$ ,  $H_y(i, j, k)$ , and  $H_y(i, j, k - 1)$ . The  $H_z(i, j - 1, k)$  is not the "correct" field to use because of the periodic boundary. Instead, the field to use is  $H_z(i, Ny2, k)$  which comes from "wrapping" the solar cell around the boundary. The field outside of the boundary is replaced by a field inside the geometrically opposing boundary. In general, the periodic boundary is incorporated into the FDTD algorithm by "wrapping" the inner fields on the opposing boundary onto the outer fields on the periodic boundary.

#### D. Light Source

Sunlight is incorporated into the FDTD model based on the standard total-field/scattered-field formulation (TFSF) of a light source [13]. The standard TFSF defines a closed surface. Inside the closed surface, an arbitrary plane wave is excited by adding source fields on the closed surface. The magnitude of the source fields determines the intensity of the light. The direction of the source fields determine the polarization of the incident light. Outside the surface, the source fields are removed so only scattered waves exist outside of the TFSF surface.

The standard TFSF does not include the periodic boundary. The periodic boundary removes the need for a closed TFSF surface which makes the light source trivial to implement in the FDTD model. Instead of a closed surface, a single plane is used. The TFSF plane is placed above the solar cell with a

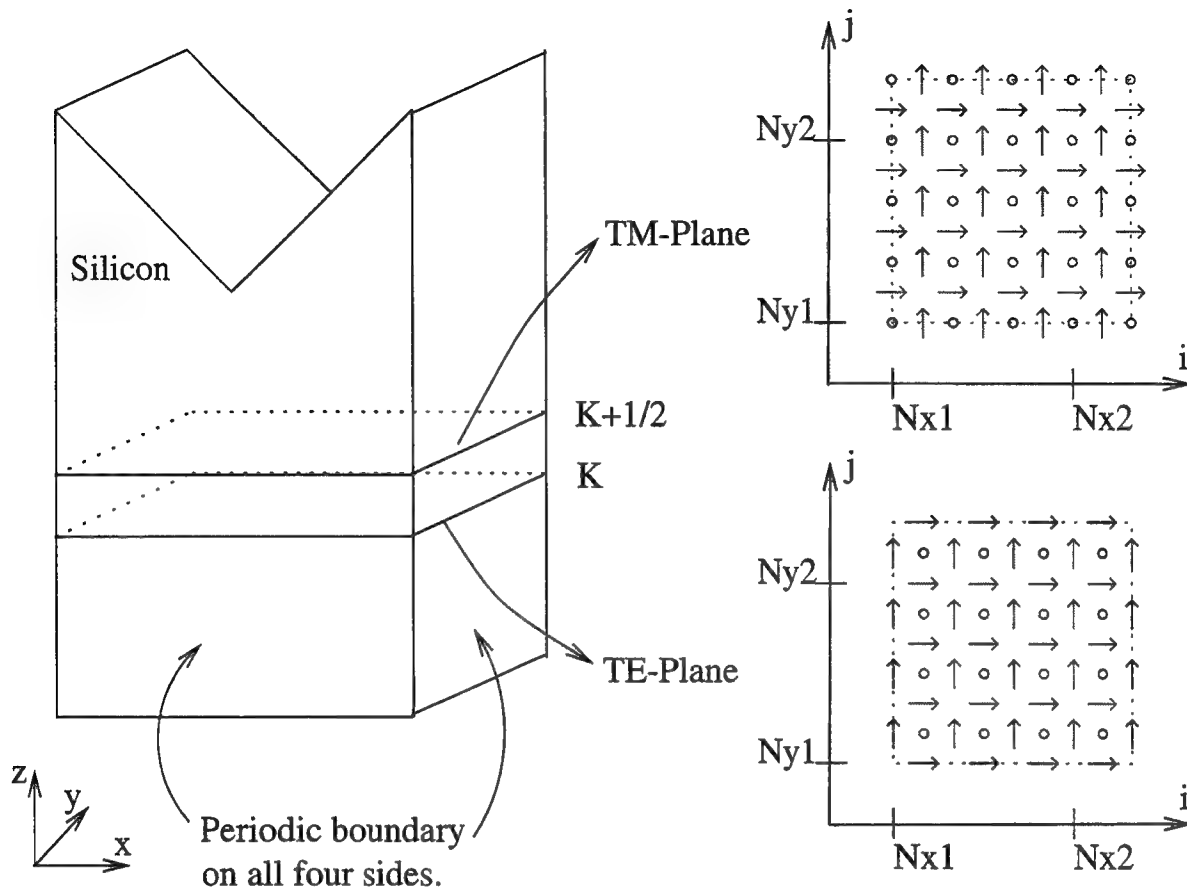


Fig. 1. The periodic boundary in the FDTD algorithm.

constant surface normal in the  $\hat{z}$  direction as shown in Figure 2. Electric and magnetic fields are excited on the TFSF plane which excite the propagation of sunlight in the model. The periodic boundary

ensures that the wave propagates correctly. Light only propagates in the  $\pm\hat{z}$  direction, parallel to the periodic boundary.

#### E. Radiation Boundary Condition

As is the case with the ray-trace model, light which escapes from the solar cell causes numerical errors unless an effective radiation boundary condition is implemented. Unlike the ray-trace model, the radiation or absorbing boundary is difficult to implement into the FDTD model. There are many different solutions to the RBC but they all have inherent limitations [17], [18], [19], [20], [21], [22]. None of the various RBC's perfectly absorb all of the light. Some fraction of the light is always reflected back into the model. The Berenger Perfectly Matched Layer (PML) is the best algorithm for reducing the reflection error [23], [24]. To incorporate the PML into the light-trapping model, the PML is modified to include the periodic boundary. The periodic boundary in the PML is broken into two

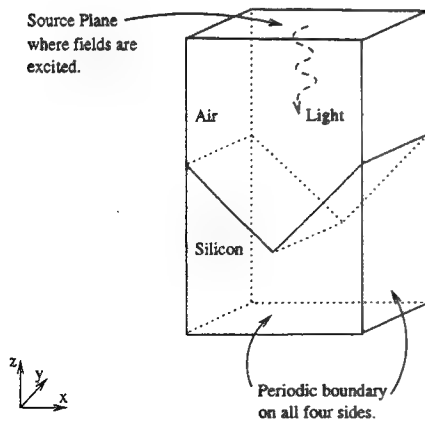


Fig. 2. The light source in the FDTD model with a periodic boundary.

steps, just like the normal Yee periodic boundary. First, the PML update is calculated. Second, the fields are wrapped around the periodic boundary.

#### F. Measurement of Light-Trapping

Absorption is the measure of light-trapping. The index of refraction and extinction coefficient vary as a function of frequency via the relation  $\lambda\omega = 2\pi c$ . The frequency dependent material properties of the solar cell dictate that a general method to calculate absorption is required by the light-trapping model. The FDTD model assumes a plane wave source with a general amplitude modulation to represent light. A common source modulation used is a Gaussian modulated sinusoid because it has a wide spectral content, is smooth, and is finite in duration. The finite duration allows actual computation run times to be reduced over a single sinusoid modulation. Also, the FDTD algorithm is not compatible with sources that are not smooth. The calculation of  $A(\omega)$  is complicated by the frequency dependent solar cell materials and the general input source modulation requirement.

Absorption is the time averaged fraction of power absorbed to power incident which is given by

$$A = \frac{\langle P_{\text{absorbed}} \rangle}{\langle P_{\text{source}} \rangle} \quad (5)$$

and the time average power is

$$\langle P \rangle = \frac{1}{T} \int_{-T/2}^{T/2} P(t) dt \quad (6)$$

The total power absorbed within the solar cell volume,  $V$ , is

$$P_{\text{absorbed}}(t) = \sigma \int_V \vec{E}(\vec{r}, t) \cdot \vec{E}(\vec{r}, t) dv \quad (7)$$

and the total incident power for a plane wave source is

$$P_{\text{source}}(t) = \int_S |\vec{E}(\vec{r}, t)|^2 / \eta_0 ds \quad (8)$$

where  $\eta_0 = 377 \Omega$  is the free space impedance. Since the input source is a modulated sinusoid, direct application of Equation 5 will give the total fraction of light absorbed not the desired fraction absorbed at the center frequency,  $\omega_0$ . Fourier Analysis is used to calculate the desired  $A(\omega_0)$ . Specifically, Parseval's Theorem is used to transform the time average integrals to the frequency domain. Parseval's Theorem for a general function,  $f(t)$ , is

$$\int_{-\infty}^{\infty} f^2(t) dt = \frac{1}{2\pi} \int_{-\infty}^{\infty} |F(j\omega)|^2 d\omega \quad (9)$$

In words, the power contained in the source,  $f(t)$ , due to a single harmonic component,  $\omega_0$ , is  $|F(j\omega_0)|^2 / 2\pi$ .  $F(j\omega_0)$  is Fourier transform of  $f(t)$  evaluated at  $\omega_0$ . It is a now simple matter to decompose the total absorption into power due to each individual harmonic using Parseval's Theorem to find

$$A(\omega_0) = \frac{\sigma \int_V |\vec{E}(\vec{r}, j\omega_0)|^2 dv}{\int_S |\vec{E}(\vec{r}, j\omega_0)|^2 / \eta_0 ds} \quad (10)$$

The time averages are transformed from integrals in the time-domain into a multiplication of the Fourier transformed electric fields in the frequency-domain.  $A(\omega_0)$  in Equation 10 is one measure of light-trapping. The maximum achievable current density (MACD) is another measure of light-trapping which takes into account the solar spectrum. The MACD,  $J_{sc}$ , is defined by

$$J_{sc} = q \int_0^{\lambda_m} F(\lambda) A(\lambda) d\lambda \quad (11)$$

where  $q$  is the charge of an electron,  $F(\lambda)$  is the solar spectrum (usually AM1.5) of the incident light, and  $A(\lambda)$  comes from the solution to Maxwell's equations. Once the absorption spectrum is known (assuming ideal internal spectral response), the MACD is calculated from Equation 11. The ideal internal spectral response makes it possible to study light-trapping without reference to any specific semiconductor material used in the solar cell. In this way, silicon as well as any other semiconductor can be studied based solely on optical considerations.

Both the absorption,  $A(\lambda)$ , and the MACD are used to quantify light-trapping. In the strict sense, absorption is the pure measure of light-trapping. Absorption quantifies how the incident light is absorbed as a function of wavelength but ignores the spectral content of the sunlight. On the other hand, the MACD integrates the effects of both the absorption and solar spectrum into a single quantity,  $J_{sc}$ . The MACD gives a more telling characterization of the real operational solar cell than absorption, without limiting itself to any particular semiconductor.

#### G. Limitations and Capabilities

The primary limitation of the FDTD model of light-trapping is due to limited computer resources. For example, a modest silicon solar cell which is  $1 \mu\text{m}$  thick with a periodic boundary has a total volume of  $1 \mu\text{m}^3$ . The total number of unit cells is  $160^3$ . The total memory requirement is approximately 188 megabytes. Today's standard personal

computer has 16 megabytes of memory, much less than required by the model. The FDTD model falls short of the ray-trace model in this regard.

The FDTD model of light-trapping assumes the geometric features of the solar cell are periodic which reduces computer resource requirements. The solar cell is described by multiple layers of dielectrics. Each dielectric has a complex surface structure, i.e. perpendicular slats, pyramid, tilted-pyramid ... or any surface described by the function,  $K(x, y)$ . Multiple layer anti-reflection coatings are also included in the model. Modern solar cell designs as thin as  $0.5 \mu\text{m}$  are potentially very cheap because of their low mass per unit of performance [25]. The combination of the FDTD algorithm, general texture shapes, and anti-reflection coatings enables the solar cell designer to model and design thin solar cells based on light-trapping more accurately than is possible with any ray-trace model.

### III. FULL WAVE MODEL LIGHT-TRAPPING ANALYSIS

In this section, the finite-difference time-domain model is applied to the light-trapping analysis of thin silicon solar cells. The thickness of the solar cell is approximately equal to the wavelength of light. The goal of the FDTD model is to accurately predict absorption in thin films. The cost of accuracy is the model's dependence on powerful and expensive computers. Unlike the ray-trace model, the FDTD model is not able to execute on a personal computer with only one megabyte of memory. All the light-trapping analysis presented in this section are executed on Cray supercomputers.

#### A. Thin Cell

Figure 3 compares the accuracy of the FDTD and ray-trace models. The absorption spectrum is calculated for a thin,  $0.75 \mu\text{m}$ , planar solar cell. The ray-trace model calculates the average absorption. The FDTD model correctly accounts for the wave nature of light. The FDTD model successfully predicts the maxima and minima. Figure 3 clearly demonstrates the FDTD model is more accurate than the ray-trace model. Note, the analytic solution is not valid for textured solar cells.

#### B. The Maximum Achievable Current Density and Light-Trapping

The light-trapping capability of a thin silicon solar cell is explored in this subsection. By varying the front and rear surface textures of a  $0.75 \mu\text{m}$  thick solar cell, the light-trapping capability of some

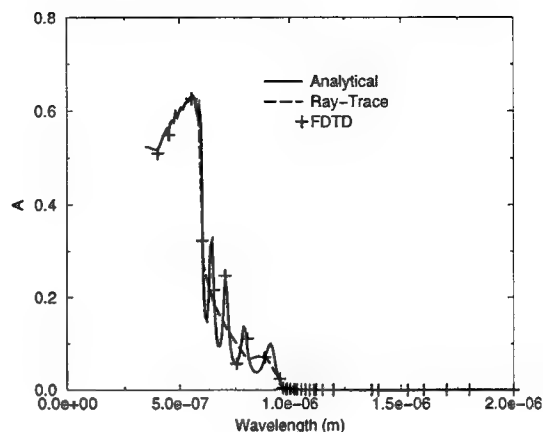


Fig. 3. The absorption of light by a  $0.75 \mu\text{m}$  untextured solar cell.

promising designs is determined [1], [3], [4], [5], [6], [7], [8], [9]. Figure 4 shows the geometric layout of five solar cells analyzed with the FDTD model. The height of all surface textures is a quarter of the thickness of the cell ( $h = t/4$ ). The peak angle of all surface textures is  $70.4^\circ$ . All the cells are illuminated by AM1.5 sunlight. Each cell in Figure 4 is  $0.75 \mu\text{m}$  thick. For the planar solar cell, the  $0.75 \mu\text{m}$  thickness is the distance between the front and rear surface of the silicon slab. For the perpendicular slat solar cell, the definition of thickness is not obvious. Figure 4 has two parallel dotted lines drawn thru each cell. The distance between the two lines is the thickness. The thickness for the perpendicular slat solar cell is not simply the distance between the front and rear surface peaks. Thickness is defined such that different solar cells with equal cross subsectional area,  $w^2$ , and equal thickness,  $t$ , have equal mass. This definition of thickness ensures a valid comparison between textured and non-textured solar cells always exists. Mass is directly proportional to volume. Thickness is equivalently defined using volume. Two solar cells that are both  $t$  microns thick have the same volume per cross subsectional area. For the planar solar cell, the volume of the unit cell is  $tw^2$ . The thickness for the planar solar cell is  $t = v/w^2$ . In general, thickness is defined as  $t = v/w^2$ . The volume and cross subsectional area are the same for each of the cells in Figure 4. The ratio between volume and cross subsectional area remains constant such that  $t = v/w^2 = 0.75 \mu\text{m}$ . Figure 5 summarizes the results of the FDTD light-trapping analysis. All of the textured  $0.75 \mu\text{m}$  solar cells increase the absorp-

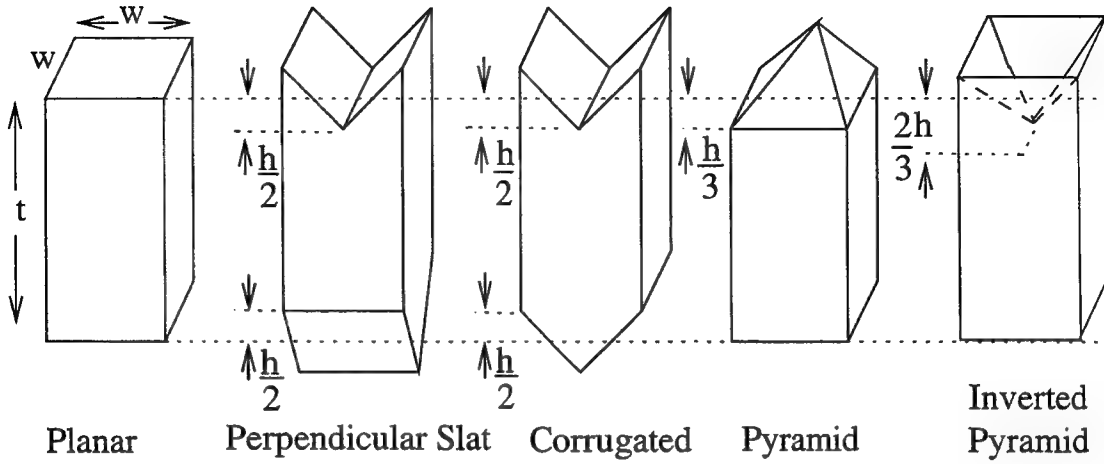


Fig. 4. The thin solar cells analyzed with the FDTD model ( $t = 0.75 \mu\text{m}$ ,  $h = t/4$  and  $\theta = 70.4^\circ$ ).

TABLE I  
THE MACD OF DIFFERENT  $0.75 \mu\text{m}$  THICK SOLAR CELL  
DESIGNS.

Design	MACD ( $\text{mA}/\text{cm}^2$ )
Planar	10.4
Corrugated	15.8
Inverted Pyramids	16.9
Perpendicular Slats	17.3
Pyramids	18.1

tion compared to the planar solar cell. The corrugated slat and the inverted pyramid designs do not perform as well as the perpendicular slat design. The perpendicular slat and pyramid designs achieve at least 50% more absorption than the planar solar cell at the shorter wavelengths. The maximum achievable current density (MACD) under AM1.5 illumination for each of the  $0.75 \mu\text{m}$  designs is tabulated in Table I. The perpendicular slat design has a MACD which is 66% greater than the planar solar cell. The ray-trace model predicts a 12% improvement when the perpendicular slat and planar solar cells are  $50 \mu\text{m}$  thick. The effect of texturing is more important as the solar cells thickness decreases. The solar cell with the front pyramid surface texture has the highest MACD of  $18.1 \text{ mA}/\text{cm}^2$ . This is contrary to the ray-trace prediction that the perpendicular slat solar cell has the higher MACD.

### C. Where are the Photons Absorbed?

The ray-trace model [11] shows that the MACD is not the best figure of merit for light-trapping. Based

solely on the MACD and the ray-trace model, the best light-trapping design is a thick solar cell with a front surface texture. The MACD makes the false assumption that every absorbed photon contributes to the net current of a solar cell. On the contrary, the net current depends on where the photons are absorbed and the quality of the semiconductor.

What is the generation rate for a thin textured solar cell? The generation rate,  $G(\vec{r}, \omega)$ , must satisfy

$$F(\omega)A(\omega) = \int_V G(\vec{r}, \omega) dv \quad (12)$$

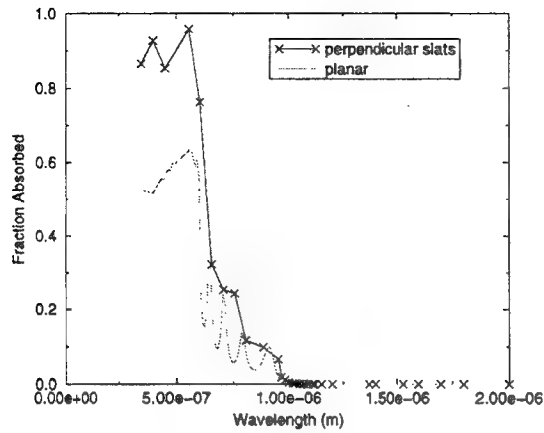
where  $F(\omega)$  is the solar spectrum and the total absorption,  $A(\omega)$ , is given by Equation 10. Substitution of Equation 10 into Equation 12 leads to the generation rate of

$$G(\vec{r}, \omega) = F(\omega) \frac{\sigma |\vec{E}(\vec{r}, j\omega)|^2}{\int_S |\vec{E}(\vec{r}, j\omega)|^2 / \eta_0 ds} \quad (13)$$

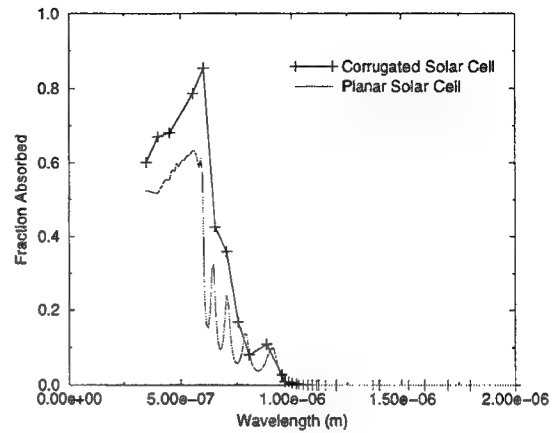
In words, the generation rate is directly proportional to the absorption density. From Equation 13 and Equation 10, the absorption density is  $G(\vec{r}, \omega)/F(\omega)$ . The absorption density (the fraction of incident light absorbed per unit volume) is calculated directly by the FDTD model.

Even though it is beyond the scope of this research to use the absorption density to solve the continuity equation, valuable information is gained by looking at the absorption density.

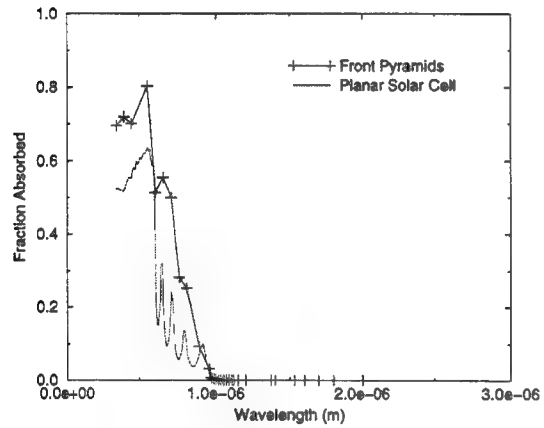
Figure 6 shows the calculated absorption density in the  $xz$ - and  $yz$ -planes for the planar solar cell. The wavelength of light is  $0.35 \mu\text{m}$ . The extinction coefficient of silicon at this wavelength is large which



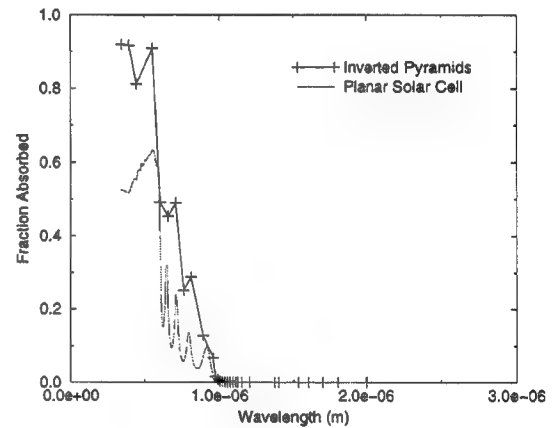
(a) Perpendicular Slats



(b) Corrugated Slats



(c) Pyramids



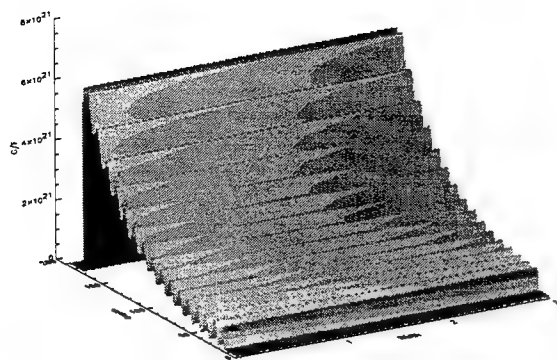
(d) Inverted Pyramids

Fig. 5. The light-trapping capability of different  $0.75 \mu\text{m}$  thick solar cell designs.

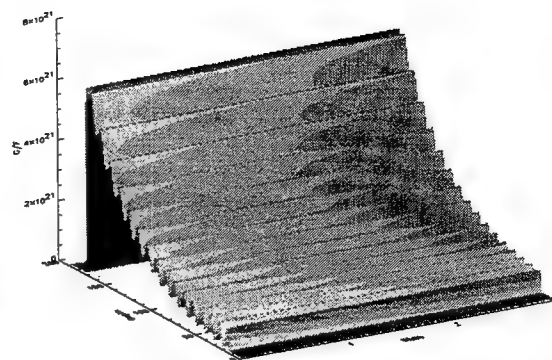
leads to the rapid exponential decay of absorption seen in Figure 6. Figure 7 shows the absorption density for the same solar cell except the wavelength of light is  $0.70 \mu\text{m}$ . The low extinction coefficient leads to a uniform average absorption density. The absorption density at the front and rear sides of the solar cell is the same. The FDTD results shows variations in the absorption density caused by the interference of light. Figure 8 illustrates the location of the  $xz$ - and  $yz$ -planes.

The calculated absorption density for the perpendicular slat solar cell is shown in Figure 9. The wavelength of light is  $0.35 \mu\text{m}$ . Unlike the planar solar cell, the absorption density has an intricate profile. Figure 9 shows most of the light is absorbed near the front surface. The similar effect occurs in the planar cell. Figure 9 shows a sharp peak in the absorption density at the peak of the front surface texture. Figure 10 shows the absorption density for the perpendicular slat solar cell at a wavelength of  $0.70 \mu\text{m}$ . Light reaches the back surface of the solar



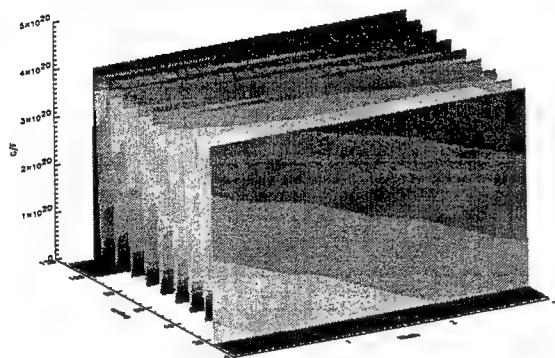


(a) Absorption density in the xz-plane

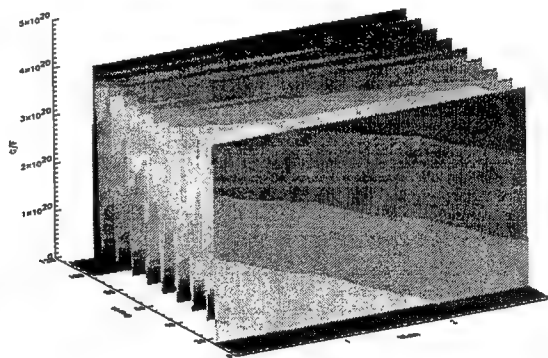


(b) Absorption density in the yz-plane

Fig. 6. The absorption density for the 0.75  $\mu\text{m}$  planar solar cell with  $\lambda = 0.35 \mu\text{m}$ .



(a) Absorption density in the xz-plane



(b) Absorption density in the yz-plane

Fig. 7. The absorption density for the 0.75  $\mu\text{m}$  planar solar cell with  $\lambda = 0.70 \mu\text{m}$ .

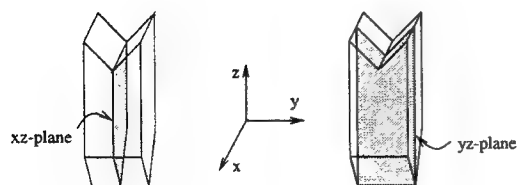


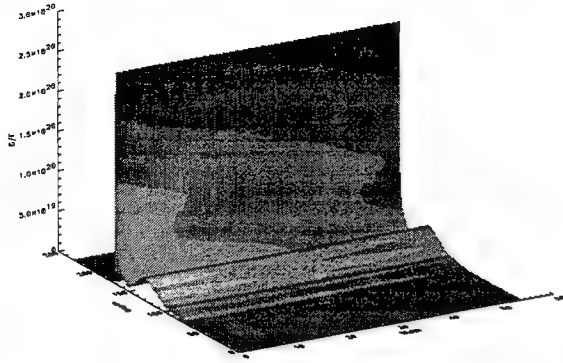
Fig. 8. An illustration of the xz- and yz-planes.

cell. Unexpectedly, the back side of the solar cell has the highest absorption density. The high absorption density at the rear surface is not predicted by the

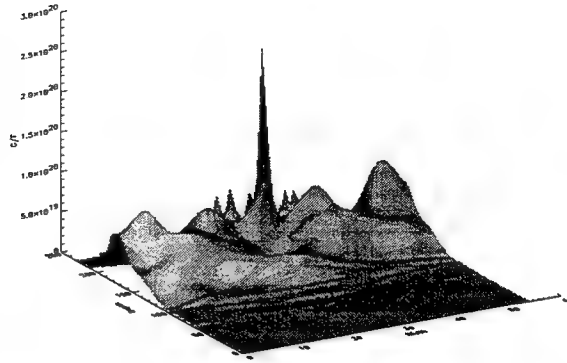
ray-trace model.

#### D. Summary of Results

The FDTD model is more accurate than the ray-trace model for thin solar cells as shown in Figure 3. Given a solar cell design, the FDTD model calculates the total absorption, the maximum achievable current density, and the absorption density. Based on these output parameters, different solar cell designs are simulated and compared using the FDTD model. The FDTD model indirectly calculates the generation rate. The generation rate is the product of the absorption density and the solar spectrum.



(a) Absorption density in the xz-plane

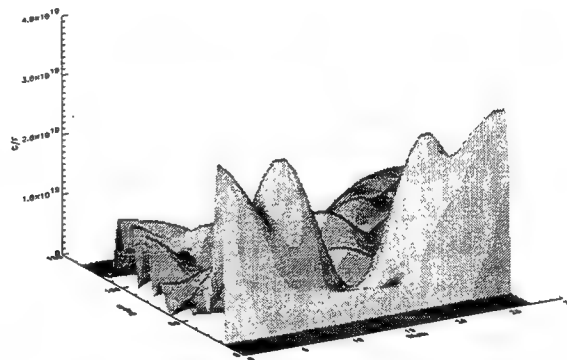


(b) Absorption density in the yz-plane

Fig. 9. The absorption density for the  $0.75 \mu\text{m}$  perpendicular slat solar cell design with  $\lambda = 0.35 \mu\text{m}$ .



(a) Absorption density in the xz-plane



(b) Absorption density in the yz-plane

Fig. 10. The absorption density for the  $0.75 \mu\text{m}$  perpendicular slat solar cell design with  $\lambda = 0.70 \mu\text{m}$ .

The generation rate could be used to calculate the expected current density of a solar cell instead of the maximum achievable current density.

Due to the size and complexity of the FDTD model, only a few select solar cell designs are analyzed based on their light-trapping capacity. The MACD for the  $0.75 \mu\text{m}$  thick pyramid solar cell is  $18.1 \text{ mA/cm}^2$ . The MACD for the  $0.75 \mu\text{m}$  thick perpendicular slat solar cell is  $17.3 \text{ mA/cm}^2$ . The ray-trace model predicts the perpendicular slat solar cell is better at light trapping than the pyramid design. It is surprising to see the FDTD model predict that the  $0.75 \mu\text{m}$  thick, pyramid design is

better. The front pyramid texture increased the MACD by 74% as compared to the planar solar cell. The planar solar cell has a MACD of  $10.4 \text{ mA/cm}^2$ . For thick solar cells, greater than  $50 \mu\text{m}$  thick, the similar increase in MACD is 12%. Texturing becomes more effective at increasing light-trapping as the thickness of the solar cell decreases.

#### IV. DISCUSSION

In this research, two computer models have been developed and used to analyze solar cell light-trapping. The characteristic size of the solar cell determines which model is useful. The ray-trace

model is based on the laws of geometrical optics. For this reason, the ray-trace model is limited to thick solar cells [11]. The ray-trace model is inaccurate when applied to the thin  $0.75\text{ }\mu\text{m}$  thick planar solar cell. The ray-trace model ignores the wave nature of light and interference effects within the solar cell. The Finite-Difference Time-Domain model is based on solving Maxwell's equations directly. The FDTD model accounts for the wave nature of light. The FDTD model accurately predicts the absorption spectrum for the thin,  $0.75\text{ }\mu\text{m}$ , planar solar cell. The FDTD model is applicable to thin solar cells where the characteristic dimension is on the order of the wavelength of light.

The diversity and complexity of possible solar cell designs based on light-trapping creates a large challenge to the engineer. Textured surfaces and anti-reflection films are known to enhance light-trapping. No simple analytical solution to Maxwell's equations exists for the different types of proposed solar cell designs. This problem is relatively easy to overcome by using numerical techniques. Once the numerical model is translated into a computer language, a textured solar cell is as easy to study as a planar solar cell. Neither the ray-trace model nor the FDTD model is limited to planar solar cells. Both models are capable of analyzing the light-trapping characteristics of solar cells with complicated surface textures and anti-reflection films. Both computer models are designed to model complex light-trapping designs. The models also handle dispersive and lossy materials, like silicon.

The solar cells which can be modeled are limited by the available computer resources. The periodic boundary was introduced to partially reduce some of these computer requirements. The ray-trace model was designed to run on an inexpensive personal computer, an Intel-386 based PC with one megabyte of memory. The typical ray-trace analysis of a solar cell requires half a megabyte of memory and about three hours of runtime. However, some runs took as long as a week to analyze a single solar cell. The length of time was dependent on how many rays in the incident beam, the number of textures, and the number of wavelengths. To model dispersion in silicon, a entire run has to be run for each wavelength of incident light. The index of refraction and extinction coefficient are dependent on wavelength. The FDTD model was designed to improve accuracy. One consequence of improved accuracy is the FDTD model cannot run on a personal computer. The biggest limiting factor for the FDTD model is the computer memory re-

quirements. Depending on the wavelength of light, the FDTD analysis of the  $0.75\text{ }\mu\text{m}$  thick solar cell required 770 megabytes at the wavelength of  $0.35\text{ }\mu\text{m}$ . This large memory requirement is due to the large index of refraction (5.442) for silicon. At the highest wavelength of  $2\text{ }\mu\text{m}$ , the memory requirement is only 20 megabytes.

A planar solar cell  $0.75\text{ }\mu\text{m}$  thick has a maximum achievable current density of  $10\text{ mA/cm}^2$ . The MACD is increased by 74% to  $18.1\text{ mA/cm}^2$  by texturing the front surface of the solar cell with pyramids. The perpendicular slat solar cell configuration increased the MACD by only 66%. The absorption density in the thin solar cell is more complicated than the standard exponential decay seen in thick planar solar cells. The absorption density in a textured solar cell can be larger at the back surface than at the front surface. Surface recombination may be most important at the back side of a thin solar cell. Overall, the FDTD model demonstrates texturing has a large effect on light-trapping in thin solar cells.

#### *A. Topics for Future Research*

There are several areas of light-trapping which are of interest to the solar cell community and require further investigation. FDTD analysis was verified for planar solar cells, however, the surprising result of the perpendicular slat solar cell FDTD analysis necessitates that experimental verification be done to confirm the modeling technique for textured surfaces. Future investigation could also include improving the FDTD model to analyzing new light-trapping designs. The ability to accurately model thin solar cells brings new avenues to study and enhance light-trapping.

#### ACKNOWLEDGMENTS

The authors thank Cray Research for supercomputing grants. They also acknowledge the support of Associated Western Universities, Inc. for a Thesis Parts Fellowship. The ray-trace work was supported by the US Department of Energy under contract DOE DE-AC02-83CH10093 and the National Renewable Energy Laboratory under two contracts; CT-2-12285-1 and CAT-4-13527-01.

#### AUTHORS BIO

Todd Marshall received his BS in Engineering Physics (1993) and his MSEE (1996) from the University of Colorado. He is currently working on his PhD in electromagnetics at the University of Colorado - Boulder.

Melinda Piket-May received her BSEE from the University of Illinois - Champaign (1988) and her MSEE (1990) and PhD (1993) from Northwestern University. She is currently an assistant professor at the University of Colorado - Boulder. She received the URSI Young Scientist Award in 1996 and the NSF CAREER Award in 1997.

## REFERENCES

- [1] P. Campbell, S.R. Wenham, and M.A. Green, "Light trapping and reflection control in solar cells using tilted crystallographic surface textures," *Solar Energy Materials and Solar Cells*, vol. 31, no. 2, pp. 133-153, November 1993.
- [2] Bhushan L. Sopor and Todd Marshall, "Optical confinement in thin silicon films: A comprehensive ray optical theory," in *Conference Record of the Twenty Third IEEE Photovoltaic Specialists Conference*, 1993, pp. 127-132.
- [3] T. Tiedje, B. Abeles, J.M. Cebulka, and J. Pelz, "Photoconductivity enhancement by light trapping in rough amorphous silicon," *Applied Physics Letters*, vol. 42, no. 8, pp. 712-714, April 1983.
- [4] Martin A. Green, Andrew W. Blakers, Jianua Zhao, Adele M. Milne, Aihua Wang, and Ximing Dai, "Characterization of 23-percent efficient silicon solar cells," *IEEE Trans. on Electron Devices*, vol. 37, no. 2, pp. 331-336, February 1990.
- [5] Tsuyoshi Uematsu, Minoru Ida, Kunio Hane, Shigeru Kokunai, and Tadashi Saitoh, "A new cell structure for very thin high-efficiency silicon solar cells," *IEEE Trans. on Electron Devices*, vol. 37, no. 2, pp. 344-347, February 1990.
- [6] Patrick Campbell and Martin A. Green, "Light trapping properties of pyramidally textured surfaces," *J. Appl. Phys.*, vol. 62, no. 1, pp. 243-249, July 1987.
- [7] H.W. Deckman, C.R. Wronski, H. Witzke, and E. Yablonovitch, "Optically enhanced amorphous silicon solar cells," *Appl. Phys. Lett.*, vol. 42, no. 11, pp. 968-970, June 1983.
- [8] Eli Yablonovitch and George D. Cody, "Intensity enhancement in textured optical sheets for solar cells," *IEEE Trans. on Electron Devices*, vol. 29, no. 2, pp. 300-305, February 1982.
- [9] B.L. Sopor and R.A. Pryor, "Design of antireflection coatings for textured silicon solar cells," *Solar Cells*, vol. 8, no. 3, pp. 249-261, April 1983.
- [10] M. A. Green, *Chapter 15: Surface Texturing and Patterning in Solar Cells*, pp. 231-269, American Solar Energy Society, 1993.
- [11] T. Marshall and M. Piket-May, "Numerical model of light-trapping in solar cells," *Applied Computational Electromagnetics Society Journal*, Submitted January 1997.
- [12] K.S. Yee, "Numerical solution of initial boundary value problems involving maxwell's equations in isotropic media," *IEEE Trans. on Antennas and Propagat.*, vol. 14, pp. 302-307, 1966.
- [13] Allen Taflov, *Computational Electrodynamics the Finite-Difference Time-Domain Method*, pp. 98-100, 111-134, 281-295, Artech House, Boston, 1995.
- [14] A. Taflov and M.E. Brodwin, "Numerical solution of steady-state electromagnetic scattering problems using the time-dependent maxwell's equations," *IEEE Trans. on Microwave Theory Tech.*, vol. 23, pp. 623-630, 1975.
- [15] F.L. Pedrotti and L.S. Pedrotti, *Introduction to Optics*, pp. 42, 466, 485-487, Prentice-Hall, Englewood Cliffs, New Jersey, 1987.
- [16] E.D. Palik, Ed., *Handbook of Optical Constants of Solids*, p. 547, Academic Press, 1985.
- [17] A. Bayliss and E. Turkel, "Radiation boundary conditions for wave-like equations," *Comm. Pure Appl. Math.*, vol. 23, pp. 707-725, 1980.
- [18] B. Engquist and A. Majda, "Absorbing boundary conditions for the numerical simulation of waves," *Mathematics of Computation*, vol. 31, pp. 629-651, 1977.
- [19] L.N. Trefethen and L. Halpern, "Well-posedness of one-way wave equations and absorbing boundary conditions," *Mathematics of Computation*, vol. 47, pp. 421-435, 1986.
- [20] G. Mur, "Absorbing boundary conditions for the finite-difference approximation of the time-domain electromagnetic field equations," *IEEE Trans. on Electromagnetic Compatibility*, vol. 23, pp. 377-382, 1981.
- [21] R.L. Higdon, "Numerical absorbing boundary conditions for the wave equation," *Mathematics of Computation*, vol. 49, pp. 65-90, 1987.
- [22] K.K. Mei and J. Fang, "Superabsorption-a method to improve absorbing boundary conditions," *IEEE Trans. on Antennas and Propagat.*, vol. 40, pp. 1001-1010, 1992.
- [23] J.P. Berenger, "A perfectly matched layer for the absorption of electromagnetic waves," *Journal of Computational Physics*, vol. 114, pp. 185-200, 1994.
- [24] D.S. Katz, E.T. Thiele, and A. Taflov, "Validation and extension to three dimensions of the berenger pml absorbing boundary condition for fd-td meshes," *IEEE Microwave and Guided Wave Letters*, vol. 4, pp. 268-270, 1994.
- [25] E. Yablonovitch, G.B. Stringfellow, and J.E. Greene, "Growth of photovoltaic semiconductors," *Journal of Electronic Materials*, vol. 22, no. 1, pp. 49-55, 1993.

# MODELLING EDDY CURRENTS IN UNBOUNDED STRUCTURES USING THE IMPEDANCE METHOD

Daniel James, David V. Thiel  
Radio Science Laboratory, School of Microelectronic Engineering,  
Griffith University, (Brisbane), Qld, Australia 4111.

## Abstract

In this paper extensions to the impedance network method are presented. In particular the method has been applied to problems with boundaries extending to infinity. The infinite boundary condition can also be applied to lines of symmetry in the given geometry. Two dimensional surface models have been verified by comparison of numerical and experimental results in which the potential was measured along the edge of copper sheeting of various shapes located in a uniform, quasi-static magnetic field. The method has potential for modelling three dimensional structures including anisotropic earth planes, arbitrarily shaped buried objects, and both finite and infinitely long faults, dykes, pipes, cylinders and cracks.

## I. Introduction

The three dimensional impedance method has been used to model eddy currents induced in heterogeneous human models by a time varying quasi-static magnetic field [1-4]. In this work, the object was modelled by a uniform cubic three dimensional mesh of impedance cells. The values of the impedances were determined from the size of the element and the conductivity of the material being modelled. Using standard circuit analysis the current was solved for each face of every cell.

Other recent approaches to the calculation of eddy currents using numerical techniques include an integral formulation using a set of R, L and C elements [5], the boundary element formulation [6], finite element modelling [7], edge element [8], the integral equation approach [9] and many others. There are considerable difficulties in modelling the eddy currents induced in conductive media when both the source field is non-uniform and the media is both inhomogeneous and has arbitrary shape or is of infinite extent in one or more directions. In this paper the impedance method [1] is extended to address these limitations. By discretising the two dimensional area or three dimensional volume in terms of a spatial array of impedance elements various structures can be represented. The individual parameters of each element and spatial variations in the applied field can also be modelled. Varying symmetries in the solution space together with prudent application of boundary conditions reduces the number of elements required to solve a given problem. The resultant matrix generated from this technique is used to solve for the current in each cell for a spatially varying time harmonic magnetic field. The technique is applied to

the solution of eddy current problems in materials with a spatial variation in conductivity in the presence of a quasi-static magnetic field.

Until now calculations using this method have only dealt with finite sized bodies with air boundaries. This excludes the possibility of modelling a large range of problems where boundaries extend to infinity. For this reason an infinite boundary condition is desirable.

## II. Impedance method theory

Maxwell's Equation in differential form (1) describes the electric field  $\vec{E}$  generated by the presence of a time varying magnetic field  $\vec{B}$ .

$$\nabla \times \vec{E} = - \frac{\partial \vec{B}}{\partial t} \quad (1)$$

With a surface area  $S$  enclosed by the boundary path  $C$ , one can apply Stoke's Theorem to equation (1) and obtain

$$\oint_C \vec{E} \cdot d\vec{l} = - \int_S \frac{\partial \vec{B}}{\partial t} \cdot d\vec{s} \quad (2)$$

For the quasi-static case the left hand side of equation (2) represents the induced potential in the loop  $V$ , ie.

$$V = \oint_C \vec{E} \cdot d\vec{l} \quad (3)$$

and the right hand side of equation (2) is the negative of the time derivative of flux  $\Phi$  crossing the surface ( $S$ ), where

$$\Phi = \int_S \vec{B} \cdot d\vec{s} \quad (4)$$

For the time harmonic case we have the relation

$$-\frac{\partial \Phi}{\partial t} = \oint_C \vec{E} \cdot d\vec{l} = -j\omega\Phi \quad (5)$$

where  $\omega$  is the angular frequency of the magnetic field.

By dividing the media into a rectangular mesh of discrete impedance elements  $Z$ , we can apply Stoke's theorem to each cell individually providing that each cell is sufficiently small so that the applied magnetic field is uniform within its boundary. The value of the impedance on each side of the cell is directly related to the length of the side and the complex dielectric constant of the cell. The magnitude of the inducing magnetic flux is directly related to the area enclosed by the cell and the angle between the  $\vec{S}$  and  $\vec{B}$ . For a two dimensional surface

formulation the values of  $Z$  are expressed in terms of the cell length  $L$ , an arbitrary impedance element transverse thickness  $A$  (usually expressed as an area in the three dimensional model although it is the thickness in the two dimensional formulation) by the following relation [3].

$$Z = \frac{L}{(\sigma + j\omega\epsilon_r\epsilon_0) \cdot A} \quad (6)$$

where  $\sigma$  is the conductivity and  $\epsilon_r$  is the relative permittivity of the material and  $\epsilon_0$  is the dielectric constant of free space.

For a good conductor ( $\sigma \gg \omega\epsilon_r\epsilon_0$ ) and using a quasi-static assumption, equation (6) becomes

$$R = \frac{L}{\sigma A} \quad (7)$$

We restrict the formulation to non-magnetic materials in time harmonic fields. A single rectangular cell is shown in Fig. 1(a), together with the electrical analog (b).

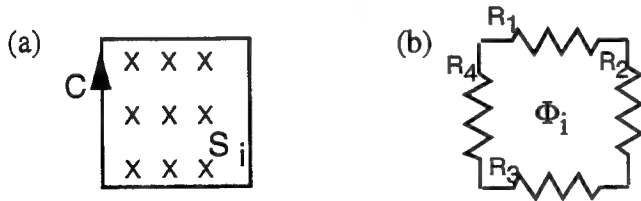


Figure 1: An arbitrarily enclosed region of space and its discretized equivalent cell.

In terms of the discretization process, it is assumed that the magnetic field  $B_i$  across the element is uniform and so the flux  $\Phi_i$  within each cell is directly related to the area of the cell  $S_i$ . For an arbitrary four sided cell, we can write

$$j\omega\Phi_i = \sum_{j=1}^4 V_{Rj} \quad (8)$$

where  $V_{Rj}$  is the voltage across the  $j^{\text{th}}$  resistor in the boundary path surrounding the  $i^{\text{th}}$  cell.

From (8) using Ohm's Law we can solve for the current in a single loop  $I_{Cj}$ . The relation then becomes

$$j\omega\Phi_i = \sum_{j=1}^4 I_{Cj} R_j ; \quad (9)$$

where  $I_{Cj}$  = cell  $j$  loop current.

The full model consists of many interconnected cell loops in a mesh. A two dimensional representation is shown in Fig. 2

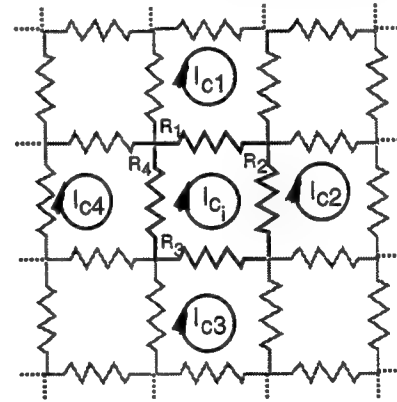


Figure 2: A portion of the two dimensional resistive element mesh.

Hence the relationship between a one cell  $I_{Cj}$  and its nearest neighbour cell currents  $I_{Cj}$  is

$$j\omega\Phi_{Cj} = \sum_{j=1}^4 (I_{Cj} - I_{Cj}) \cdot R_j \quad (10)$$

For a conductive sheet consisting of  $n$  cells, the system can be represented as

$$[R]_{n \times n} \cdot [I]_{1 \times n} = j\omega[\Phi]_{1 \times n} \quad (11)$$

where  $R_{ij}$  forms the resistance network,  $I$  is a column matrix of unknown currents and  $\Phi$  is a row matrix of magnetic flux through each element.

From (11) it is possible to calculate the loop current in each cell and from this, calculate the net current distribution throughout the solution space. Thus, we can determine the net current through each resistive element  $R$  by summing the contributing currents from adjoining cells. For the two dimensional surface formulation there are a maximum of two component currents per resistive element, however for a three dimensional model there are potentially four component currents flowing through a resistive element. For example, if the resistive element lies in the  $x$  direction then there are two loop currents in the XOY plane and two in the XOZ plane [4].

Note that the applied field flux  $[\Phi]$  can be spatially variable for each element and so non-uniform fields can be modelled. The flux generated by induced currents in a particular cell will be in the opposite direction to the applied flux and extends radially from the cell. If we consider the four immediately adjacent cells then to a first approximation we would expect less than 25% of this flux will flow through each adjacent cell. Since the field falls away as  $r^{-3}$  contributions to other cells will be even less significant. Therefore re-radiated flux generated from the induced eddy currents is not considered in this method. This assumption is also used by others [1-4].

The two dimensional surface formulation is sufficient to solve many problems and the method is easily adaptable to three dimensions and has been demonstrated in the literature [1]. The computation of  $\Phi$  as it appears in equation (11) is still from the magnetic flux through each cell which must be calculated from the magnetic field component normal to the surface area of each cellface.

### Boundary conditions

A variety of boundary conditions are required for the accurate solution of models of arbitrary shape or semi-infinite size. Application of the appropriate boundary conditions can reduce the number of cells required to solve a given problem and hence increase the computational efficiency. This allows larger problems to be solved on a given platform. A number of boundary conditions are discussed below.

#### (i) Open boundary/insulator boundary

In the case of an open boundary where a conductor meets an insulator, cells lying on the edge do not allow current to flow beyond the boundary, i.e. there are no sources/sinks of current beyond the boundary. Hence for an open boundary the contributing current  $I_c$  in equation (8) is zero. Thus any element at this boundary is expressed in terms of its four bounding resistances and up to three nearest neighbouring current elements.

#### (ii) Infinite boundary

Where a uniform material extends to infinity and is subjected to a uniform magnetic field it can be classified as an infinite boundary. At infinity, adjoining cells in the direction of the boundary will have identical currents. If the infinite boundary is located at  $x = \infty$ , then it follows

that  $\frac{dI}{dx} = 0$  and the net current flowing through the element on the boundary of these two cells will be zero (the summation of two equal and opposite component currents). This is a Neumann boundary condition. Equation (10) then becomes a summation of potentials  $j = 1..3$ . The location of the infinite boundary is chosen such that in the solution, the difference in current between cells adjacent to the boundary is less than (say) 5%.

With 3 or more infinite boundaries the cell currents are no longer constrained. This is reflected by an ill conditioned matrix  $[R]$  where no unique solution exists because the number of unknown quantities exceeds the number of knowns and the matrix equation cannot be solved.

#### (iii) Symmetry

Along a line (eg. parallel to the  $Y$  axis) or plane of symmetry (eg. in the YOZ-plane) then  $\frac{dI}{dx} = 0$ . This is also a Neumann boundary condition, identical to the infinite boundary condition.

### Computational aspects

The computational model was developed and implemented on a Sun Sparc Server 10. Mesh generation and processing was implemented using custom software in 'C' with double precision variables. For a two dimensional surface formulation, mesh generation yields an  $n \times n$  matrix for an  $n$  element problem. The matrix generated has a sparse diagonally dominant band structure. Because the problems exhibit a low condition number an exact rather than an iterative inversion routine was implemented. Standard LU decomposition as described in [10] was used. Matlab™ was used to create the net current vectors and voltage plots from the numerically obtained values of cell loop currents  $[I]$  in equation (11).

#### Non-rectangular cells

Equation (9) can be modified to calculate the induced current in one cell in terms of any number of nearest neighbour cells. It follows from this equation that the number of sides  $n$ , of a given cell determines the exact form of this equation ( $j=1..n$ ). Triangular elements allow more accurate representation of many structures where normally highly detailed staircase approximations are required.



### III The numerical results

To verify the method in two dimensions, a uniform, square, conductive sheet of dimensions 9cm x 9cm was modelled in a uniform quasi-static magnetic field. The numerical model was evaluated for many cell sizes. The voltages between points on one edge of the sheet were evaluated. This is equivalent to the spaced pickup experiment (described below). Note that a cell with dimensions of 3cm x 3cm allows the solution of only two data points whereas a cell size of 0.25cm x 0.25cm produces 18 data points. These results are shown in Fig. 3. It should be noted that there is good agreement between the numerical results obtained for all cell sizes although the spatial resolution is obviously limited by the cell size. The error for even the largest cell size is less than 5%.

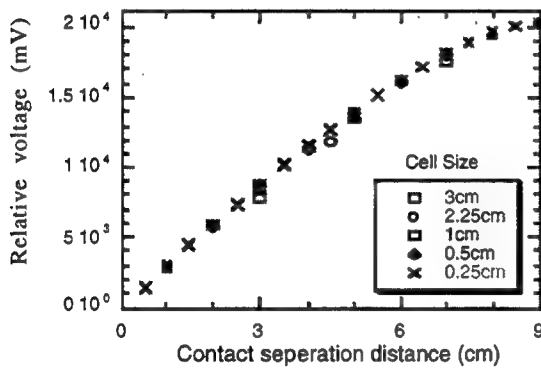


Figure 3: Model accuracy for a variety of cell sizes ( $f=1\text{kHz}$ ,  $\sigma = 5.8 \times 10^7 \text{S/m}$ ).

To model an infinitely long strip about a small region of interest infinite boundary conditions are used. The conductor/air interface is an open boundary since the currents are confined to the conductor with little current injection to/from the air. Fig. 4 shows an 18 x 18 cell model of 1cm x 1cm cells with  $R = 1/\text{unit}$  with two open and two infinite boundary conditions applied.

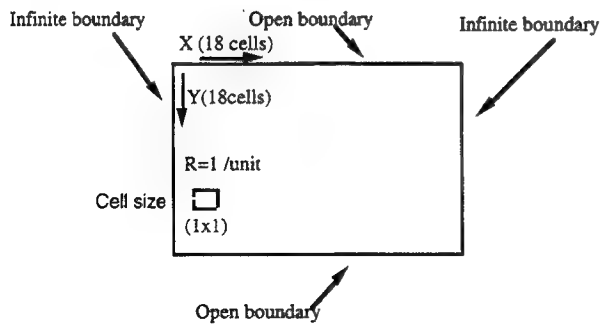


Figure 4: Model of an infinitely long conductive strip.

### IV Experimental setup

Experimental measurements were made to provide a direct comparison with results from the numerical model. A split shielded loop of diameter 50cm was placed around the test area (Fig. 5). The loop was driven with a signal generator at 1kHz to create a uniform magnetic field normal to and inside the loop. A typical field strength of 5μT was generated. Using a small search coil, the magnetic field inside the area bounded by the coil was found to be constant to within less than 5%. Copper foil of various shapes were placed in this region normal to the magnetic field.

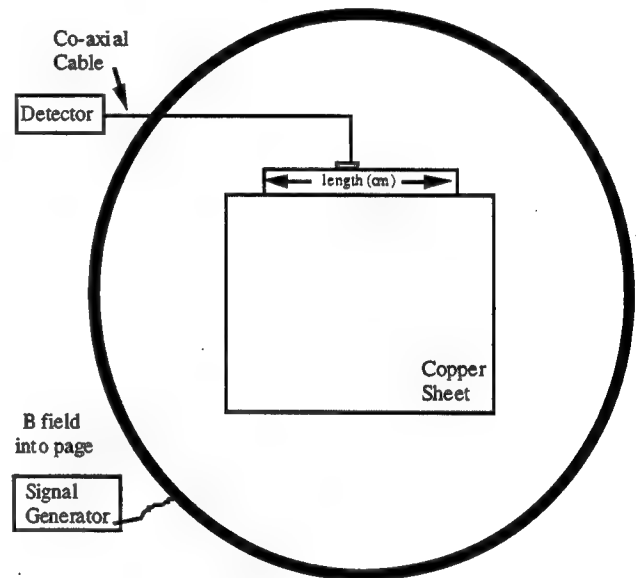


Figure 5: Experimental setup.

Voltage probes with electrical connections to the edge of the foil were connected to a detector using co-axial cable. The detector circuit had an input impedance of  $10^{12}\Omega$ . This was created by using commercially available JFET operational amplifiers in an instrumentation amplifier configuration. Detector electronics was housed in a small aluminium box (5cm x 7cm x 10cm) which was battery powered with a LCD display. There was no earth reference to the detector. The electronics consisted of a band pass filter tuned to 1kHz, amplifier stages, an RMS to DC detector and DMM (digital multimeter) module. The instrument was calibrated by varying the field strength stepwise and recording the probe output.

The objective in this design was to minimise any electric field generation from the coil and magnetic or electric field



induction in the detector electronics. When the earth connection to the shield of the excitation coil was removed, the signal level of a test coil placed within the test area showed poor directionality indicating electric field coupling. With the earth connection in place, the detector output was zero when the wire test coil was oriented parallel to the magnetic field.

## V Results

In the first experiment a square sheet of copper foil (9cm x 9cm) was placed in the quasi-static magnetic field such that the field is normal to the copper sheet. This problem was solved numerically using a variety of cell sizes. With 18 x 18 cells the numerical solution for the quasi-static vector current distribution is displayed in Fig. 6. This current distribution shows a well known result where the induced current is circular and the greatest current magnitudes lie on the edge of the sheet. This was verified by experiment by monitoring the voltage drop across a spaced pickup at various points on the edge of the sheet. This current plot gives good agreement with a result generated using edge analysis [8].

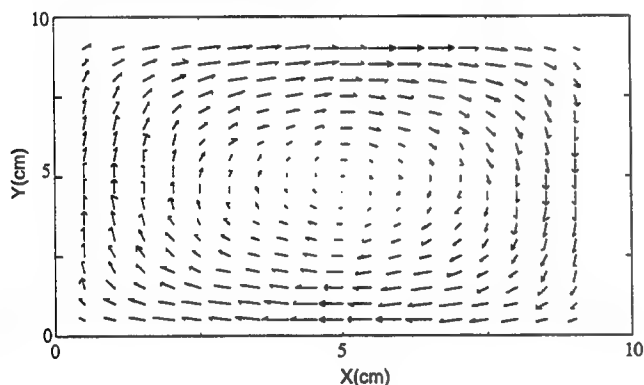


Figure 6: Induced current distribution in a homogenous conductive square (9cm x 9cm) cell size (0.5cm x 0.5cm) calculated using the impedance method.

### Spaced pickup

In this set of measurements, separation between the measurement points was varied across the top of the sheet while remaining symmetrical about the position  $x = 4.5$ cm. The numerical model results are normalised to the experimental magnetic field strength by using a field strength probe. The model used had a cell size of 0.25cm. The model results were obtained by numerically integrating the currents between the ends of the pickup to obtain a measured potential. These results are displayed in Fig. 7. The difference between the model results and the experimentally measured data is less than 10%

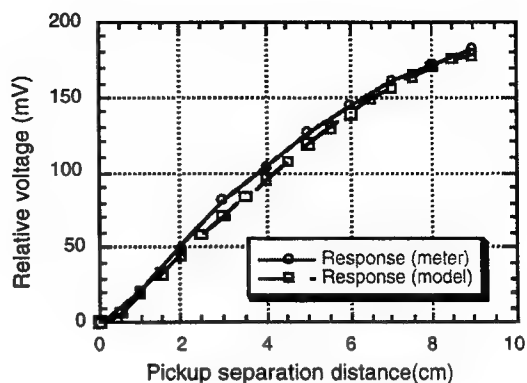


Figure 7: Comparison between impedance method model results and experimental results for a spaced pickup.

### Length variations

In this experiment a rectangular (20cm x 9cm) sheet of copper foil was placed in a quasi-static magnetic field such that the field is normal to the surface of the copper sheet. The length of the sheet was progressively shortened from 20cm to 9cm in 0.5cm increments. The voltage difference was always measured between two corner points on one 9cm edge. The numerical model used had a cell size of 0.5cm x 0.5cm. Fig. 8 shows that the normalised response of the model compares well with the experimentally measured results. Clearly as the size of the sheet decreases, the response also decreases. There is however, a limiting sheet length (approximately 9cm) beyond which there is no significant increase in response.

It is clear that beyond a length of 9cm there is very little contribution to the measured voltage from additional copper material; ie. for short lengths the current is constrained by the y dimension and beyond the square, the current is constrained by the x direction.

### Cell shape variability

Two shapes were modelled experimentally and numerically. First the response from a symmetrical detector with a separation distance of 9cm across the top of a 9cm x 9cm square sheet of copper foil was measured. The foil was then cut from a top corner across the diagonal to a lower corner to form a triangular shape. The detector position remained unchanged. The response from this triangular shape was then measured. The two shapes were modelled using a square and triangular one element model respectively. The induced voltage of the triangular shape reduces to 66% of the square shape in both the numerical and experimental results. The measured and numerically modelled results were found to differ by 0.5%

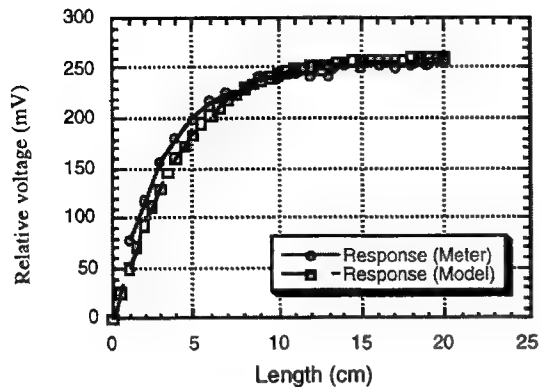


Figure 8: Model and experiment results for copper rectangle length variations.

#### Infinitely long homogenous conductive strip

In Fig. 4 the region of interest is divided into  $18 \times 18$  cells. Cells on the top and bottom of this model are open boundaries and the cells on the left and right boundaries are infinite boundaries. Fig. 9 shows the vector currents obtained by the impedance method. Note that the boundary elements are included in columns 1 and 18 of the figure. The current through the model is parallel to the open boundary edges indicating that the infinite boundary condition is effective.

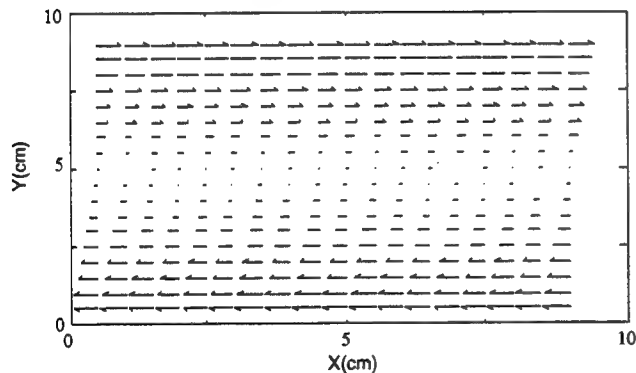


Figure 9: Induced currents in an infinitely long conductive strip.

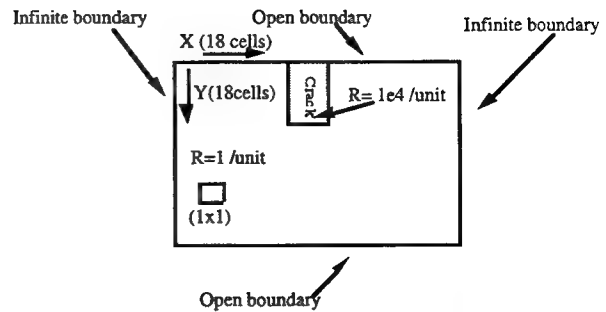


Figure 10: A model of a surface crack in an infinitely long conductive strip.

#### Surface crack modelling

Fig. 10 shows a resistive crack ( $1 \times 5$  cells,  $R = 1 \times 10^4$ ) in an infinitely long homogenous strip ( $R=1$ ). The impedance method results are shown in Fig. 11. The induced currents flow around the resistive crack as expected.

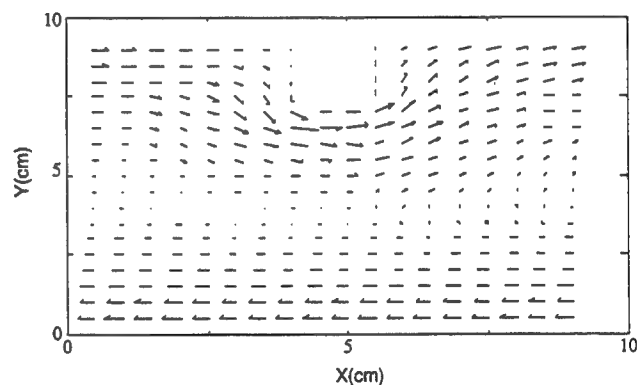


Figure 11: Induced currents around a crack in an infinitely long conductive strip.

#### Three dimensional modelling

The impedance method can be used to model three dimensional bodies in the presence of an applied magnetic field [3]. Computation time for a three dimensional model is dramatically increased (cubic rather than squared relationship) for given cell dimensions.

The two dimensional surface formulation is adequate for the two dimensional cross section modelling of three dimensional structures on three conditions:

(a) The magnetic flux  $[\Phi]$  is unaffected by the nearest adjacent plane perpendicular to the direction of the applied field. (There is no significant magnetic field attenuation if the distance is less than 10% of one skin depth).

(b) The conductivity distribution in the adjacent plane is not significantly different to that of the plane being

modelled. (There will be negligible cross planar currents generated which give rise to additional out of plane current sources and sinks.)

(c) The magnetic field is always directed parallel to the surface vector of each cell. (If this is not the case then additional current sources and sinks will be present within the model.)

## VI Conclusions

The impedance method can be used to solve eddy current problems in both bounded and unbounded regions. This formulation has the advantage of using a variety of cell shapes (for example triangular and rectangular) to best represent the structure in the model. In addition, there is no requirement for a uniform mesh. Different sizes and shapes can be used within the one model. The impedance method has been verified using copper sheet in a uniform magnetic field. The experimental measurements lie within 10% of the numerical model results for most measurements.

By applying appropriate boundary conditions, small regions of interest within large structures can be modelled. This enables large structures to be modelled with only a small number of elements if the region of interest is small. This technique allows for significant CPU savings and hence greater resolution.

Three dimensional modelling has great potential to model complex features. If the features of interest lie only in the plane orthogonal to the applied field then a two dimensional model is sufficient since there will be no interaction between the layers. The method has potential for the non-destructive detection of sub-surface flaws in metallic regions eg. aircraft wings and generator housings.

## References

- [1] O.P. Gandhi, J.F. DeFord and H. Kanai, "Impedance method for calculation of power deposition patterns in magnetically induced hyperthermia", *IEEE Trans. Biomed. Eng.*, vol. BME-31, no. 10, pp. 644-651, 1984.
- [2] J. F. DeFord and O.P. Gandhi, "An impedance method to calculate currents induced in biological bodies exposed to quasi-static electromagnetic fields", *IEEE Trans. Electromagn. Compat.*, vol. EMC-27, no. 3, pp. 168-173, 1985.
- [3] N. Orcutt and O.P. Gandhi, "A 3-D impedance method to calculate power deposition in biological bodies subjected to time varying magnetic fields", *IEEE Trans. Biomed. Eng.*, vol. BME-35, pp. 577-583, 1988.
- [4] W. Xi and M.A. Stuchly, "Induced electric currents in models of man and rodents from 60Hz magnetic fields", *IEEE Trans. Biomed. Eng.*, vol. BME-41, no. 11, pp. 1018-1023, 1994.
- [5] M. Gimignami, A. Musolino and M. Raugi, "Integral formulation for nonlinear magnetostatic and eddy currents analysis", *IEEE Trans. Mag.*, vol. MAG-30, pp. 3024-3027, 1994.
- [6] I.D. Mayergoyz, "Boundary integral equations of minimum order for the calculation of three dimensional eddy current problems", *IEEE Trans. Mag.*, vol. MAG-18, no. 2, pp. 536-539, 1982.
- [7] A. Konrad, M.V.K. Chari and Z.J. Csendes, "New finite element techniques for skin depth problems", *IEEE Trans. Mag.*, vol. MAG-18, no. 2, pp. 450-455, 1982.
- [8] H.Tsuboi, F. Kobayashi and T.Misaki, "Computation of electric current distribution on thin conducting plate using edge element", *IEEE Trans. Mag.*, vol MAG-32, no. 3, pp. 745-748, 1996.
- [9] L. Turner, "An integral equation approach to eddy-current calculations", *IEEE Trans. Mag.*, vol MAG-13, no. 5, pp. 1119-1121, 1977.
- [10] W. Press, *Numerical recipes in C : The art of scientific computing*, 2nd ed., Cambridge University Press, 1992.

# VERIFICATION OF SOFTWARES FOR ELECTROMAGNETIC FIELD ANALYSIS USING MODELS PROPOSED BY INVESTIGATION COMMITTEES IN IEE OF JAPAN

Norio Takahashi

Department of Electrical and Electronic Engineering, Okayama University  
3-1-1 Tsushima, Okayama 700, Japan

**Abstract:** *In order to investigate methods for analyzing electromagnetic fields and to compare the accuracy and the CPU time of various codes and so on, investigation committees were set up in IEE of Japan. In this paper, the activities of various investigation committees relating electromagnetic field analysis are described from the viewpoint of the verification of software.*

## 1. INTRODUCTION

In the Institute of Electrical Engineers (IEE) of Japan, twelve investigation committees for analyzing electromagnetic fields have been established from 1977 as shown in Table 1. These committees are composed of 20-30 members from universities, institutes and industries. The committee has a meeting every month or

every two months and surveys the following subjects, for example:

- (1) recently developed methods for calculating electromagnetic fields,
- (2) validity of newly developed methods,
- (3) new application areas of numerical analysis of electromagnetic fields.

Some committees have proposed models in order to verify various numerical methods. Each committee published an IEEJ Technical Report.

In this paper, verification models proposed by the committees of IEE of Japan and some results reported by committee members are shown. Results of calculation of magnetic fields, eddy currents, forces, torques, optimized shapes and measurement carried out by the author are also

Table 1 Investigation committees in IEE of Japan

no.	period *	name	number of members		
			univ.	inst.	indust.
1	1977 - 1980	Investigation Committee on Electromagnetic Field Analysis of Electric Power Machines Using Finite Element Method	8	1	10
2	1980 - 1984	Investigation Committee on Applications of Numerical Method for Analyzing Electric Power Machines	11	2	12
3	1984 - 1987	Investigation Committee on 3-D Calculation of Electromagnetic Fields	12	2	10
4	1987 - 1990	Investigation Committee on Numerical Analysis of Eddy Current	10	1	14
5		Investigation Committee on Applications of Numerical Method for Analyzing Magnetic Fields in Rotating Machines	14	0	12
6	1990 - 1993	Investigation Committee on Techniques for Applications of 3-D Electromagnetic Field Analysis	12	1	17
7		Investigation Committee on Software for Numerical Analysis of Magnetic Fields in Rotating Machines	10	0	14
8	1993 - 1995	Investigation Committee on Highly Accurate Simulation Technique for Rotating Machines	8	0	17
9	1993 - 1996	Investigation Committee on Electromagnetic Field Analysis and Its Applications to Optimization Problems	11	3	14
10	1995 - 1997	Investigation Committee on Techniques for Applications of Electromagnetic Field Analysis for Rotating Machines	10	0	16
11	1996 - 1999	Investigation Committee on Highly Advanced Optimization Technique for Electromagnetic Problems	13	2	16
12	1997 - 1999	Investigation Committee on Techniques of Electromagnetic Field Analysis for Virtual Engineering of Rotating Machines	8	0	17

\* : The committees start in April and end in March.

discussed.

## 2. MAGNETOSTATIC AND EDDY CURRENT MODELS (1984-1990)

### A. 1984-1987

The "Investigation Committee on 3-D Calculation of Electromagnetic Fields" (1984-1987, Chairman: T. Nakata, Okayama Univ.) proposed a simple 3-D magnetostatic model[1] as shown in Fig.1, so that many universities, institutes and industries can join the project. The rectangular open core is surrounded by a d.c. exciting winding with 457 turns. The d.c. current is equal to 6.56A. A magnetic shield box of which the thickness  $t$  is 1.6mm covers the model. The relative permeabilities of the core and the shield are assumed to be 1000.

Fig.2 shows the calculated flux distribution. Fig.3 shows the absolute value of flux density above the core ( $z=110\text{mm}$ ). Fig.4 shows the effects of the thickness  $t$  and the relative permeability  $\mu_s$  of the shield box on the flux density at the point of  $x=y=0$ ,  $z=110\text{mm}$ . When  $t$  is increased, the flux density is not changed with  $t$ . The change of flux density by the thickness  $t$  is small when  $\mu_s$  is increased. The effect of the gauge condition of the  $A$ -method on the obtained result is discussed[3]. The cancellation error of the T-W method[4] and the error of the boundary element method[5] are discussed.

## B. 1987-1990

The "Investigation Committee on Numerical analysis of Eddy Current" (1987-1990, Chairman: T. Onuki, Waseda Univ.) proposed a 3-D eddy current model[6] as

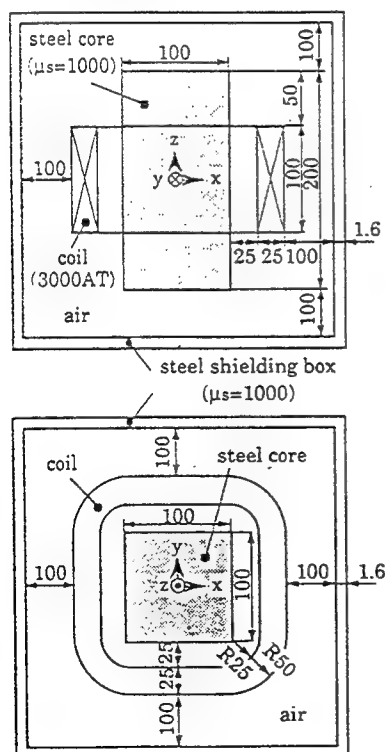


Fig.1 3-D Magnetostatic model.

shown in Fig.5. A rectangular ferrite core is surrounded by an exciting coil. An ac current of which the effective value is 1000AT at the frequency of 50Hz is applied. Two aluminum plates are set on the upper and lower sides of the core. The conductivity of the aluminum is equal to  $3.215 \times 10^7$  S/m, and the relative permeability ( $\mu_r$ ) of the core is assumed to be 3000. Both cases with and without a hole in the plate are investigated.

Magnetic field noise is induced at the junction of the Hall sensor and lead wires, and this noise cannot be easily eliminated by simply twisting the lead wires. Therefore, the flux density is measured using a small search coil

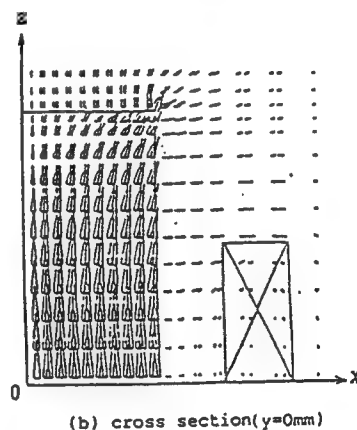
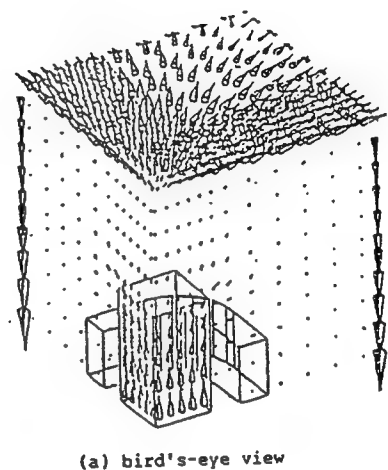


Fig.2 Flux distribution.

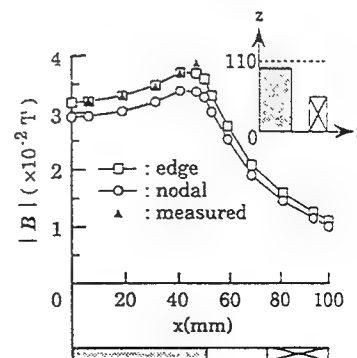


Fig.3 Spatial distribution of flux density (with shield,  $y=47\text{mm}$ ,  $z=110\text{mm}$ ).

Fig.6 shows the distributions of flux density vectors. Fig.7 shows the maximum absolute value  $|\mathbf{B}|$  of the flux

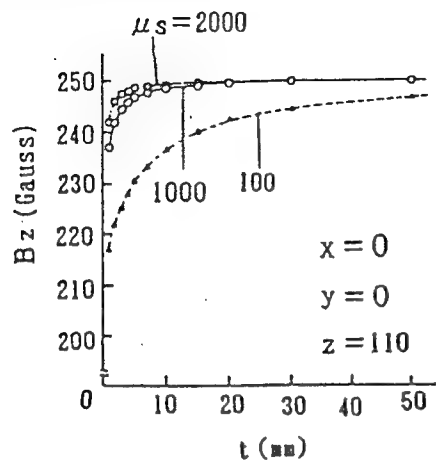


Fig.4 Effect of thickness  $t$  on flux density.

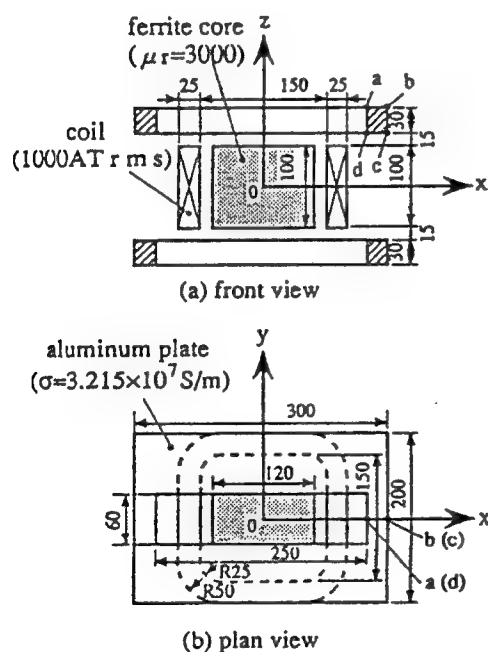


Fig.5 3-D eddy current model.

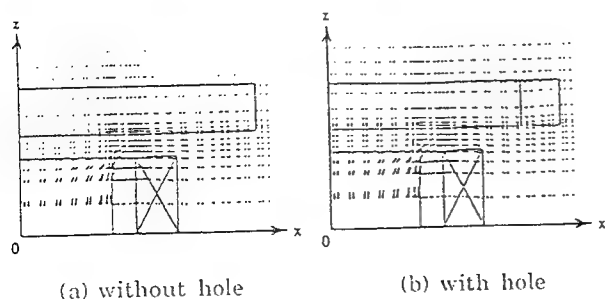


Fig.6 Distributions of flux density vectors  
( $y=0\text{mm}$ ,  $\omega t=0^\circ$ ).

density along the line at  $z=57.5\text{mm}$ [7]. The discrepancies between the calculated and measured values are quite small. Fig.8 shows the distributions of eddy current density vectors. Fig.9 shows the x- and y-components of the maximum value of the eddy current density on the surface ( $z=65\text{mm}$ ) of the aluminum plate. The results calculated using various methods and elements are almost the same. The discrepancies between the calculated and

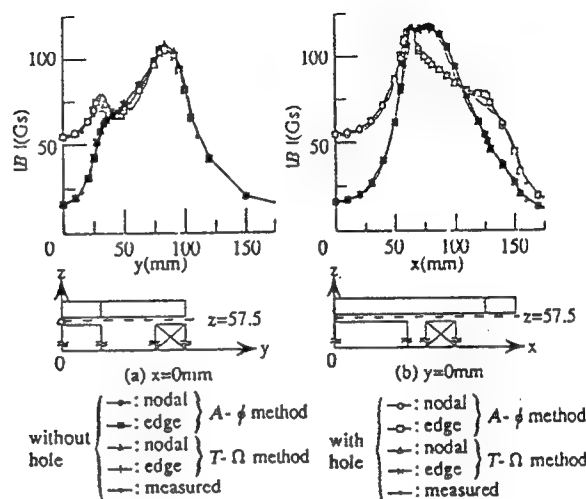
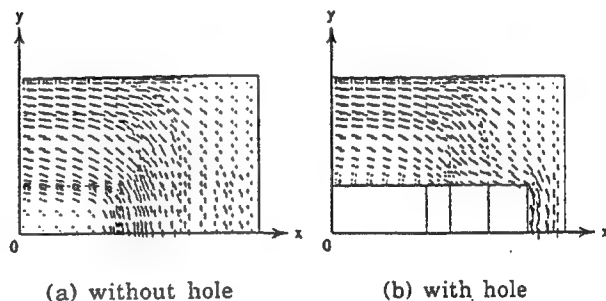


Fig.7 Distributions of flux density ( $z=57.5\text{mm}$ ).



**Fig.8** Distributions of eddy current density vectors ( $z=65\text{mm}$ ,  $\omega t=0^\circ$ ).

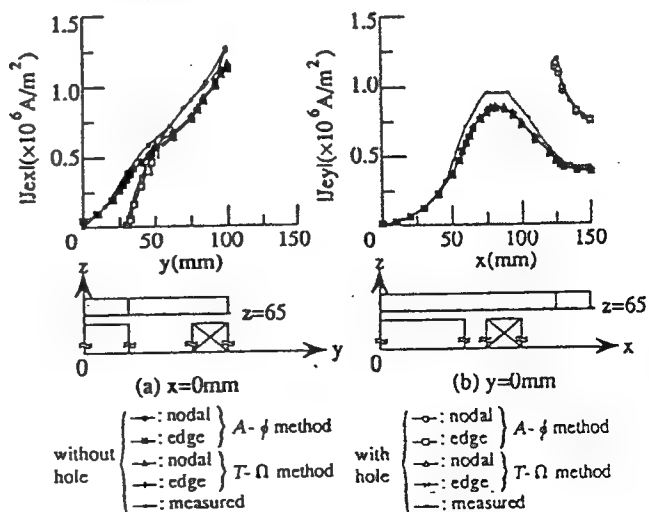


Fig.9 Distribution of eddy current density ( $z=65\text{mm}$ ).

measured values may be due to an insufficient number of elements, setting error of sensor, etc. Table 2 shows the comparison of calculated and measured values of total eddy current  $I_e$  passing through the cross section a-b-c-d-a in Fig.5. The error  $\varepsilon$  is defined by

$$\varepsilon = \left| \frac{I_e(\text{cal}) - I_e(\text{mea})}{I_e(\text{mea})} \right| \times 100\% \quad (1)$$

where  $I_e(\text{cal})$  is the current calculated and  $I_e(\text{mea})$  is the current measured.

The number of iterations of ICCG (Incomplete Cholesky Conjugate Gradient) method for calculating large simultaneous equations, the CPU time, etc. are shown in Table 3. The CPU time of the  $T-\Omega$  method in the analysis of the model without hole decreases considerably compared with the  $A-\phi$  method. The CPU times of the edge element for the  $A-\phi$  and  $T-\Omega$  methods are about 1/6 and 1/2 of the nodal element. Although the CPU time of the  $T-\Omega$  method in the analysis of the model with hole is much larger compared with that without hole in the case of nodal element, it is not so remarkable in the case of edge element. From the viewpoints of the CPU time, the  $T-\Omega$  method with edge element is favorable.

A new formulation of the  $A-\phi$  method[8], a hybrid FE-BE method[9], the boundary element method using edge elements[10] and the finite element method with integral equation[11] are discussed.

### 3. MODELS FOR CALCULATING FORCE AND TORQUE (1990-1995)

#### A. 1990-1993

The "Investigation Committee on Software for Numerical Analysis of Magnetic Fields in Rotating Machines" (1990-1993, Chairman: T. Nakata, Okayama Univ.) proposed four kinds of models which are related to magnetic field analysis of rotating machines[12].

Fig.10 shows a 3-D model for the verification of dc force calculation[13,14]. The center pole and yoke are made of steel. The coil has 381 turns and the ampere-turns (dc) are chosen to be 1000, 3000, 4500 and 5000 in order to investigate the saturation effect. Fig.11 shows the z-component  $F_z$  of electromagnetic force calculated using the Maxwell stress tensor method, advanced energy method and magnetizing current method. The number of elements,  $n_e$ , is equal to 108864. The force calculated by the Maxwell stress tensor method using the edge element with  $A$  (magnetic vector potential) variable is the nearest to the measured value. The rate of increase of the force with current is reduced above 3000AT due to the saturation of the center pole.

Fig.12 shows the effect of number of elements,  $n_e$ , on the results calculated. Fig.13 shows the initial mesh ( $n_e=4032$ ). Each side of individual elements is subdivided into twice ( $n_e=4032 \times 2^3=32256$ ) and thrice ( $n_e=4032 \times 3^3=108864$ ). The figure suggests that the force calculated by the Maxwell stress tensor method

Table 2 Comparison of eddy current (with hole)

item	$A-\phi$		$T-\Omega$		measured
	nodal	edge	nodal	edge	
amplitude of eddy current $ I_e $ (A)	449	451	450	450	444
error $\varepsilon_3$ (%)	1.13	1.58	1.35	1.35	—

Table 3 Discretization data and CPU time

item	without hole				with hole			
	$A-\phi$		$T-\Omega$		$A-\phi$		$T-\Omega$	
	nodal	edge	nodal	edge	nodal	edge	nodal	edge
number of elements	14400							
number of nodes	16275							
number of unknowns	43417	41060	22844	22412	42885	41060	22844	22412
number of non-zero entries	1781644	653718	632859	423056	1734684	653718	632859	423056
computer storage (MB)	72.2	28.4	30.7	19.4	70.5	28.4	30.7	19.4
number of iterations of ICCG method	1306	513	172	192	1264	582	1141	327
CPU time (s)	6242	947	533	290	5870	1069	2001	442

Computer used : NEC supercomputer SX-1E  
(maximum speed : 285 MFLOPS)

convergence criterion of ICCG method :  $10^{-7}$

Fig.14 shows the 2-D model for verification of the torque calculation[15]. The stator core is made of non-oriented silicon steel (AISI: M-36). The rotor is composed of 4 poles. The rotor shaft is made of carbon steel. The rotor magnets are made of  $\text{SmCo}_5$  ( $B_r=0.9\text{T}$ ,  $H_c=7.0 \times 10^6 \text{ A/m}$ ), and magnetized in parallel. Twelve participants solved the cogging torque and seven groups measured it.

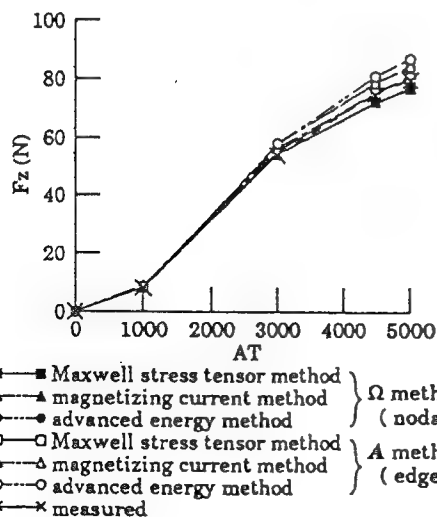


Fig.11 · z-component  $F_z$  of electromagnetic force.

Figure 10 consists of two plots, (a) and (b), showing the dependence of the force  $F_z$  (N) on the number of elements  $n_c$  for different methods. The x-axis for both plots is  $n_c$  on a logarithmic scale from  $10^3$  to  $10^5$ . The y-axis is  $F_z$  (N). Plot (a) is for 1000 AT and plot (b) is for 5000 AT. The methods are grouped into three categories:  $\Omega$  method (nodal),  $\Lambda$  method (edge), and  $\Lambda$  method (nodal).

Plot (a) 1000 AT:

- $\Omega$  method (nodal):  $F_z$  values are approximately 8.5, 8.8, 9.0, 9.2, 9.5, 9.8, 10.0, 10.5, 11.0, 11.5, 12.0 N.
- $\Lambda$  method (edge):  $F_z$  values are approximately 6.5, 7.0, 7.5, 8.0, 8.5, 9.0, 9.5, 10.0, 10.5, 11.0, 11.5 N.
- $\Lambda$  method (nodal):  $F_z$  values are approximately 4.5, 5.0, 5.5, 6.0, 6.5, 7.0, 7.5, 8.0, 8.5, 9.0, 9.5 N.

Plot (b) 5000 AT:

- $\Omega$  method (nodal):  $F_z$  values are approximately 95, 98, 100, 102, 105, 108, 110, 112, 115, 118, 120 N.
- $\Lambda$  method (edge):  $F_z$  values are approximately 85, 90, 95, 100, 105, 110, 115, 120, 125, 130, 135 N.
- $\Lambda$  method (nodal):  $F_z$  values are approximately 60, 65, 70, 75, 80, 85, 90, 95, 100, 105, 110 N.

Figure 1 consists of two schematic diagrams, (a) and (b), showing the cross-sections of a magnet. Diagram (a) is a cross-section in the  $x-z$  plane, with the  $z$ -axis vertical and the  $x$ -axis horizontal. It shows a central vertical region labeled 'center pole', flanked by two vertical regions labeled 'coil', and an outer region labeled 'yoke'. Diagram (b) is a cross-section in the  $y-z$  plane, with the  $z$ -axis vertical and the  $y$ -axis horizontal. It shows a central vertical region labeled 'center pole', flanked by two vertical regions labeled 'coil', and an outer region labeled 'yoke'. Both diagrams include coordinate axes  $x$ ,  $y$ , and  $z$ .

54



is used. The cogging torque,  $T$ , is calculated using the Maxwell stress tensor method and the advanced energy method. In order to obtain the cogging torque as a function of rotor angular displacement, numerical field solutions are obtained for different rotor positions.

The torque is calculated for two kinds of mesh patterns as shown in Fig.17. Fig.18 shows the effect of the mesh pattern on the torque calculated. The figure suggests that the results obtained by the Maxwell stress tensor method are affected by the mesh pattern. On the contrary, the results obtained by the advanced energy method are scarcely affected by the mesh pattern. Fig.19 shows the effect of the position of integration path in the air gap of the Maxwell stress tensor method on the calculated cogging torque under no load. The result obtained for the fine mesh ( $n_e=17352$ ) and the measured result are also shown. The figure suggests that the accuracy of the result for the integration path along the middle contour ( $r=11.75\text{mm}$ ,  $r$ : radius from the center of rotor shaft) in the air gap and that along the rotor side contour ( $r=11.55\text{mm}$ ) are better than that along the stator side contour ( $r=11.95\text{mm}$ ). This is because the change of the flux distribution is significant near the teeth of the stator.

The cogging torque calculated using 3-D analysis is compared with that using 2-D analysis[16]. It is shown that the result of 3-D analysis is a little closer to the measured result.

Fig.20 shows a linear motor model[12]. The field is composed of yoke (steel) and 2 pole ferrite magnets. The

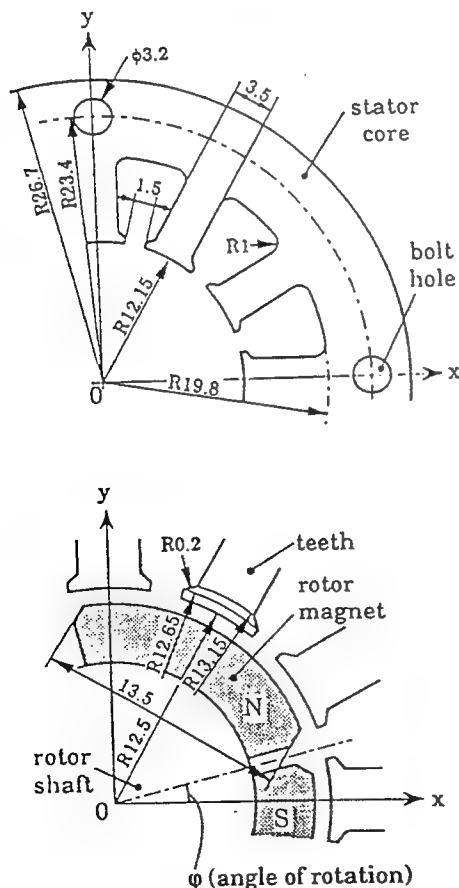


Fig.14 2-D model for verification of torque calculation.

armature core is made of steel. The number of turns of each winding is 50. Fig.21 shows the comparison of calculated and measured thrust and attractive forces.

Fig.22 shows a model of salient-pole synchronous machine[12]. The number of poles is 6. The core is made of non-oriented silicon steel (AISI: M-47). Fig.23 shows the calculated flux distributions in the air gap.

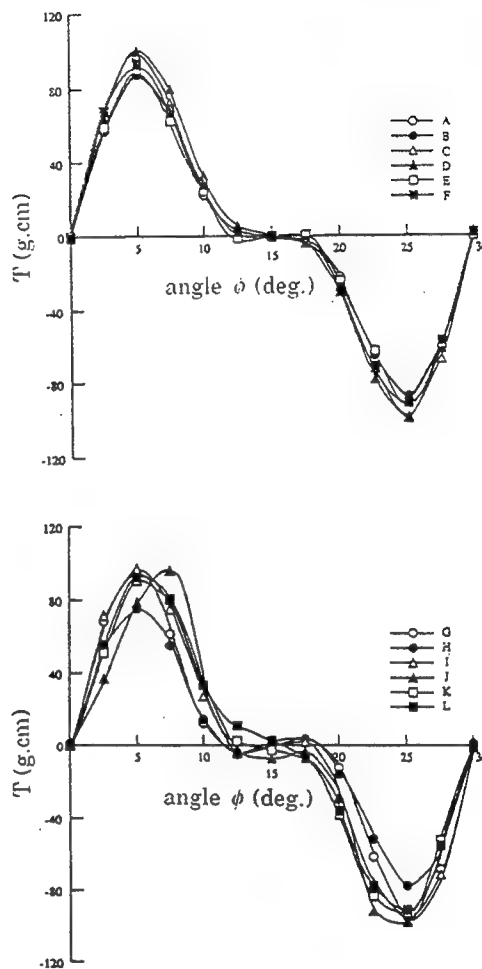


Fig.15 Cogging torques calculated by twelve participants.

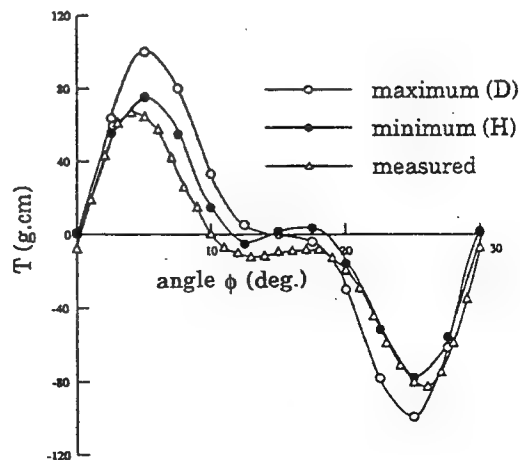
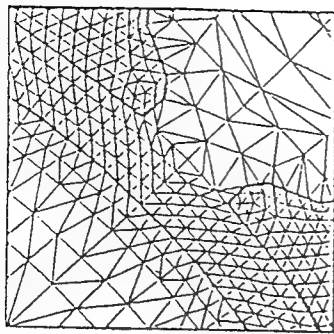
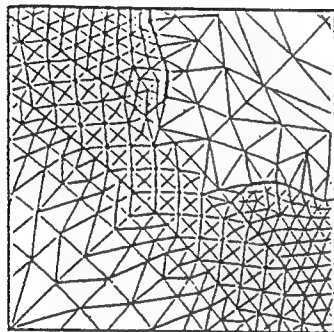


Fig.16 Maximum and minimum calculated cogging torques and measured one.

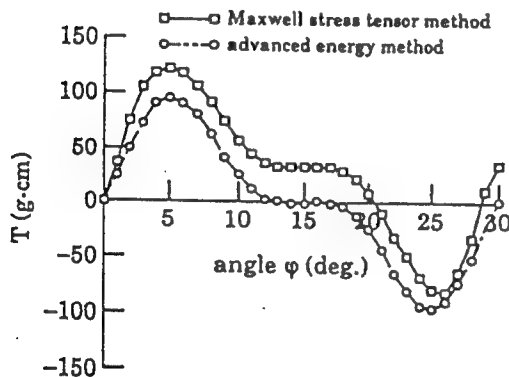


(a) mesh-1

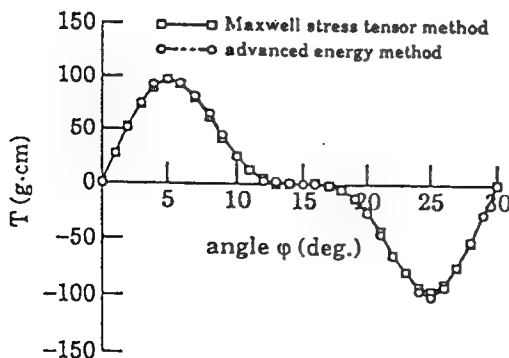


(b) mesh-2

Fig.17 Mesh in and around gap ( $n_e=4338$ ).



(a) mesh-1



(b) mesh-2

Fig.18 Effect of subdivision in air gap.

B. 1993-1995

In the "Investigation Committee on Highly Accurate Simulation Technique for Rotating Machines" (1993-1995, Chairman: M. Itoh, Hitach Ltd.), the torque under load and the load current, etc. of the permanent magnet motor model shown in Fig.14 are analyzed[17]. Fig.24 shows the connection of stator windings. Fig.25 shows the torque-speed characteristics[18]. Torques under various excitation conditions are analyzed[19,20].

#### 4. MODELS FOR COMPARING OPTIMIZATION METHODS (1993-1996)

The "Investigation Committee on Electromagnetic Field Analysis and Its Application to Optimization Problems" (1993-1996, Chairman: T. Takuma, Kyoto Univ.) proposed five kinds of models for the comparison of optimization methods[21].

Fig.26 shows a model of die press with electromagnet for orientation of magnetic powder[22]. This is used for producing anisotropic permanent magnets. The die press is made of steel. The die molds are set to form the radial

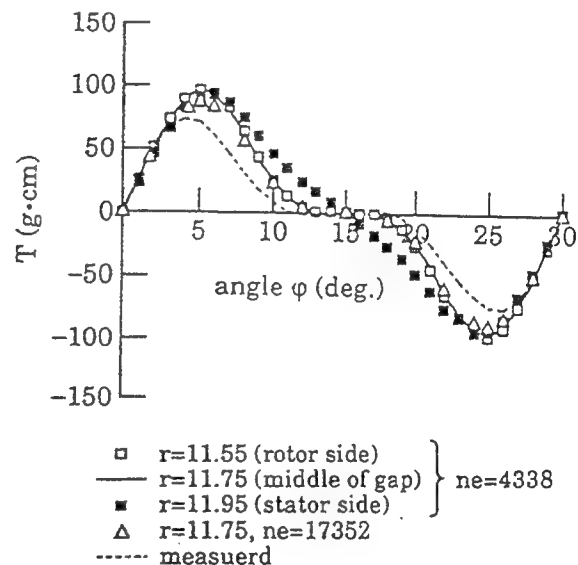


Fig.19 Cogging torque.

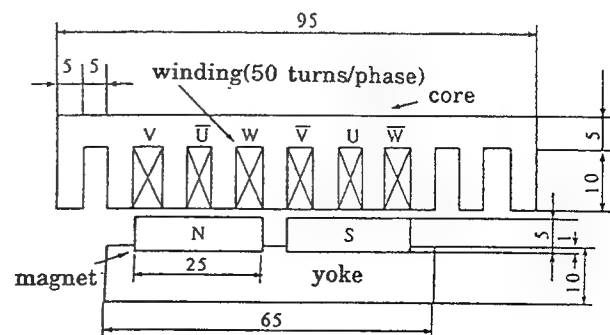
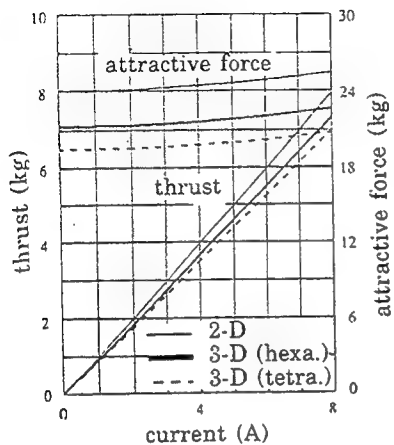


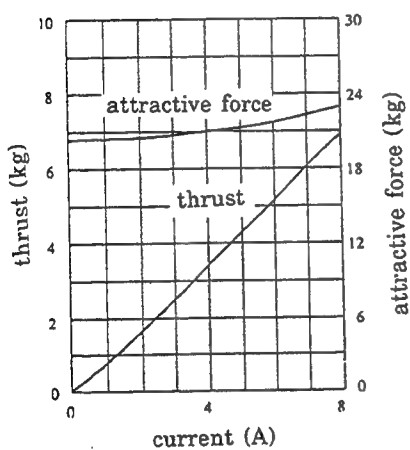
Fig.20 Linear motor model.

flux distribution. The magnetic powder is inserted in the cavity. The ampere-turns of each coil are 33.7kAT. x- and y-components  $B_x$  and  $B_y$  of flux density at the points along the line e-f in the cavity are specified as follows:

$$\left. \begin{aligned} B_x &= 1.5 \cos \theta(T) \\ B_y &= 1.5 \sin \theta(T) \end{aligned} \right\} \quad (2)$$

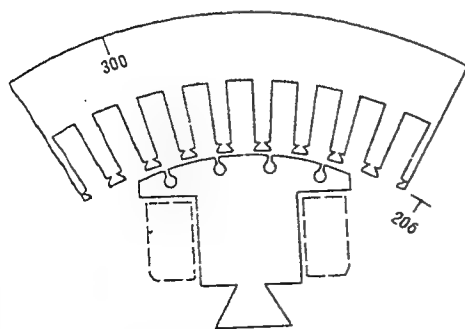


(a) calculated



(b) measured

Fig.21 Thrust and attractive force.



minimum gap : 1.3mm  
thickness of core : 100mm

Fig.22 Synchronous machine model

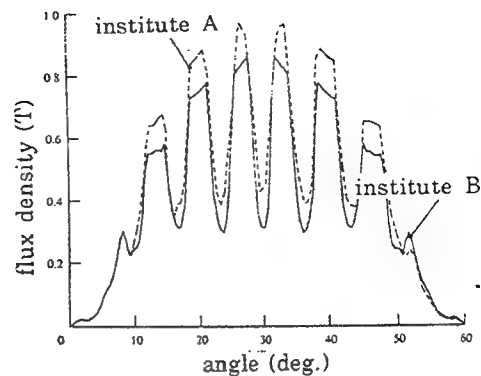


Fig.23 Flux distribution along air gap (1300AT).

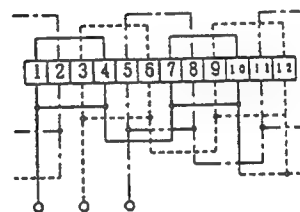
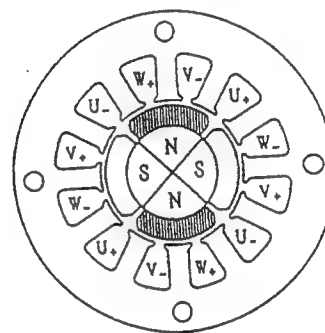


Fig.24 Connection of stator winding.

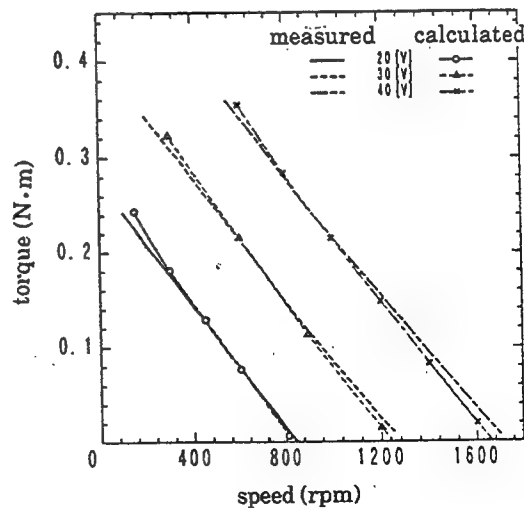


Fig.25 Torque-speed characteristics.

where  $\theta$  is the angle measured from the x-axis. The following four kinds of optimization methods are applied to this model.

(a) Physical and Engineering Investigation Method (PEM)

The shape of the magnetic circuit is examined from the physical and engineering viewpoint (Fig.27(a)). Finally four kinds of design variables ( $r_1$ - $r_4$ ) are chosen as shown in Fig.27 (b) and the final result using the simulated annealing method is shown in Fig.27(c).

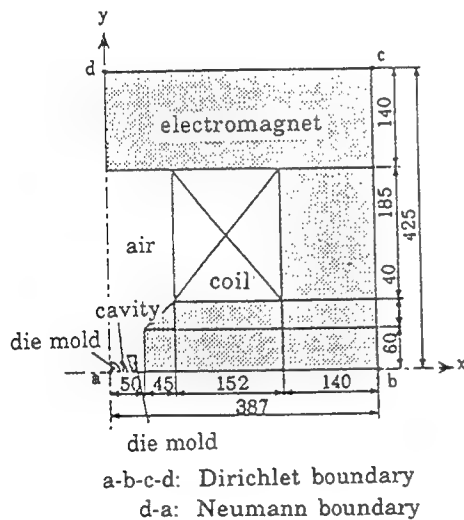
(b) Genetic Algorithm Method (GAM)

Fig.28 (a) shows the initial shape. The points 1-6 are moved in the radial direction, whereas the points 7-12 are moved in the x-direction. 4 bits are specified for each GA node. Fig.28 (b) shows the final shape obtained after 190 generations.

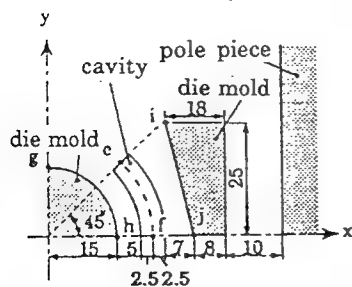
(c) Rosenbrock's Method (RBM) and Simulated Annealing Method (SAM)

Fig.29 (a) denotes the definition of design variables. n-p and k-m are denoted by ellipses whose long and short axes are L1, L2, L3 and L4. Fig.29 (b) shows the final shapes obtained using RBM and SAM.

Fig. 30 shows the comparison of the amplitude and direction of the flux density vector which are obtained using four kinds of methods. The advantage and disadvantage of each method should be investigated in the future.

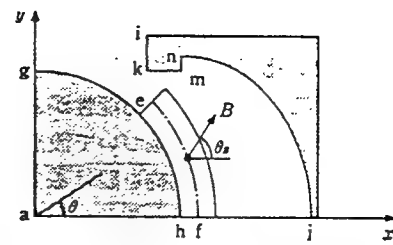


(a) whole view

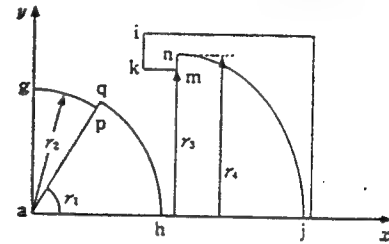


(b) enlarged view

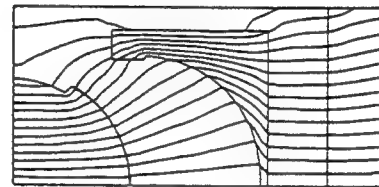
Fig.26 Model of die press with electromagnet.



(a) investigation of shape of magnetic circuit

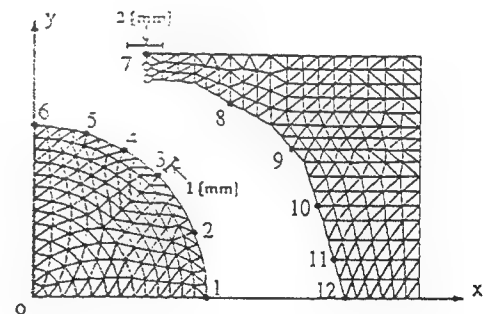


(b) choice of design variables

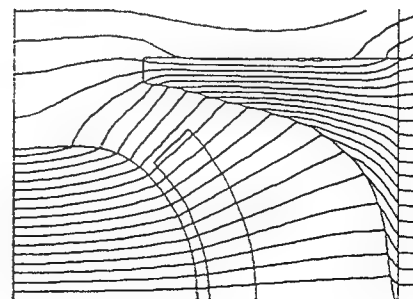


(c) final shape

Fig.27 Optimization by physical and engineering investigation method (PEM).



(a) points to be moved



(b) final shape

Fig.28 Optimization by genetic algorithm (GA).

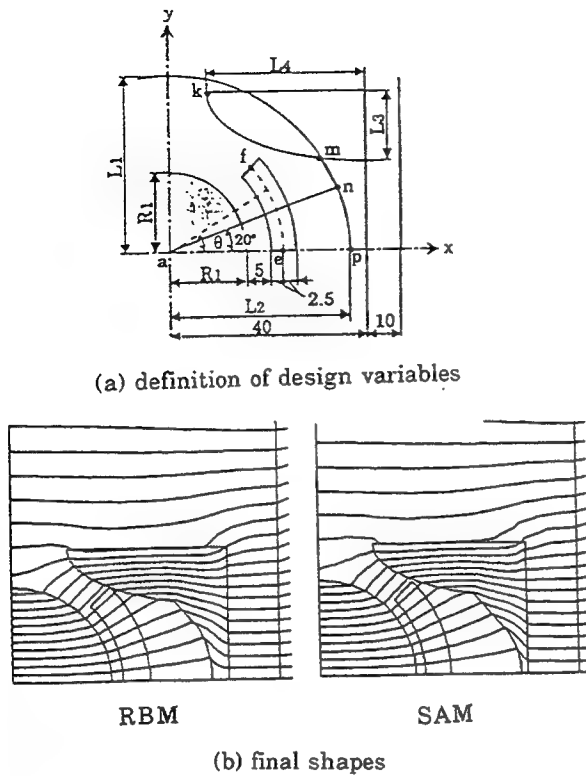


Fig.29 Optimization by Rosenbrock's method (RBM) and simulated annealing method (SAM).

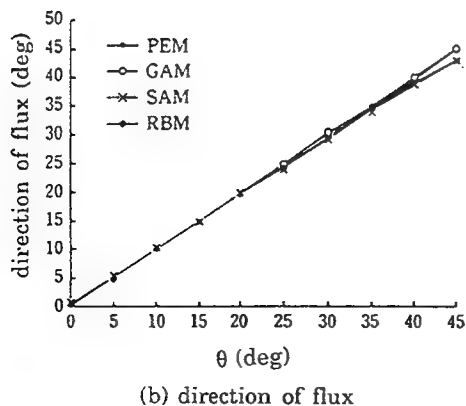
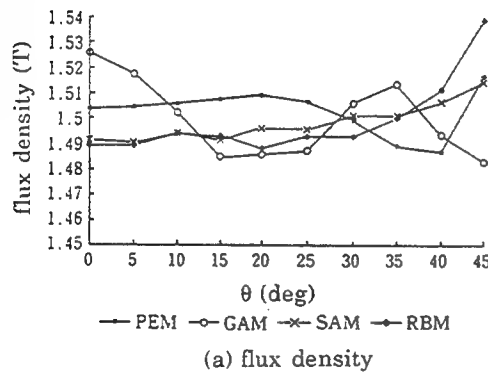


Fig.30 Flux density and direction of flux at final shape.

Fig.31 shows a superconducting MRI magnet model[21]. The uniform flux density is 1.5T. The required uniformity in the center sphere (radius: 200mm) is less than 5ppm. Fig.32 shows the obtained result using the quasi-Newton method and theoretical equation of magnetic field[23]. The obtained uniformity is 0.4ppm.

Fig.33 shows the axi-symmetric electrode model[21]. Fig.34 shows the obtained shape of the electrode which

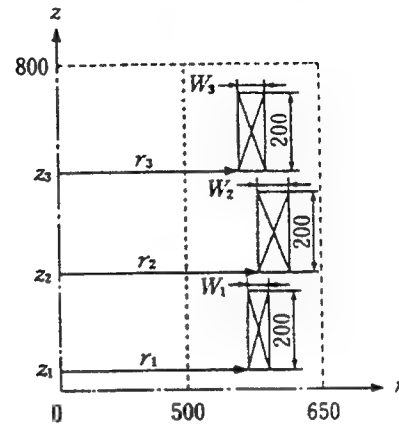


Fig.31 MRI magnet model.

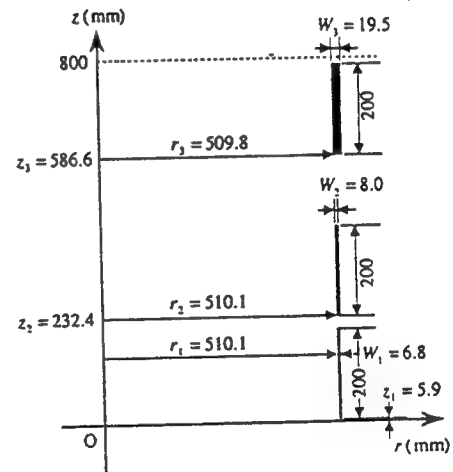


Fig.32 Optimal configuration.

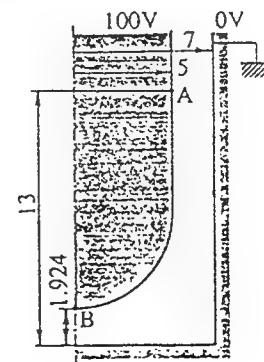


Fig.33 Axi-symmetric electrode model.

produces the uniform electric field intensity[24]. The electric field is calculated using the charge simulation method (CSM) and the surface charge method (SCM).

Fig.35 shows the sphere electrode in a cube[21]. Fig.36 shows the obtained shape of the electrode which produces the uniform electric field intensity[24].

Fig.37 shows the 3-D shielding model[21]. The ferrite plate has the relative permeability of 1000 and is

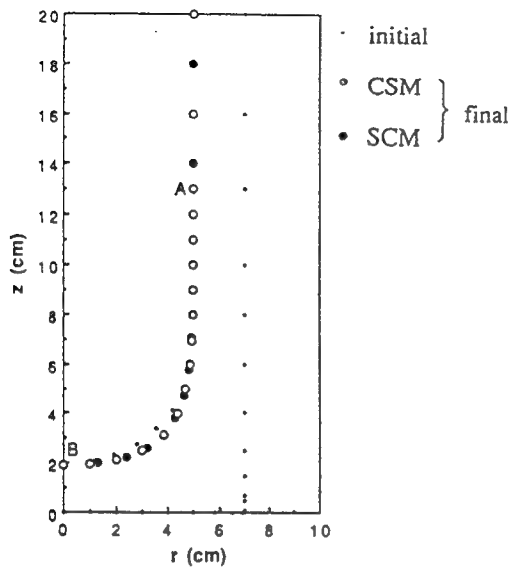


Fig.34 Obtained shape of axis-symmetric electrode.

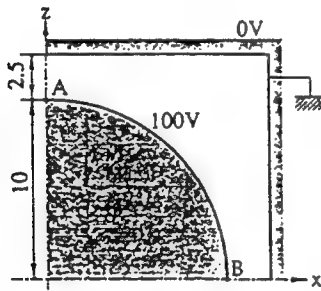


Fig.35 Sphere electrode model.

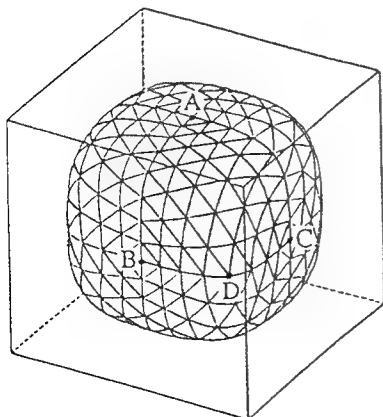


Fig.36 Obtained shape of 3-D electrode.

energized by 39789AT. Fig.38 shows the obtained shape of the plate having various partial thickness so that the maximum value of the flux density in the observation area is less than 0.005T.

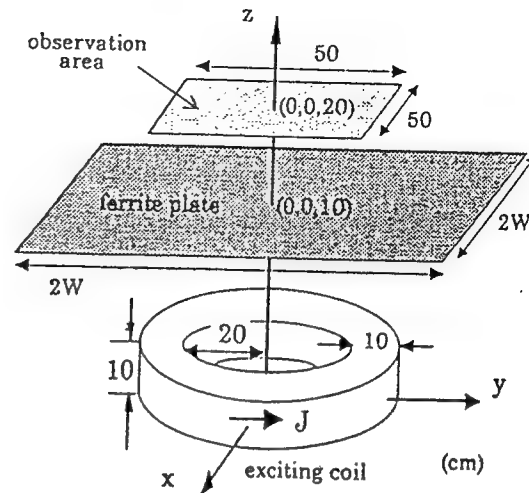


Fig.37 3-D magnetic shield model.

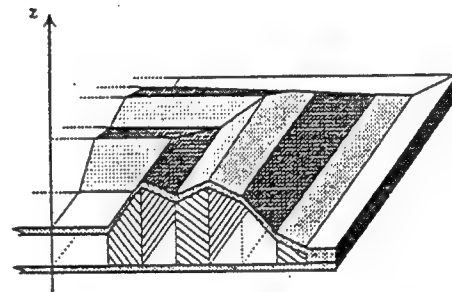


Fig.38 Obtained plate shape.

## 5. CONCLUSIONS

The verification models proposed by the investigation committees of IEE of Japan and some results are discussed. Various knowledge related to electromagnetic field calculation was obtained by using these models. The detailed discussion is written in each paper. Some models (Fig.10 and the modified version of Fig.26) were also adopted as TEAM Workshop problems (Problems 20 and 25[25]).

The verification of the following problems should be investigated in the future:

- (a) modeling of material properties, such as anisotropy, hysteresis and superconductivity,
- (b) coupled problems with heat and fluid flow,
- (c) optimization method of actual machines.

I think such activities of the verification of softwares using various models shown in this paper made considerable contribution to the progress of the electromagnetic field calculation in Japan.

## REFERENCES

- [1] IEEJ Technical Report, no.286, "Numerical technique for analyzing 3-D magnetostatic field", 1988.

- [2] T. Nakata, N. Takahashi and K. Fujiwara, "3-D finite element analysis of magnetic fields of IEEJ model", *Electromagnetic Fields in Electrical Engineering*, pp.285-288, Pergamon Press, 1988.
- [3] Y. Kanai, T. Abe, M. Sengoku, T. Iijima, M. Iizuka and K. Mukasa, "Further discussion on magnetic vector potential finite-element formulation for three-dimensional magnetostatic field analysis," *IEEE Trans. on Magnetics*, vol.26, no.2, pp.411-414, 1990.
- [4] T. Nakata, N. Takahashi, K. Fujiwara and T. Imai, "Effects of permeability of magnetic materials on errors of the T-W method," *IEEE Trans. on Magnetics*, vol.26, no.2, pp.698-701, 1990.
- [5] K. Sawa and T. Hirano, "An evaluation of the computational error near the boundary with magnetostatic field calculation by B.E.M.," *IEEE Trans. on Magnetics*, vol.26, no.2, pp.403-406, 1990.
- [6] IEEJ Technical Report, no.384, "Numerical technique for analyzing 3-D eddy current", 1991.
- [7] T. Nakata, N. Takahashi, K. Fujiwara, T. Imai and K. Muramatsu, "Comparison of various methods of analysis and finite elements in 3-D magnetic field analysis", *IEEE Trans. on Magnetics*, vol.27, no.5, pp.4073-4076, 1991.
- [8] P. Robert, M. Ito and T. Takahashi, "Numerical solution of three dimensional transient eddy current problems by the A-f method," *IEEE Trans. on Magnetics*, vol.28, no.2, pp.1166-1169, 1992.
- [9] T. Onuki and S. Wakao, "Novel boundary element formulation in hybrid FE-BE method for electromagnetic field computations," *IEEE Trans. on Magnetics*, vol.28, no.2, pp.1162-1165, 1992.
- [10] T. Onuki and S. Wakao, "Novel boundary element analysis for 3-D eddy current problems," *IEEE Trans. on Magnetics*, vol.29, no.2, pp.1520-1523, 1993.
- [11] Y. Tanaka, "Three-dimensional eddy current analysis by the finite element method with integral equations using T- $\Omega$ ," *IEEE Trans. on Magnetics*, vol.28, no.2, pp.1150-1153, 1992.
- [12] IEEJ Technical Report, no.486, "Software for numerical analysis of magnetic fields in rotating machines", 1994.
- [13] T. Nakata, N. Takahashi, Suhartono and H. Morishige, "Investigation of a model to verify softwares for 3-D static force calculation", *IEEE Trans. on Magnetics*, vol.30, no.5, pp.3483-3486, 1994.
- [14] T. Nakata and N. Takahashi, "Verification of 3-D software for calculating electromagnetic force", *Electromagnetic Field Problems and Applications*, International Academic Publishers, pp.7-10, 1993.
- [15] N. Takahashi, T. Nakata and H. Morishige, "Verification of software for calculating electromagnetic force and torque using IEEJ model", *Software Applications in Electrical Engineering*, pp.221-227, Computational Mechanics Publications, 1993.
- [16] Y. Kawase, T. Yamaguchi and Y. Hayashi, "Analysis of cogging torque of permanent magnet motor by 3-D finite element method," *IEEE Trans. on Magnetics*, vol.31, no.3, pp.2044-2047, 1995.
- [17] IEEJ Technical Report, no.565, "Highly accurate simulation technique for rotating machines", 1995.
- [18] N. Igura, T. Shimomura, K. Harada, Y. Ishihara and T. Todaka, "A proposal for rotating machineries analysis by considering the unknown equal potential condition on FEM," *IEEE Trans. on Magnetics*, vol.31, no.3, pp.1722-1724, 1995.
- [19] Y. Kawase, Y. Hayashi, T. Yamaguchi, Y. Ishihara and Y. Kitamura, "3-D finite element analysis of permanent-magnet motor excited from square pulse voltage source," *IEEE Trans. on Magnetics*, vol.32, no.3, pp.1537-1540, 1996.
- [20] T. Yamaguchi, Y. Kawase and Y. Hayashi "Dynamic transient analysis of vector controlled motors using 3-D finite element method," *IEEE Trans. on Magnetics*, vol.32, no.3, pp.1549-1552, 1996.
- [21] IEEJ Technical Report, no.611, "Electromagnetic field analysis and its application to optimization problems", 1996.
- [22] N. Takahashi, K. Ebihara, K. Yoshida, T. Nakata, K. Ohashi and K. Miyata, "Investigation of simulated annealing method and its application to optimal design of die mold for orientation of magnetic powder", *IEEE Trans. on Magnetics*, vol.32, no.3, pp.1210-1213, 1996.
- [23] M. Kitamura, S. Kakukawa, K. Mori and T. Tominaka, "An optimal design technique for coil configurations in iron-shielded MRI magnets," *IEEE Trans. on Magnetics*, vol.30, no.4, pp.2352-2355, 1994.
- [24] H. Tsuboi and T. Misaki, "Optimization of electrode and insulator contours by using Newton method", *Trans. of IEE of Japan*, vol.106, no.7, pp.307-314, 1986.
- [25] Proceedings of the TEAM Workshop in the Sixth Round, Okayama, 1996.
- [26] T. Nakata, K. Fujiwara, M. Nakano and T. Kayada, "Effects of construction of yokes on the accuracy of a single sheet tester", *Anales de Fisica, Serie B*, vol.86, pp.190-192, 1990.





## 1997 INSTITUTIONAL MEMBERS

THE AEROSPACE CORPORATION  
PO Box 92957  
Los Angeles, CA 90009-2957

ANDREW CORPORATION  
10500 W. 153rd Street  
Orland Park, IL 60462

BIN 293 HIGH PERFORMANCE  
PO Box 830702  
Birmingham, AL 35283-0702

BOEING NORTH AMERICAN SVCS  
1745 Jefferson Davis Hwy  
Arlington, VA 22202

BRITISH AEROSPACE  
FPC 267 PO Box 5  
Filton, BRISTOL, UK BS12 7QW

BRITISH BROADCASTING CO R&D  
Kingswood Warren  
Tadworth, SURREY, UK KT20 6NP

CAMBRIDGE CONSULTANTS, LTD.  
Milton Road, Science Park  
Cambridge, CAMBS, UK CB5 4DW

CHALMERS UNIV. OF TECH.  
Microwave Technology  
Gothenburg, SWEDEN S 412 96

COMMUNICATOR CEC AB  
Box 1310  
Solna, SWEDEN 17125

CSC PROFESSIONAL SERVICE.  
10101 Senate Drive  
Lanham, MD 20706-4368

CSIRO, CTR FOR ADV. TECH.  
PO Box 883  
Kenmore, QLD, AUSTRALIA 4069

CULHAM LAB  
UK Atomic Energy Authority  
Abingdon, OXFORD, UK OX14 3DB

DARTMOUTH COLLEGE  
Feldberg Library  
Hanover, NH 03755-1809

D.L.R. OBERPFAFFENHOFEN  
Zentralbibliothek  
Wessling, OBB, GERMANY 8031

DEFENCE TECH & PROCUREMENT  
NEMP Lab, AC-Zentrum  
Spiez, SWITZERLAND CH 3700

DEFENSE RESEARCH ESTAB. LIB.  
3701 Carling Avenue  
Ottawa, ON, CANADA K1A 0Z4

DEUTSCHE TELEKOM AG  
PO Box 10-00-03  
Darmstadt, GERMANY D-64 276

E.T.S.E. TELECOMUNICACIONES  
Campus Lagoas Marcosende  
Vigo, SPAIN 36200

ELECTRICAL COMM. LAB,  
1-1 Hikarinooka Yokusuka Shi  
Kanagawa, KEN, MZ, JAPAN 239

ELECTRONICS RESEARCH INC.  
7777 Gardner Road  
Chandler, IN 47610-9219

ERA TECHNOLOGY LTD.  
Cleve Road  
Leatherhead, SURREY, UK KT22 7SA

ERICSSON SAAB AVIONICS AB  
Electromagnetic Technology  
Linköping, SWEDEN SE 58188

ESCUELA TRANSMISS. EJERCITO  
Ctr. Extremadura, KM, 10,200  
Madrid, SPAIN 28024

FANFIELD LTD.  
Braxted Park  
Witham, ESSEX, UK CM8 3XB

FGAN/FHP/AUS  
Neuenahr Strasse 20  
Wachtbert, Werth, GERMANY 53343

FOR-ON-TIME/TECHNION  
147-24 176<sup>TH</sup> Street  
Jamaica, NY 11434-5410

GEC MARCONI RES. CTR. LIB.  
W. Hanningfield Road, Gt. Baddow  
Chelmsford, ESSEX, UK CM2 8HN

HARRIS CORPORATION  
1680 University Avenue  
Rochester, NY 14610-9983

HARRY-YOUNG PUBLICATIONS  
6261 Manchester Blvd.  
Buena Park, CA 90621

HKUST, UNIVERSITY LIBRARY  
Clear Water Bay Road  
Kowloon, HONG KONG

HOKKAIDO DAIGAKU  
Nishi 8, Kita 13  
Sapporo, JAPAN 060

HUGHES RESEARCH LIBRARY  
3011 Malibu Canyon Road  
Malibu, CA 90265-4737

HUNTING ENGINEERING LTD.  
Reddings Wood, Ampthill  
Bedford, UK MK45 2HD

HYDRO-QUEBEC INST. OF RES.  
1800 Boul. Lionel-Boulet  
Varennes, PQ, CANADA J3X 1S1

IABG MBH, TRM  
Einsteinstrasse 20  
Ottobrunn, GERMANY D 85521

IIT RESEARCH INSTITUTE  
185 Admiral Cochrane Drive  
Annapolis, MD 21401-7396

IMAGINEERING LTD.  
95 Barber Greene Road, Ste. 112  
Toronto, ON, CANADA M3C 3E9

INFORMATION CENTRE  
A4 Bldg. Ively Road  
Farnborough, HAMPS. UK GU14 0LK

IPS RADIO & SPACE SVC/LIBRARY  
PO Box 5606  
W. Chatswood, AUSTRALIA 2057

KATHREIN-WERKE KG  
Postbox 100 444  
Rosenheim, GERMANY D-83004

LAVOISIER ABONNEMENTS  
14 Rue De Provigny  
Cachan, Cedex, FRANCE 94236

LICOSA LIBRARY  
Via Duca Di Calabria 1/1  
Florence, ITALY 50125

LINDA HALL LIBRARY  
5109 Cherry Street  
Kansas City, MO 64110-2498

MALARDALENS UNIVERSITY  
PO Box 883  
Vasteras, SWEDEN S 721-23

MATRA DEFENSE  
37 Av. Louis Breguet Bp 1  
Velizy Cedex, FRANCE 78590

METAWAVE COMMUNICATIONS  
8700 148th Avenue, N.E.  
Redmond, WA 98052

MISSISSIPPI STATE UNIV LIBRARY  
PO Box 9570  
Mississippi State, MS 39762

MITRE CORPORATION LIBRARY  
202 Burlington Road  
Bedford, MA 01730-1407

MOD(PE) DGSS  
Abbey Wood #54, PO Box 702  
Bristol, UK BS12 7DU

MOTOROLA  
2001 N. Division Street  
Harvard, IL 60033

MPB TECHNOLOGIES, INC.  
151 Hymus Blvd.  
Pointe-Claire, QC, CANADA H9R 1E9

MYERS ENGINEERING INTL, INC.  
PO Box 15908, 5425 NW 24th St.  
Margate, FL 33063

NATL RADIOLOGICAL PROT. BD.  
Chilton  
Didcot, OXON, UK OX11 0RG

NGIC  
220 7th Street, NE  
Charlottesville, VA 22902-5396

NIKSAR  
35/45 Gilbey Road  
Mt. Waverley, VIC, AUSTRALIA 3149

NORTEL TECHNOLOGY  
London Road  
Harlow, ESSEX, UK CM17 9NA

NTT WIRELESS SYSTEMS LABS.  
1-1 Hikarinooka Yokosuka-Shi  
Kanagawa, JAPAN239

PENN STATE UNIV LIBRARY  
Pattee Library  
University Park, PA 16802

PHILIPS RESEARCH  
Prof. Holstlaan 4  
Eindhoven, NETHERLANDS 11172j

QUEEN MARY & WESTFIELD COLL  
Mile End Road  
London, UK E1 4NS

RADIO FREQUENCY SYSTEMS  
36 Garden Street  
Kilsyth, VIC, AUSTRALIA 3137

RAND AFRIKAANS UNIVERSITY  
PO Box 524, Aucklandpark  
Johannesburg, S AFRICA 2006

RAYTHEON E-SYSTEMS  
PO Box 6056  
Greenville, TX 75403

SONY CORPORATION  
174 Fujitsukacho, Hodogaya Ku  
Yokohama MZ, JAPAN 240

SOUTHWEST RESEARCH INST.  
6220 Culebra Road  
San Antonio, TX 78238

SWETS SUBSCRIPTION SERVICE  
440 Creamery Way, Suite A  
Exton, PA 19341

TAMPERE UNIVERSITY OF TECH  
PO Box 692  
Tampere, FINLAND 33101

TASC - LIBRARY  
55 Walkers Brook Drive  
Reading, MA 01867-3297

TECHNISCHE UNIV. DELFT  
Mekelweg 4, Delft  
HOLLAND, NETHERLANDS 2628 CD

TELEBRAS - CPQD, LIB.  
Rod. Campinas  
Campinas, SP BRAZIL 13088-061

TELSTRA LIBRARY  
Private Bag 37  
Clayton, VIC, AUSTRALIA 3168

TELSTRA RESEARCH LABS  
770 Blackburn Road  
Clayton, VIC, AUSTRALIA 3168

THE ULTRA CORPORATION  
PO Box 50, University Station  
Syracuse, NY 13210-0050

UNIV OF CENTRAL FLORIDA LIB.  
PO Box 162440  
Orlando, FL 32816-2440

UNIV OF COLORADO LIB.  
Campus Box 184  
Boulder, CO 80309-0184

UNIV OF MISSOURI-ROLLA LIB.  
1870 Miner Circle  
Rolla, MO 65409-0001

UNIVERSITAT DER BUNDESWEHR  
Werner Heisenberg Weg 39  
Neubiberg, GERMANY D-85577

US COAST GUARD ACADEMY  
15 Mohegan Avenue  
New London, CT 06320-4195

VECTOR FIELDS LTD.  
24 Bankside Kidlington  
Oxford, UK OX5 1JE

VIT, TECHNICAL RESEARCH. CTR.  
PO Box 1202  
Espoo, FINLAND FIN-02044

# ACES COPYRIGHT FORM

This form is intended for original, previously unpublished manuscripts submitted to ACES periodicals and conference publications. The signed form, appropriately completed, MUST ACCOMPANY any paper in order to be published by ACES. PLEASE READ REVERSE SIDE OF THIS FORM FOR FURTHER DETAILS.

TITLE OF PAPER:

AUTHORS(S)

PUBLICATION TITLE/DATE:

RETURN FORM TO:

Dr. Richard W. Adler  
Naval Postgraduate School  
Code EC/AB  
833 Dyer Road, Room 437  
Monterey, CA 93943-5121 USA

---

## PART A - COPYRIGHT TRANSFER FORM

(NOTE: Company or other forms may not be substituted for this form. U.S. Government employees whose work is not subject to copyright may so certify by signing Part B below. Authors whose work is subject to Crown Copyright may sign Part C overleaf).

The undersigned, desiring to publish the above paper in a publication of ACES, hereby transfer their copyrights in the above paper to The Applied Computational Electromagnetics Society (ACES). The undersigned hereby represents and warrants that the paper is original and that he/she is the author of the paper or otherwise has the power and authority to make and execute this assignment.

**Returned Rights:** In return for these rights, ACES hereby grants to the above authors, and the employers for whom the work was performed, royalty-free permission to:

1. Retain all proprietary rights other than copyright, such as patent rights.
2. Reuse all or portions of the above paper in other works.
3. Reproduce, or have reproduced, the above paper for the author's personal use or for internal company use provided that (a) the source and ACES copyright are indicated, (b) the copies are not used in a way that implies ACES endorsement of a product or service of an employer, and (c) the copies per se are not offered for sale.
4. Make limited distribution of all or portions of the above paper prior to publication.
5. In the case of work performed under U.S. Government contract, ACES grants the U.S. Government royalty-free permission to reproduce all or portions of the above paper, and to authorize others to do so, for U.S. Government purposes only.

**ACES Obligations:** In exercising its rights under copyright, ACES will make all reasonable efforts to act in the interests of the authors and employers as well as in its own interest. In particular, ACES REQUIRES that:

1. The consent of the first-named author be sought as a condition in granting re-publication permission to others.
2. The consent of the undersigned employer be obtained as a condition in granting permission to others to reuse all or portions of the paper for promotion or marketing purposes.

In the event the above paper is not accepted and published by ACES or is withdrawn by the author(s) before acceptance by ACES, this agreement becomes null and void.

---

AUTHORIZED SIGNATURE

TITLE (IF NOT AUTHOR)

---

EMPLOYER FOR WHOM WORK WAS PERFORMED

DATE FORM SIGNED

## PART B - U.S. GOVERNMENT EMPLOYEE CERTIFICATION

(NOTE: If your work was performed under Government contract but you are not a Government employee, sign transfer form above and see item 5 under Returned Rights).

This certifies that all authors of the above paper are employees of the U.S. Government and performed this work as part of their employment and that the paper is therefore not subject to U.S. copyright protection.

---

AUTHORIZED SIGNATURE

TITLE (IF NOT AUTHOR)

---

NAME OF GOVERNMENT ORGANIZATION

DATE FORM SIGNED

## PART C - CROWN COPYRIGHT

(Note: ACES recognizes and will honor Crown Copyright as it does U.S. Copyright. It is understood that, in asserting Crown Copyright, ACES in no way diminishes its rights as publisher. Sign only if ALL authors are subject to Crown Copyright.

This certifies that all authors of the above Paper are subject to Crown Copyright. (Appropriate documentation and instructions regarding form of Crown Copyright notice may be attached).

AUTHORIZED SIGNATURE

TITLE OF SIGNED

NAME OF GOVERNMENT BRANCH

DATE FORM SIGNED

### Information to Authors

#### ACES POLICY

ACES distributes its technical publications throughout the world, and it may be necessary to translate and abstract its publications, and articles contained therein, for inclusion in various compendiums and similar publications, etc. When an article is submitted for publication by ACES, acceptance of the article implies that ACES has the rights to do all of the things it normally does with such an article.

In connection with its publishing activities, it is the policy of ACES to own the copyrights in its technical publications, and to the contributions contained therein, in order to protect the interests of ACES, its authors and their employers, and at the same time to facilitate the appropriate re-use of this material by others.

The new United States copyright law requires that the transfer of copyrights in each contribution from the author to ACES be confirmed in writing. It is therefore necessary that you execute either Part A-Copyright Transfer Form or Part B-U.S. Government Employee Certification or Part C-Crown Copyright on this sheet and return it to the Managing Editor (or person who supplied this sheet) as promptly as possible.

#### CLEARANCE OF PAPERS

ACES must of necessity assume that materials presented at its meetings or submitted to its publications is properly available for general dissemination to the audiences these activities are organized to serve. It is the responsibility of the authors, not ACES, to determine whether disclosure of their material requires the prior consent of other parties and if so, to obtain it. Furthermore, ACES must assume that, if an author uses within his/her article previously published and/or copyrighted material that permission has been obtained for such use and that any required credit lines, copyright notices, etc. are duly noted.

#### AUTHOR/COMPANY RIGHTS

If you are employed and you prepared your paper as a part of your job, the rights to your paper initially rest with your employer. In that case, when you sign the copyright form, we assume you are authorized to do so by your employer and that your employer has consented to all of the terms and conditions of this form. If not, it should be signed by someone so authorized.

**NOTE RE RETURNED RIGHTS:** Just as ACES now requires a signed copyright transfer form in order to do "business as usual", it is the intent of this form to return rights to the author and employer so that they too may do "business as usual". If further clarification is required, please contact: The Managing Editor, R.W. Adler, Naval Postgraduate School, Code EC/AB, Monterey, CA, 93943, USA (408)656-2352.

Please note that, although authors are permitted to re-use all or portions of their ACES copyrighted material in other works, this does not include granting third party requests for reprinting, republishing, or other types of re-use.

#### JOINT AUTHORSHIP

For jointly authored papers, only one signature is required, but we assume all authors have been advised and have consented to the terms of this form.

#### U.S. GOVERNMENT EMPLOYEES

Authors who are U.S. Government employees are not required to sign the Copyright Transfer Form (Part A), but any co-authors outside the Government are.

Part B of the form is to be used instead of Part A only if all authors are U.S. Government employees and prepared the paper as part of their job.

**NOTE RE GOVERNMENT CONTRACT WORK:** Authors whose work was performed under a U.S. Government contract but who are not Government employees are required to sign Part A-Copyright Transfer Form. However, item 5 of the form returns reproduction rights to the U.S. Government when required, even though ACES copyright policy is in effect with respect to the reuse of material by the general public.

RICHARD W. ADLER, EXECUTIVE OFFICER  
ECE DEPARTMENT, CODE ECAB, NAVAL POSTGRADUATE SCHOOL, 833 DYER ROAD, RM 437, MONTEREY, CA 93943-5121  
PHONE: 408-646-1111 FAX: 408-649-0300 EMAIL: RWA@IBM.NET  
please print

**please print**

COMPANY/ORGANIZATION/UNIVERSITY DEPARTMENT/MAIL STATION

**PLEASE LIST THE ADDRESS YOU WANT USED FOR PUBLICATIONS**

MAILING ADDRESS

CITY	PROVINCE/STATE	COUNTRY	ZIP/POSTAL CODE
------	----------------	---------	-----------------

TELEPHONE \_\_\_\_\_ FAX \_\_\_\_\_ AMATEUR RADIO CALL SIGN \_\_\_\_\_

E-MAIL ADDRESS \_\_\_\_\_ E-MAIL ADDRESS CAN BE INCLUDED IN ACES DATABASE ☐ YES ☐ NO

PERMISSION IS GRANTED TO HAVE MY NAME PLACED ON MAILING LISTS WHICH MAY BE SOLD ☐ YES ☐ NO

AREA	INDIVIDUAL SURFACE MAIL	INDIVIDUAL AIRMAIL	ORGANIZATIONAL (AIRMAIL ONLY)
U.S. & CANADA	( ) \$65	( ) \$65	( ) \$115
MEXICO,CENTRAL & SOUTH AMERICA	( ) \$68	( ) \$70	( ) \$115
EUROPE, FORMER USSR, TURKEY, SCANDINAVIA	( ) \$68	( ) \$78	( ) \$115
ASIA, AFRICA, MIDDLE EAST & PACIFIC RIM	( ) \$68	( ) \$85	( ) \$115

**FULL-TIME STUDENT/RETIRED/UNEMPLOYED RATE IS \$25 FOR ALL COUNTRIES**

**Non-USA participants:** Prices are in U.S. dollars. All currencies must be converted to U.S. dollars payable by banks with U.S. affiliates. (1) Bank Checks, must have U.S. address of bank; (2) Traveler's Checks (in U.S. \$\$); (3) U.S./International Money Order drawn in U.S. funds, payable in U.S.. (4) Credit Cards: Visa, MasterCard, Amex and Discover.

**PAYMENT METHOD: ALL CHECKS/TRAVELER'S CHECKS/MONEY ORDERS ARE PAYABLE TO "ACES"**

☐ CHECK (PAYABLE TO ACES)      ☐ TRAVELER'S CHECKS      ☐ INTERNATIONAL MONEY ORDER

☐ CREDIT CARD      ☐ VISA      ☐ MASTERCARD      ☐ AMEX      ☐ DISCOVER

### CREDIT CARD USERS

**SIGNATURE AND ADDRESS OF CARD HOLDER IS MANDATORY.**

**IF YOU ARE PAYING VIA ANOTHER PERSONS CARD, HE/SHE MUST PRINT AND SIGN NAME AND ADDRESS.**

PRINT CARD HOLDER NAME: \_\_\_\_\_

**CREDIT CARD HOLDER SIGNATURE:** \_\_\_\_\_

CREDIT CARD EXPIRATION DATE: \_\_\_\_\_ / \_\_\_\_\_

**CREDIT CARD HOLDER ADDRESS, SPECIFICALLY PO BOX, OR STREET/HOUSE NUMBER, AND ZIP CODE.**

**CREDIT CARD ACCOUNT #**[illegible]

November 1997

# THE APPLIED COMPUTATIONAL ELECTROMAGNETICS SOCIETY

## 14TH ANNUAL REVIEW OF PROGRESS

### IN APPLIED COMPUTATIONAL ELECTROMAGNETICS

March 16-20, 1998  
Naval Postgraduate School  
Monterey, CA

#### Pre-Registration Form

Please print (BLACK INK)

(NOTE: CONFERENCE REGISTRATION FEE DOES NOT INCLUDE ACES MEMBERSHIP FEE OR SHORT COURSE FEE)

LAST NAME	FIRST NAME	MIDDLE INITIAL
COMPANY/ORGANIZATION/UNIVERSITY		DEPARTMENT/MAIL STATION
MAILING ADDRESS		
CITY	PROVINCE/STATE	COUNTRY
		ZIP/POSTAL CODE
TELEPHONE	FAX	E-MAIL ADDRESS
		AMATEUR RADIO CALL SIGN

	BEFORE 3/1/98	3/1/98 TO 3/11/98	AFTER 3/11/98
ACES MEMBER	<input type="checkbox"/> \$ 255	<input type="checkbox"/> \$ 270	<input type="checkbox"/> \$ 285
NON-MEMBER	<input type="checkbox"/> \$ 295	<input type="checkbox"/> \$ 310	<input type="checkbox"/> \$ 325
STUDENT/RETIRED/UNEMPLOYED	<input type="checkbox"/> \$ 115 (no proceedings)	<input type="checkbox"/> \$ 115	<input type="checkbox"/> \$ 115
STUDENT/RETIRED/UNEMPLOYED	<input type="checkbox"/> \$ 150 (includes proceeding)	<input type="checkbox"/> \$ 150	<input type="checkbox"/> \$ 150
BANQUET <input type="checkbox"/> Meat <input type="checkbox"/> Fish	<input type="checkbox"/> \$ 30	<input type="checkbox"/> \$ 30	<input type="checkbox"/> \$ 30

**Short Course information is not available at this time.** (1) If you desire Short Course information, please contact Michael A. Jensen, ECE Dept. 459 CB, BYU, Provo, UT 84602, email: jensen@ee.byu.edu. (2) If you plan to attend this conference, and are NOT PRESENTING a paper, please return this form to Richard W. Adler, ECE Dept/Code EC/AB, Naval Postgraduate School, 833 Dyer Rd, Rm 437, Monterey, CA 93943-5121, email: rwa@ibm.net. (3) If you ARE AN AUTHOR ON a paper, send this form to: Jianming Jin, U of Illinois, ECE Dept. 1406 W. Green St. Urbana, IL 61801-2991. email: j-jin1@uiuc.edu. (See pg 44, Call for papers, for Short Course prices).

**Non-USA participants:** Prices are in U.S. dollars. All currencies must be converted to U.S. dollars payable by banks with U.S. affiliates. (1) Bank Checks must be: (a) drawn on a U.S. Bank, (b) have U.S. bank address, (c) contain series of (9) digit mandatory routing numbers on left bottom of check; (2) Traveler's Checks (in U.S. \$\$); (3) International Money Order drawn in U.S. funds, payable in U.S.; (4) Credit Cards: Visa, MasterCard, Discover and AmEx.

**PAYMENT METHOD: CHECKS/TRAVELER'S CHECKS, MONEY ORDERS, ARE PAYABLE ONLY TO: "ACES"**

☐ BANK CHECK ☐ TRAVELER'S CHECKS ☐ INTERNATIONAL MONEY ORDER

CREDIT CARD: ☐ VISA ☐ MASTERCARD ☐ AMEX ☐ DISCOVER

#### CREDIT CARD USERS

**SIGNATURE AND ADDRESS OF CARD HOLDER IS MANDATORY!**

**IF YOU ARE PAYING VIA ANOTHER PERSONS CARD, THE CARD HOLDER MUST PRINT & SIGN NAME AND ADDRESS.**

PRINT CARD HOLDER NAME: \_\_\_\_\_

CREDIT CARD HOLDER SIGNATURE: \_\_\_\_\_

CREDIT CARD EXPIRATION DATE: \_\_\_\_\_ / \_\_\_\_\_

CREDIT CARD HOLDER ADDRESS: \_\_\_\_\_

CREDIT CARD ACCOUNT #

--	--	--	--	--	--	--	--	--	--	--	--	--	--	--	--	--	--	--	--

November 1997

ADVERTISING RATES		
	FEE	PRINTED SIZE
Full page	\$200.	7.5" x 10.0"
1/2 page	\$100.	7.5" x 4.7" or 3.5" x 10.0"
1/4 page	\$ 50	3.5" x 4.7"
<p>All ads must be camera ready copy.</p> <p>Ad deadlines are same as Newsletter copy deadlines.</p> <p>Place ads with Ray Perez, Newsletter Editor, Martin Marietta Astronautics, MS 58700, PO Box 179, Denver, CO 80201, USA. The editor reserves the right to reject ads.</p>		

ACES NEWSLETTER AND JOURNAL COPY INFORMATION	
<u>Issue</u>	<u>Copy Deadline</u>
March	January 13
July	May 25
November	September 25

# APPLIED COMPUTATIONAL ELECTROMAGNETICS SOCIETY JOURNAL

## INFORMATION FOR AUTHORS

### PUBLICATION CRITERIA

Each paper is required to manifest some relation to applied computational electromagnetics. **Papers may address general issues in applied computational electromagnetics, or they may focus on specific applications, techniques, codes, or computational issues.** While the following list is not exhaustive, each paper will generally relate to at least one of these areas:

**1. Code validation.** This is done using internal checks or experimental, analytical or other computational data. Measured data of potential utility to code validation efforts will also be considered for publication.

**2. Code performance analysis.** This usually involves identification of numerical accuracy or other limitations, solution convergence, numerical and physical modeling error, and parameter tradeoffs. However, it is also permissible to address issues such as ease-of-use, set-up time, run time, special outputs, or other special features.

**3. Computational studies of basic physics.** This involves using a code, algorithm, or computational technique to simulate reality in such a way that better or new physical insight or understanding is achieved.

**4. New computational techniques,** or new applications for existing computational techniques or codes.

**5. "Tricks of the trade"** in selecting and applying codes and techniques.

**6. New codes, algorithms, code enhancement, and code fixes.** This category is self-explanatory but includes significant changes to existing codes, such as applicability extensions, algorithm optimization, problem correction, limitation removal, or other performance improvement. **Note: Code (or algorithm) capability descriptions are not acceptable, unless they contain sufficient technical material to justify consideration.**

**7. Code input/output issues.** This normally involves innovations in input (such as input geometry standardization, automatic mesh generation, or computer-aided design) or in output (whether it be tabular, graphical, statistical, Fourier-transformed, or otherwise signal-processed). Material dealing with input/output database management, output interpretation, or other input/output issues will also be considered for publication.

**8. Computer hardware issues.** This is the category for analysis of hardware capabilities and limitations in meeting

various types of electromagnetics computational requirements. Vector and parallel computational techniques and implementation are of particular interest.

Applications of interest include, but are not limited to, antennas (and their electromagnetic environments), networks, static fields, radar cross section, shielding, radiation hazards, biological effects, electromagnetic pulse (EMP), electromagnetic interference (EMI), electromagnetic compatibility (EMC), power transmission, charge transport, dielectric and magnetic materials, microwave components, MMIC technology, remote sensing and geophysics, communications systems, fiber optics, plasmas, particle accelerators, generators and motors, electromagnetic wave propagation, non-destructive evaluation, eddy currents, and inverse scattering.

Techniques of interest include frequency-domain and time-domain techniques, integral equation and differential equation techniques, diffraction theories, physical optics, moment methods, finite differences and finite element techniques, modal expansions, perturbation methods, and hybrid methods. This list is not exhaustive.

A unique feature of the Journal is the publication of unsuccessful efforts in applied computational electromagnetics. Publication of such material provides a means to discuss problem areas in electromagnetic modeling. Material representing an unsuccessful application or negative results in computational electromagnetics will be considered for publication only if a reasonable expectation of success (and a reasonable effort) are reflected. Moreover, such material must represent a problem area of potential interest to the ACES membership.

Where possible and appropriate, authors are required to provide statements of quantitative accuracy for measured and/or computed data. This issue is discussed in "Accuracy & Publication: Requiring quantitative accuracy statements to accompany data", by E.K. Miller, *ACES Newsletter*, Vol. 9, No. 3, pp. 23-29, 1994, ISBN 1056-9170.

### EDITORIAL REVIEW

In order to ensure an appropriate level of quality control, papers are refereed. They are reviewed both for technical correctness and for adherence to the listed guidelines regarding information content. Authors should submit the initial manuscript in draft form so that any suggested changes can be made before the photo-ready copy is prepared for publication.



## STYLE FOR CAMERA-READY COPY

The ACES Journal is flexible, within reason, in regard to style. However, certain requirements are in effect:

1. The paper title should NOT be placed on a separate page. The title, author(s), abstract, and (space permitting) beginning of the paper itself should all be on the first page. The title, author(s), and author affiliations should be centered (center-justified) on the first page.

2. An abstract is REQUIRED. The abstract should state the computer codes, computational techniques, and applications discussed in the paper (as applicable) and should otherwise be usable by technical abstracting and indexing services.

3. Either British English or American English spellings may be used, provided that each word is spelled consistently throughout the paper.

4. Any commonly-accepted format for referencing is permitted, provided that internal consistency of format is maintained. As a guideline for authors who have no other preference, we recommend that references be given by author(s) name and year in the body of the paper (with alphabetical listing of all references at the end of the paper). Titles of Journals, monographs, and similar publications should be in boldface or italic font or should be underlined. Titles of papers or articles should be in quotation marks.

5. Internal consistency shall also be maintained for other elements of style, such as equation numbering. As a guideline for authors who have no other preference, we suggest that equation numbers be placed in parentheses at the right column margin.

6. The intent and meaning of all text must be clear. For authors who are NOT masters of the English language, the ACES Editorial Staff will provide assistance with grammar (subject to clarity of intent and meaning).

7. Unused space should be minimized. Sections and subsections should not normally begin on a new page.

## MATERIAL, SUBMITTAL FORMAT AND PROCEDURE

The preferred format for submission and subsequent review, is 12 point font or 12 cpi, double line spacing and single column per page. Four copies of all submissions should be sent to the Editor-in-Chief. Each submission must be accompanied by a covering letter. The letter should include the name, address, and telephone and/or fax number and/or e-mail address of at least one of the authors.

Only camera-ready original copies are accepted for publication. The term "**camera-ready**" means that the material is neat, legible, and reproducible. The preferred font style is Times Roman 10 point (or equivalent) such as that used in this text. A double column format similar to that used here is preferred. **No author's work will be turned down once it has been accepted because of an inability to meet the requirements concerning fonts and format.** Full details are sent to the author(s) with the letter of acceptance.

There is NO requirement for India ink or for special paper; any plain white paper may be used. However, faded lines on figures and white streaks along fold lines should be avoided. Original figures - even paste-ups - are preferred over "nth-generation" photocopies. These original figures will be returned if you so request.

While ACES reserves the right to re-type any submitted material, this is not generally done.

## PUBLICATION CHARGES

ACES members are allowed 12 pages per paper without charge; non-members are allowed 8 pages per paper without charge. Mandatory page charges of \$75 a page apply to all pages in excess of 12 for members or 8 for non-members. Voluntary page charges are requested for the free (12 or 8) pages, but are NOT mandatory or required for publication. A priority courtesy guideline, which favors members, applies to paper backlogs. Full details are available from the Editor-in-Chief.

## COPYRIGHTS AND RELEASES

Each primary author must sign a copyright form and obtain a release from his/her organization vesting the copyright with ACES. Forms will be provided by ACES. Both the author and his/her organization are allowed to use the copyrighted material freely for their own private purposes.

Permission is granted to quote short passages and reproduce figures and tables from an ACES Journal issue provided the source is cited. Copies of ACES Journal articles may be made in accordance with usage permitted by Sections 107 or 108 of the U.S. Copyright Law. This consent does not extend to other kinds of copying, such as for general distribution, for advertising or promotional purposes, for creating new collective works, or for resale. The reproduction of multiple copies and the use of articles or extracts for commercial purposes require the consent of the author and specific permission from ACES. Institutional members are allowed to copy any ACES Journal issue for their internal distribution only.